Optical Properties of Metal Nanoparticle Arrays created using Electron Beam Lithography for Solar Cell Applications

Ranveig Flatabø

Master Thesis in Nano Science

Supervisors: Professor Dr. Bodil Holst
Dr. Martin Møller Greve

Department of Chemistry
University of Bergen

June 2014

Acknowledgements

I would like to express my sincere gratitude to my supervisors Professor Dr. Bodil Holst and Dr. Martin Møller Greve for giving me the opportunity to be a part of this project. For giving me the opportunity to conduct real science and experience how it is when things just don't work - and when they finally do! I am ever grateful for the guidance, support and constructive feedback Bodil has given me throughout this year. This combined with Martin's ability to explain complex processes in terms of simple words as well as his commitment to my work have been invaluable for the work presented in this thesis. I also wish to thank Professor Dr. Ingve Simonsen at the NTNU for welcoming me in Trondheim and sharing his passion for computational physics as well as for his generous contributions of knowledge and experience. I would also like to acknowledge the rest of the nanophysics group for their help and our discussions throughout the work of this thesis. Last but not least, I would like to thank my family and friends for their love and support.

Abstract

Metal nanoparticles (MNPs) are of key interest in many research fields due to their unique optical properties, which are largely dominated by the localized surface plasmon resonance (LSPR) effect. The LSPR effect gives rise to intense light absorption by the MNP at certain wavelengths of incident light. The LSPR wavelength can be manipulated by changing the size and shape of the MNPs as well as by changing the surrounding medium, opening for a variety of applications such as optical- and biological sensing and solar energy conversion.

The company EnSol AS has patented a novel thin-film solar cell technology based on the LSPR effect in MNPs. The University of Bergen, in collaboration with EnSol, has started a project of investigating and optimizing the production parameters of the EnSol solar cell with the ultimate aim of producing model solar cells. As a step in the optimization process, the optical properties of large arrays of nanoparticles need to be investigated theoretically and experimentally. This has been the aim of this thesis work. Large arrays (9 mm^2 - 16 mm^2) of disk-shaped aluminum, gold or nickel NPs fabricated on non-conductive glass substrates have been fabricated by the means of electron beam lithography (EBL). MNP disks of diameter down to 20 nm have been fabricated. The optical properties of MNP arrays are analyzed for disk diameters in the range 30 nm – 45 nm with a constant height of 25 nm. EBL suffer from low throughput, but offer high control of particle size, shape and orientation which is of prime importance in the development of reliable model system where size- and shape dependent properties are investigated. The large size of the arrays allows optical investigation using spectroscopy techniques, making it possible to mimic realistic operation conditions of the solar cell. The LSPR wavelengths are found experimentally using an integrating sphere set-up. The experimental results are tested and supported by theoretical calculations based on an electrostatic model developed by I. Simonsen and R. Lazzari, where the disk-shaped metal nanoparticles are approximated as spheroids truncated by a glass substrate. Despite the discrepancies in particle shape between the model and experimental system, good qualitative agreement is found. The LSPR wavelength is also found to be in good agreement with published literature that in most cases is based on much smaller arrays.

Contents

List of Figures

List of Tables

Chapter 1

Introduction

1.1 Background

The first volume of the fifth Intergovernmental Panel on Climate Change (IPCC) report [1], released in September 2013, presents a comprehensive study on the science of climate change. The consensus of the report is clear; the average global temperature has increased since the mid-20th century, owing to human-induced emissions of greenhouse gases (e.g. CO_2, CH_4, H_2O, NO_x). Greenhouse gases in the atmosphere absorb infrared (IR) radiation emitted from the surface of the Earth. Re-emission of this thermal radiation effectively warms the surface of the planet. This process, known as the greenhouse effect, is in principle vital to life on Earth. However, increased concentrations of greenhouse gases in the atmosphere, related in particular to the combustion of fossil fuels, have greatly enhanced the natural greenhouse effect [2], evident as an ongoing increase in the average global temperature. Possible emission schemes predict that the average global temperature will increase between 0.3 and 6.4 degree Celsius during the 21st century relative to pre-2000 conditions [1].

Global warming is one feature of the totality of attributes that define climate change. The rise in global temperature has been accompanied by changes in weather patterns, ocean levels and the direction and speed of wind and ocean currents [1]. Continued emissions at or above current rate will induce climate changes characterized as irreversible. IPCC urges "substantial and sustained reduction of greenhouse gas emissions" [1].

One of the biggest climate polluter, with regard to CO_2 emissions, is the global electricity sector [3]. In 2009 coal power provided 40.6 % of the world's electricity needs. The runner-up was natural gas (21.4 %), followed by hydropower (16.4%) and nuclear power (13.4 %). The energy sources and their percent share of the total electricity generation in 2009 are tabulated in Fig. 1.1. The world's hunger for electricity is increasing in line with human population, industrialization of third world countries and improved standard of living [3]. Harnessing renewable electricity sources are of prime importance in order to avert future global warming and climate change [1].

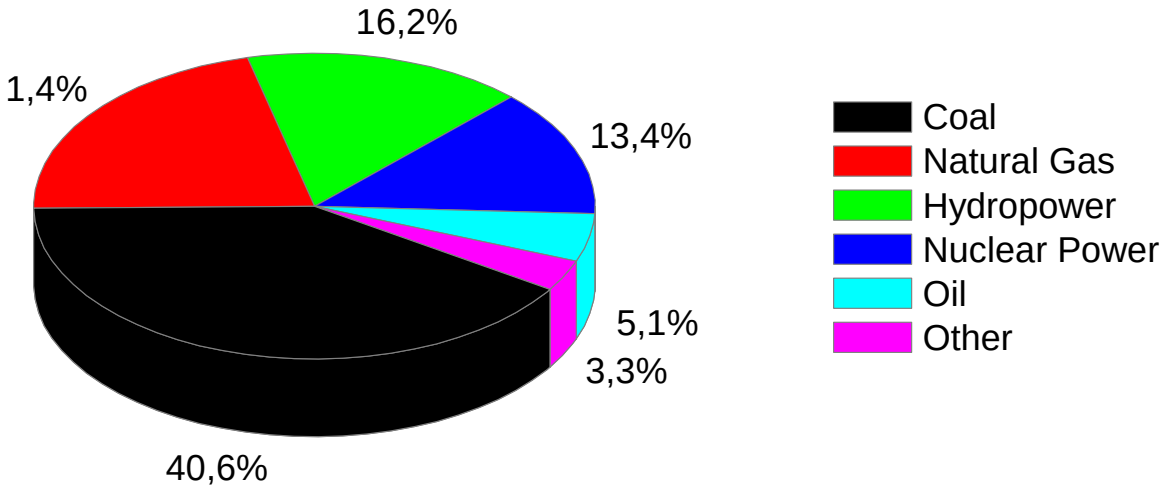

Figure 1.1: Total electricity generation by fuel in 2009. *Others* include electricity generated from solar, wind, biomass and the renewable fraction of municipal waste, geothermal sources, ocean, tidal and wave resources and biofuel [3]. Data obtained from [3]

A solar cell converts solar energy (sunlight) directly into electric energy. It does not, in principle, emit greenhouse gases, such as coal-fired power stations, nor does it create waste that needs to be stored, such as electricity generated from nuclear power [3]. The maximum solar irradiance, that is, the amount of power per unit area, that reaches the surface of the Earth at normal incidence is about is about 1000 W/m^2 (power density at a given wavelength). If harvested efficiency, the world's electricity (and energy!) needs could be met by solar power alone [2]. Solar cells are, partly due to the above mentioned properties, described as prime candidates for meeting the world's future need for electricity in a sustainable manner[4]. However, as evident from Fig. 1.1, solar cells provided a tiny fraction of the world's electricity needs in 2009 [3]. Currently, the power-to-price ratio of solar cells is too low with respect to other sources of electricity. Hence, the expense of solar cells must be reduced to make them an economically viable source of electricity. This depends upon the development of novel or improved solar cell technologies [4]. One such solar cell technology is the subject of the present thesis.

1.2 Principles of Solar Cell Operation

In 1838 Becquerel [5] observed a voltage developed upon the illumination of a solid electrode in an electrolyte solution. This phenomenon, known as the photovoltaic effect, is the fundamental physical process solar cell utilizes in order to convert light into electric energy. The majority of solar cells to date comprises a positive-negative (p-n) semiconductor junction across which the photovoltage is generated [6]. A cross-section of an illuminated p-n

semiconductor junction is given in Fig. 1.2.

AA p-n junction is formed by introducing impurities (i.e. by adding dopants) into the semiconductor material [7]. Currently, most solar cells are based on silicon p-n junctions [8]. Positive doping (p-doping), giving rise to a net positive charge, is achieved by adding atoms with fewer valence electrons than silicon (e.g. boron), while adding atoms with more valence electrons (e.g. phosphor) is termed negative doping. The charge difference across the junction causes electrons to diffuse from the n-side to the p-side, where they recombine with holes and vice versa. As electrons diffuse across the junction they leave behind immobile, positively charged ions, whereas holes that diffuse across the junction leave behind immobile, negatively charged ions. These fixed ions sets up an electric field ($\mathbf{E}_0$) which effectively depletes a region, termed depletion region, close to the junction of mobile charges. This electric field inhibits the diffusion and as the system reaches equilibrium, the drift current and the diffusion current equals out [7].

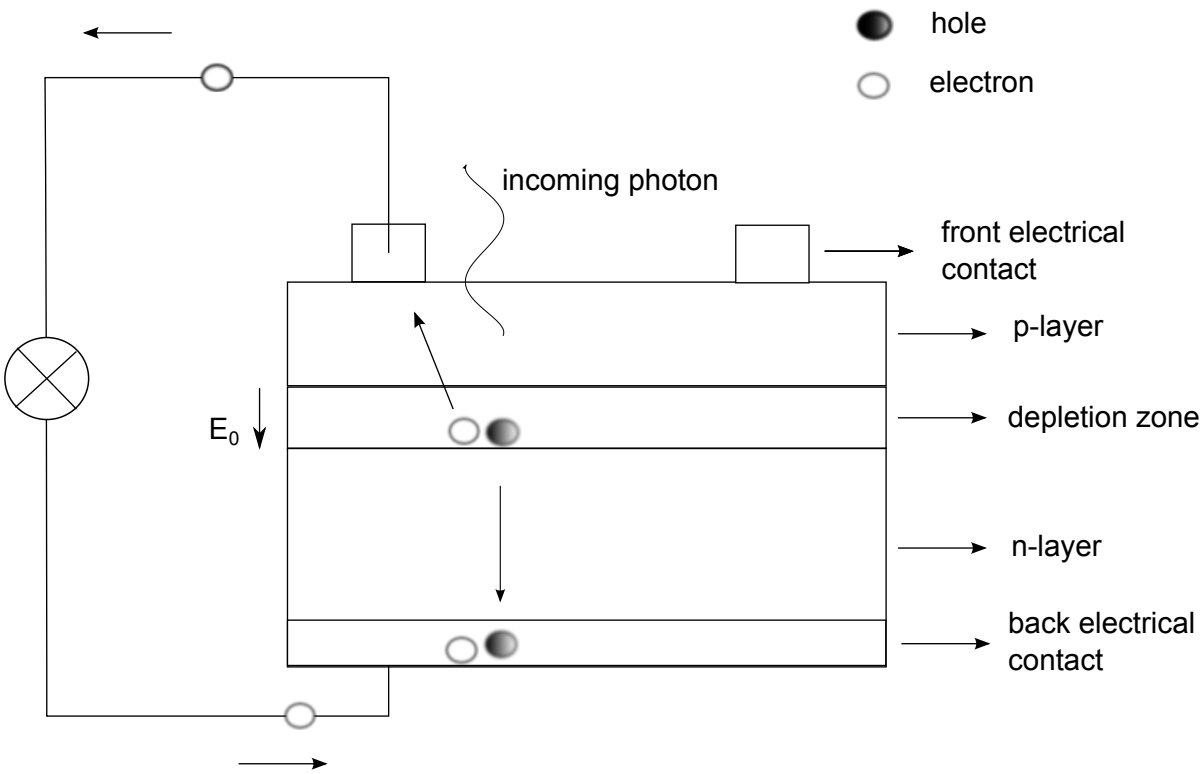

Figure 1.2: Cross-section of an illuminated p-n semiconductor junction solar cell.Incoming light of sufficient energy excites an electron-hole pair. The electric field (E_0) separates the charges, which in turn produces a voltage. Since the system is connected to a load, this voltage is used to force electrons to an outer circuit which generates a current [7]. Redrawn from [9]

All electromagnetic radiation consists of discrete energy quanta termed photons. The energy of a photon is given by [7]

$$E = h\nu \tag{1.1}$$

where h is Planck's constant and ν is the photon frequency. Sunlight consists of photons with a wide range of energies, spanning the ultraviolet (UV), visible and infrared (IR) regions of the electromagnetic spectrum [2].

A semiconductor solar cell can only absorb photons with energy E equal to or greater than the energy of the bandgap E_{bg} of the cell material. The bandgap is defined as the energy difference between the valence band and the conduction band i.e. an energy range where no electron states exist [7]. Hence, when $E \geq E_{bg}$ the incident photon can excite an electron-hole pair. If this electron-hole pair is created in the depletion zone, the electric field across the junction forces the electron to drift to the n-side, while the hole flows to the p-side. This separation of charge produces a voltage; the photovoltaic effect in practice. If the system is connected to a load, the produced voltage is used to force electrons to an outer circuit, and hence, generate a current [7].

A photon of energy $E < E_{bg}$ does not possess enough energy to excite an electron to the conduction band. As described above, a photon of energy $E > E_{bg}$ can generate an electron-hole pair. However, excess energy above the bandgap is lost as heat. These two loss mechanisms are termed spectrum loss. Spectrum loss is given as a function of bandgap energy and limit the efficiency of semiconductor solar cells [10]. The efficiency of a solar cell is defined as the percentage of incident solar energy that is converted into electricity [11]. In the case of silicon, whose bandgap is 1.1 eV [12], spectrum loss limits the efficiency to approximately 50 % [10]. Furthermore, in a real solar cell, not all electron-hole pairs contribute to the generation of a current, as an electron may relax back to its ground state before it reaches the contact (see Fig. 1.2). The sum of these loss mechanisms make up the fundamental limit of efficiency – the so-called detailed balance limit [13]. The detailed balance limit is based on the assumptions that one photon generates one electron-hole pair and that the sunlight is not concentrated. The maximum efficiency of an ideal silicon solar cell is, according to the detailed-balance limit, 29%. The absolute limit of efficiency with which light (energy) can be converted to electricity is 95 % [14]. This suggests that the performance of a solar cell can be improved by multiple factors if the underlying material and/or concept are changed.

1.3 Solar Cell Technologies

The modern age of solar cell technology began in 1954 when Chapin et al. [15] built the very first silicon solar cell. The efficiency of this solar cell was approximately 6 % [15]. For many years following this event the only widespread use of solar cells was in spacecraft. State-of-the-art solar cells are still widely used to power outer-space shuttles [16]. The major challenge is to develop solar cell technologies for widespread commercial use. Nevertheless, thanks to technological development and political incentives the solar cell market is rapidly growing [12]. Traditional as well as novel technologies are being exploited.

Solar cells can be divided into three generations, simply designated first, second and third

[14]. Wafer-based silicon solar cells; either in mono-crystalline or poly-crystalline form, are known as first-generation solar cells. First generation solar cells are the only generation that has reached large-scale commercialization [8]. Mono-crystalline silicon solar cells have reached of nearly 25 % at laboratory scale [17], but efficiencies of commercial cells are in the range between 15 % and 22 % [8]. Mono-crystalline silicon solar cells do, however, suffer from a very energy-intensive and expensive manufacturing process. Commercial poly-crystalline silicon cells typically have efficiencies in the range 12 % – 15 %. It is worth noting that the presence of defects and metal imputites in poly-crystalline silicon give rise to a less energy-intensive manufacturing process although this currently comes with a minor trade-off in terms of efficiency [8].

Second-generation solar cells, so-called thin-film solar cells, are addressing the cost issues by reducing the content of the semiconductor material. A thin-film solar cell consists of a thin-layer (μm) of photo-sensitive material deposited on top of a low-cost substrate (e.g. glass, plastic). Examples of photo-sensitive material used in thin-film solar cells are amorphous and crystalline silicon, cadmium telluride (CdTe) and copper indium selenium (CIS). In addition to the reduced material volume, alternative manufacturing processes give rise to a reduction in cost. Currently however, thin-film solar cells are not as efficient as first-generation silicon solar cells. A CdTe thin-film solar cell has reached an efficiency of 17.3 % at laboratory scale [8].

Semiconductor solar cells, independent of generation, suffer from the detailed-balance limit (described in the previous section). Since this limit is given as a function of bandgap energy, it varies from semiconductor to semiconductor. The ideal bandgap given by the detailed-balance limit, that is, the bandgap that theoretically provides the highest efficiency is 1.4 eV - 1.5 eV, corresponding to an efficiency of approximately 33 % [11].

Third generation solar cells are currently at the pre-commercial stage. This generation exploits a number of novel technologies, aimed to overcome the detailed-balance efficiency limit at low cost [14]. Multi-junction solar cells, also known as tandem cells, are a well-known example of a third generation solar cell. By combining several semiconductors, thereby introducing several bandgap energies, the detailed-balance limit can be surpassed. Indeed, an efficiency of 43.5 % has been reported for a triple-junction III-V solar cell [17]. This was achieved by concentrating sunlight by the means of mirrors with an intensity of 418 times the intensity of natural sunlight.

Nanostructures, particles with one or more dimensions on the nanoscale (1-100 nm), have emerged as key building blocks of future solar cells [18]. For instance, metal nanoparticles deposited on top of thin-film solar cells are currently being exploited as a method of improving light-trapping. By utilizing a unique property of metal nanoparticles, termed the localized surface plasmon resonance effect (described in greater detail in Section 1.4 and Chapter 2), it is possible to increase light-trapping in semiconductor solar cells which in turn increases light absorption [19]. Another example is the TiO_2 dye-sensitized solar cell, a third-generation solar

cell comprised of titanium dioxide (TiO_2) nanoparticles coated with a light-sensitive dye. In interaction with light the dye-electrons are excited and transferred to the conduction band of TiO_2. Currently, the dye-sensitized solar cell has reached an efficiency of approximately 11 % at laboratory scale. However, the dye-sensitized solar cell can be made of low-cost material and is regarded as a prime candidate for future solar power [8].

1.4 The EnSol Solar Cell

The Norwegian company EnSol AS has patented [20] a thin-film solar cell technology, based on metal nanoparticles (MNPs) enclosed in a transparent composite matrix. A thin-film deposition system for fabricating solar cells with an active area of 10 cm $\times$ 10 cm is under construction. The objective is to develop a competitive solar cell with an efficiency of 20 % or greater, through systematically refining the technology [1].

The MNPs is enclosed in a non-conductive and transparent material, as schematically illustrated in Fig. 1.3. The difference between the work functions (a work function expresses the minimum energy required to separate an electron from a solid to a point in vacuum outside the solid) of the front and back electrode produces an electric field. This electric field forces electrons to the front electrode and hence generates a current. The MNPs provide the electrons that generate the electric current [21]. Provided that the particles are smaller than the wavelength of incoming light, the incident electric field of light will displace the mobile conduction electrons of the MNP relative to the fixed ion cores. This displacement sets up a restoring force between the ion cores and the conduction electrons giving rise to a collective oscillation of the electrons once they are excited. A resonance condition arises when the frequency of light matches the eigenfrequency of the oscillating system [22]. This resonance is termed localized surface plasmon resonance (LSPR) and gives, among others, rise to intense absorption by the MNP. The energy stored in the LSPR can decay radiatively by emission of light or non-radiatively through the generation of electron-hole pairs [23]. The EnSol solar cell will utilize the latter decay-channel to extract electrons to an outer circuit and thereby generate a current. In 2011, a year after EnSol patented the thin-film solar cell, Knight et al. [24] studied photocurrent generated by gold nanoparticles deposited on a semiconductor surface and demonstrated that such hot (i.e. high kinetic energy) electrons generated via LSPR decay can produce a photocurrent.

For noble MNPs the resonance condition is met in the visible and near-infra red (IR) regions of the electromagnetic spectrum. However, it is possible to tune the energy (wavelength) at which the resonance condition is met by changing the size and shape of the MNPs as well as by changing the surrounding medium (described in greater detail in Chapter 2). The EnSol technology can utilize this tuning to produce solar cell that potentially can be used in areas unattractive to traditional solar cell. Furthermore, as this novel technology is not based on

[1] Assessed from www.ensol.no

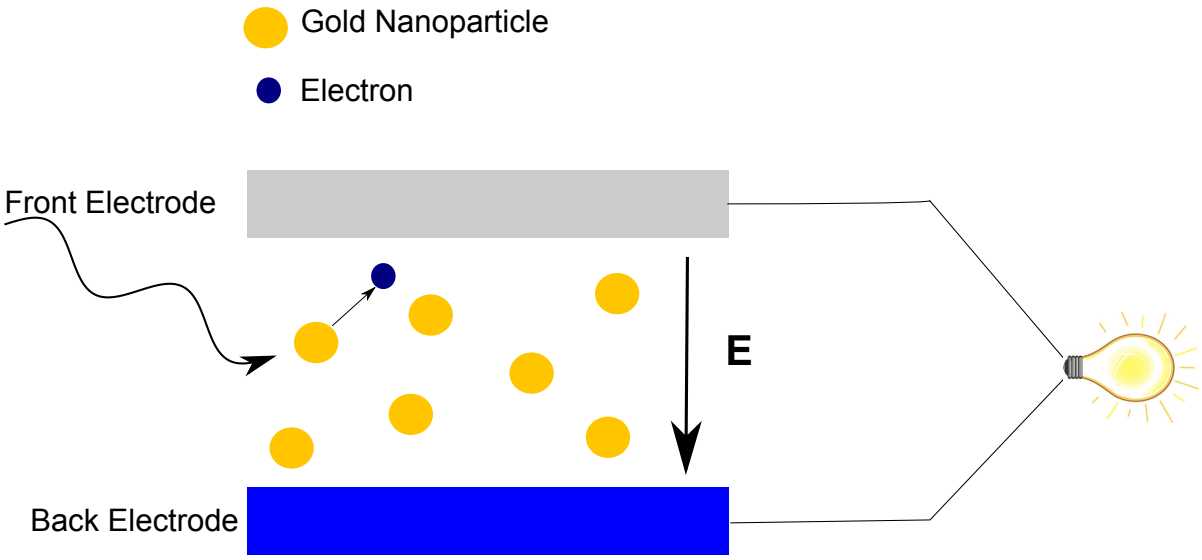

Figure 1.3: Illustration of the working principles of the EnSol solar cell. An incident photon, drawn as a black, curved arrow excites the LSPR of a gold NP. The LSPR decays by emitting hot electrons that due to the built-in electric field are forced to an outer circuit. Redrawn from [21]

semiconductors it is not subjected to the detailed-balance limit. The EnSol solar cell aims to achieve an efficiency of 20 % by systematically refining the absorption properties of MNPs.

1.5 Thesis Objectives

The University of Bergen (UoB) is a collaborating partner in the EnSol solar cell project. The long-term objective of the work at UoB is built model solar cells by the means of electron beam lithography (described in Chapter 4.2.1). Electron beam lithography (EBL) enables fabrication of MNP in a highly controlled manner with respect to size, shape and array arrangement. The model solar cells will thus be used to optimize the EnSol solar cell production parameters.

The first contribution to the optimization of the EnSol solar cell was made by Håvardstun [9]. Håvardstun established a procedure for fabricating large (16 mm^2 - 25 mm^2) arrays of MNPs of diameters in the range 45 nm - 150 nm situated on a transparent substrate using EBL as well as a method for studying the interaction of the MNP arrays and visible light by the means of transmission spectroscopy. The large area of the arrays allows for investigation of the LSPR effect using spectroscopy techniques rather than microscopy techniques previously used [83]. The objective of this thesis work has been to improve Håvardstuns production method to enable the fabrication of smaller nanoparticles (diameters down to 20 nm). The size of the arrays are in the range 9 mm^2 - 16 mm^2 comprising up to 160 million nanoparticles. Furthermore, the topic of this thesis work has been to extend the spectroscopy-testing setup with an integrating sphere (described in greater detail in Chapter 4.6). Finally, a theoretical framework for analyzing the experimental results has been established. This has been done in

cooperation with Professor Ingve Simonsen at NTNU. More exact, the objectives of this thesis are

- Produce MNP arrays situated on a non-conductive glass substrate by the means of EBL to evaluate the effect of MNP size as well as the magnitude of the interparticle distance upon the optical response of the array, in particular the LSPR wavelength. The effect of the interparticle distance is evaluated with respect to near-field coupling between neighboring particles (i.e. particle-particle interactions).
- Establish a procedure for fabricating MNPs using a bi-layer resist scheme
- Study the optical response of the produced MNP arrays by the means of an integrating sphere
- Establish theoretical framwork for analysing the optical response of MNP arrays using the GranFilm code developed by Professor Ingve Simonsen.

The first step of this thesis work was to find suitable writing parameters for producing disk-shaped MNPs with a diameter of in the range between 30 nm - 45 nm and an interparticle distance ranging from 90 nm to 150 nm. The size of the MNPs and the corresponding interparticle distance is chosen to evaluate how the magnitude of the spacing affects the optical response of the MNPs. A center-to-center spacing equal to or greater than 3 times the particle diameter eliminates near-field coupling between neighboring particles [25]. The second step was to use a bi-layer resist scheme to fabricate even smaller MNPs (MNP diameter down to 20 nm has been successfully produced). A bi-layer resist scheme was employed as it eases the lift-off process. Finally, an integrating sphere set-up was used to obtain extinction spectra of the MNP arrays, while the GranFilm code was used to calculate corresponding model extinction spectra.

1.6 Thesis Outline

Chapter 2 presents the theoretical background of the localized surface plasmon resonance effect, while Chapter 3 outlines the physical principles behind the theoretical modelling done in this work. Chapter 4 introduces the experimental equipment used in sample production and characterization. The experimental procedure is presented in Chapter 5. The main emphasis in Chapter 4 and 5 has been on the description of instrumentation and methods that have been established during this thesis work. Sample production parameters and structural characterization, modeling results and optical measurements of MNPs are presented and discussed in Chapter 6. Chapter 7 encloses the conclusion and the suggestions for further work.

Chapter 2

Theoretical Background: The Localized Surface Plasmon Resonance Effect

This chapter presents the fundamentals of the localized surface plasmon resonance (LSPR) effect in metal nanoparticles (MNPs). Most of the physics underlying the interaction of light and MNPs can be extracted from the dielectric function of the metal. The dielectric function is therefore the starting point of this chapter, followed by an introduction to surface plasmon polaritons at metal-dielectric interfaces. The chapter finishes with a discussion of localized surface plasmons in MNPs with prime focus on the resonance condition.

2.1 Towards Sub-Wavelength Optics

The interaction between light and MNPs has intrigued humans since ancient times. Well before any theory explaining the nature of this interaction was developed, glassmakers employed MNPs to generate colors in glass artifacts and in the staining of church windows [26]. One of the most famous results is the Lycurgus cup, a glass vessel produced around 300 B.C., currently housed in the British museum. The cup exhibits different colors depending on the position of the light source, the cup and the observer. The cup appears green when light reflected off the cup is observed and ruby-red when light transmitted through the cup is observed [27]. Nowadays, it is well-known that the characteristic colors of the Lycurgus cup are caused by interaction between gold and silver nanoparticles embedded in the glass and light [26]. The characteristic colors exhibited by noble metal nanoparticles are a manifestation of the LSPR effect [23].

By combining optics and nanoscience and nanotechnology, the scientific field of nanoplasmonics emerges [22]. Nanoplasmonics exploits the interaction of light and MNPs [28]. At first glance, optics does not seem relevant to the nanometer world, since the diffraction limit states that electromagnetic radiation cannot be confined to a region smaller than about half the light's wavelength. However, by utilizing the LSPR effect it is possible to squeeze light into

the nanometer regime [29].

At the turn of the 19th century Maxwell [30] described the physical phenomena related to the interaction of light and matter. Maxwell developed the theory of light as an electromagnetic wave and described the dynamics of electromagnetic fields through what is now known as Maxwell's equations. An exact solution to Maxwell's equation describing the scattering of electromagnetic radiation by a sphere of arbitrary size was presented in 1908 by Mie [31]. In 1956 Pines [32] attributed the energy loss experienced by electrons traveling through metals to a collective oscillation of the metal's conduction electrons. Pines named this collective oscillation (volume) plasmon. In 1957 Ritchie [33] demonstrated that plasmons can be excited near metal surfaces. In 1970 Kreibig and Zacharias [34] described the optical properties of metal nanostructure in terms of plasmons. Currently, nanoplasmonics is a rapidly growing field of science and technology [22]. Theories describing the underlying nature of the interaction between MNPs and light are being developed and practical applications utilizing the LSPR effect are being exploited [26].

2.2 The Dielectric Function

The interaction of matter and electromagnetic fields are, within the framework of classical physics, described by Maxwell's equations. In SI units Maxwell's equations read as follows [28, 35]

$$\bigtriangledown \times \mathbf{E} = -\frac{\delta \mathbf{B}}{\delta t} \tag{2.1a}$$

$$\bigtriangledown \times \mathbf{H} = \mathbf{J} + \frac{\delta \mathbf{D}}{\delta t} \tag{2.1b}$$

$$\bigtriangledown \cdot \mathbf{D} = \rho \tag{2.1c}$$

$$\bigtriangledown \cdot \mathbf{B} = 0 \tag{2.1d}$$

where $\mathbf{E}$ is the electric field, $\mathbf{H}$ is the magnetic field, $\mathbf{D}$ is the electric displacement (electric flux density) and $\mathbf{B}$ is the magnetic induction (magnetic flux density). The quantities $\mathbf{J}$ and ρ are the current and charge densities, respectively, of any external sources (i.e. not including induced polarization current and charges) [35].

The electromagnetic fields are related to each other via the so-called constitutive relations. The precise form of the constitutive relations is determined by the material in which the fields exist. In linear, homogenous and isotropic materials the constitutive relations are given as [35]

$$\mathbf{D} = \varepsilon \varepsilon_0 \mathbf{E} \tag{2.2a}$$

$$\mathbf{B} = \mu\mu_0\mathbf{H} \tag{2.2b}$$

$$\mathbf{J} = \sigma\mathbf{E} \tag{2.2c}$$

where ε_0 is the electric permittivity and μ_0 is the magnetic permeability of vacuum, ε is the dielectric constant, μ is the relative permeability and σ is the conductivity. In Eq. 2.2a ε is a scalar. A scalar ε indicates that **D** reacts instantaneously to **E**, which is not true for real materials. The finite response time can be included in Eq. 2.2a by writing ε as a function of the angular frequency of the electric field. $\varepsilon(\omega)$ is known as the dielectric function and quantitatively describes the electromagnetic response of any material [36]. The dielectric function reads as follows [28]

$$\varepsilon(\omega) = 1 + \frac{i\sigma(\omega)}{\varepsilon_0\omega} \tag{2.3}$$

The conductivity and the dielectric function are complex valued functions [28]

$$\sigma(\omega) = \sigma_1(\omega) + i\sigma_2(\omega) \tag{2.4a}$$

$$\varepsilon(\omega) = \varepsilon_1(\omega) + i\varepsilon_2(\omega) \tag{2.5a}$$

where subscript 1 denotes the real part and subscript 2 denotes the imaginary part of $\sigma(\omega)$ and $\varepsilon(\omega)$. $\varepsilon_1(\omega)$ and $\sigma_2(\omega)$ describe how much the material polarizes when subjected to an external electric field, while $\varepsilon_2(\omega)$ and $\sigma_1(\omega)$ expresses the amount of absorption inside the material. The dielectric function is further connected to the complex refractive index $\widetilde{n}(\omega)$ through [28]

$$\widetilde{n}(\omega) = \sqrt{\varepsilon(\omega)} = n(\omega) + i\kappa(\omega) \tag{2.6}$$

where $n(\omega)$ is the real part and $\kappa(\omega)$ is the imaginary part of $\widetilde{n}(\omega)$. κ is termed the extinction coefficient and is related to the light absorption by the material [28].

2.2.1 The Drude Model

One of the simplest models used to describe the electromagnetic response of metals subjected to an electromagnetic field was developed by Drude. Despite its simplicity, the Drude model describes characteristic properties of metals, such as their high conductivity and high reflectivity at visible frequencies, remarkably well [37]. The Drude model is based on the assumption that metals behave like plasma (i.e. a sea of free charges) comprised of fixed, positive ion cores

and mobile conduction electron. The mass of each electron is expresses in terms of an effective optical mass. This effective optical mass carries some information regarding the band structure of the metal, but details of lattice potential and electron-electron interactions are ignored [28].

An external electric field excites the metal-plasma. Its oscillation is damped through collisions characterized by a collision frequency denoted γ where $\gamma = \frac{1}{\tau}$. τ is termed the relaxation time and is on the order of 10^{-14} s at room temperature [28]. In the case of an applied electric field of harmonic time-dependence ($\mathbf{E}(t) = \mathbf{E_0} e^{-i\omega t}$), the dielectric function of the metal-plasma is derived from the equation of motion of an individual electron. This evaluates to [37]

$$\varepsilon(\omega) = \varepsilon_1(\omega) + i\varepsilon_2(\omega) = 1 - \frac{\omega_p^2}{\omega^2 - i\gamma\omega} \tag{2.7}$$

ω_p is known as the plasma frequency and is defined in terms of the electron density n, the electron charge e, the relative permittivity of vacuum ε_0 and the effective optical mass m of the electron [28]

$$\omega_p = \frac{ne^2}{\varepsilon_0 m} \tag{2.8}$$

Damping is negligible for frequencies close to ω_p. In this frequency range the dielectric function is mainly real-valued and can be written as [37]

$$\varepsilon(\omega) = 1 - \frac{\omega_p^2}{\omega^2} \tag{2.9}$$

As can be seen from Eq. 2.9, the dielectric function of the metal is negative below the plasma frequency and hence, the refractive index ($n(\omega) = \sqrt{\varepsilon(\omega)}$) of the metal is complex valued. A complex valued refractive index implies that electromagnetic waves cannot propagate inside the material. The conduction electrons of the metal screen the electric field of light and incoming light of frequency $\omega < \omega_p$ is therefore reflected. If $\omega > \omega_p$ the conduction electrons cannot respond fast enough to screen the electric field of light, so the electromagnetic waves are transmitted [22]. The plasma frequency of most metals lie in the ultra-violet (UV) regime of the electromagnetic spectrum [28]. As a result, most metals are highly reflective to incoming light of visible frequencies.

Equation 2.9 cannot describe the electromagnetic response of noble metals, such as gold which is of prime importance in this thesis work. Noble metals experience interband transitions in the frequency range where Eq. 2.9 is valid. Interband transitions increase the imaginary part of the dielectric function [28] and are included in more sophisticated models. Nevertheless, the Drude model has a lot to offer with respect to underlying physics of the localized surface plasmon resonance effect outlined in the present chapter.

2.3 Surface Plasmon Polaritons

Surface plasmon polaritons (SPP) are electromagnetic surface waves that propagate along metal-dielectric interface(s). These surface waves originate from a coupling between the electromagnetic field of light and the oscillation of the conduction electrons of the metal [28]. The name polariton describe this coupled nature [22].

The amplitude of the electromagnetic field of a SPP decays exponentially into the metal and the dielectric. Such exponential decay is only possible when the real part of the dielectric functions of the two media is of opposite sign. As a consequence, SPPs are only excited at interfaces between a metal, in which $\mathrm{Re}[\varepsilon(\omega)] < 0$, and a dielectric [28].

Quantitatively, SPPs are described in terms of a dispersion relation derived from Maxwell's equations. In the case of two halfspaces, a metal, whose dielectric function is denoted $\varepsilon(\omega)$ and a dielectric with a constant and real relative permittivity ε_m the dispersion relation reads as follows [28]

$$\beta = k\sqrt{\frac{\varepsilon(\omega)\varepsilon_d}{\varepsilon(\omega)+\varepsilon_d}} \tag{2.10}$$

where β is called the propagation constant. β corresponds to the wave number in the direction of propagation and k is the wave number of the propagating wave in vacuum ($k = \frac{2\pi}{\lambda}$).

The SPP dispersion relation resides below the light-line ($k = \sqrt{\varepsilon}\frac{\omega}{c}$) of the dielectric. A direct crossing only occur in the limit $\omega = \beta = 0$. As a result, SPPs cannot be excited directly by light, since the momentum of SPPs ($\hbar\beta$) exceed the momentum of light ($\hbar k$) at any frequency. Special techniques for phase-matching, e.g. prism or grating coupling, need to be employed to excite SPPs [28].

SPP is a surface electromagnetic wave, whose electromagnetic field is confined to the near vicinity of a metal-dielectric interface. In fact, the electromagnetic energy of SPPs can be confined (squeezed) into volumes smaller than the diffraction limit. The fact that SPPs pave the way for sub-wavelength optics is of prime importance in plasmonics [28], especially with respect to applications in optical sensing [23].

2.4 Localized Surface Plasmons

As opposed to SPPs that propagate along a metal surface, localized surface plasmons (LSP) are non-propagating excitations of the conduction electrons of metal nanoparticles (MNPs) coupled to light. (Strictly speaking, the LSP is also a polarition, but this ending is usually omitted.) A surface plasmon confined in a metal nanostructure is termed a localized surface plasmon, schematically depicted in Fig. 2.1. The collective displacement of the conduction electrons relative to the fixed ion-cores sets up a restoring force. Hence, the metal nanoparticle in interaction with light can in its simplest form be studied as an oscillator. A resonance

condition arises when the frequency of light matches the eigenfrequency of the oscillator [22]. This resonance is termed localized surface plasmon resonance (LSPR). Among others, the LSPR give rise to an enhancement of the metal nanostructure ability to scatter and/or absorb light. The wavelength of LSPR excitation is a characteristic property of the metal and is highly sensitive to changes in the shape and size of the MNP as well as to changes in the surrounding medium. Furthermore, in an ensemble of MNPs, the resonance condition can be altered by interaction between neighboring particles as well as coupling via diffraction [28].

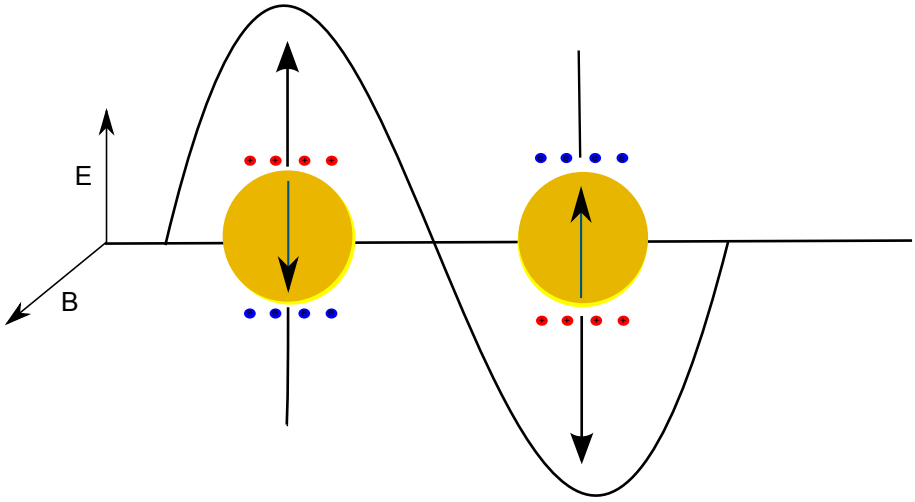

Figure 2.1: Schematics of a spherical MNPs in a electromagnetic field (light). The electric field of light displaces the conduction electrons of the MNP relative to the fixes ion cores. This displacement sets up a restoring force. Certain wavelength of light will induce a resonant oscillation of the conduction electrons. Redrawn from [21].

2.4.1 The Quasi-Static Approximation

The optical response of a single and isolated MNP, provided that the particle is much smaller than the wavelength of incoming light, is described by the so-called quasi-static approximation. Within this limit, retardation effects over the particle volume are neglected (i.e. the electric field is assumed to be spatially static). The interaction of light and the MNP is therefore governed by electrostatics rather than electrodynamics [38].

To arrive at the resonance condition, a homogenous and isotropic sphere of radius a ($a << \lambda$) located at the origin of a uniform electric field $\mathbf{E} = E_0\hat{\mathbf{z}}$ is considered. The sphere, whose dielectric function is assumed to be a complex number ε (neglecting frequency dependence), is embedded in a non-absorbing and isotropic medium with a dielectric constant denoted ε_m. The difference in permittivity between the sphere and the medium will induce a distortion of the initially uniform electric field. The electric fields outside and inside the sphere are derived from the Laplace equation [38, 28]

$$\bigtriangledown^2 \psi = 0 \tag{2.11}$$

where

$$-\bigtriangledown\psi = \mathbf{E} \tag{2.12}$$

in which ψ is the electrostatic potential. Due to the symmetry of the problem, the electrostatic potentials are independent of ϕ. The electrostatic potentials inside $\psi_{in}(r,\theta)$ and outside $\psi_{out}(r,\theta)$ the sphere are given as [28]

$$\psi_{in}(r,\theta) = \sum_{l=0}^{\infty}[A_l r^l]P_l(cos\theta) \tag{2.13a}$$

$$\psi_{out}(r,\theta) = \sum_{l=0}^{\infty}[B_l r^l + C_l r^{-(l+1)}]P_l(cos\theta) \tag{2.13b}$$

where $P_l(cos\theta)$ is associated the Lengrende Polynomials of order l. θ denotes the angle between the position vector $\mathbf{r}$ at point P and the z-axis (see Fig. 2.2). This general solution to Laplace equation has in principle an infinite number of solutions. However, by imposing boundary conditions to the solutions, the electrostatic potential is uniquely defined [35]. The boundary conditions read as follows [28]

$$-\frac{1}{a}\frac{\delta\psi_{in}}{\delta\theta}\mid_{r=a} = -\frac{1}{a}\frac{\delta\psi_{out}}{\delta\theta}\mid_{r=a} \tag{2.14a}$$

$$-\varepsilon_0\varepsilon\frac{\delta\psi_{in}}{\delta r}\mid_{r=a} = -\varepsilon_0\varepsilon_m\frac{\delta\psi_{out}}{\delta r}\mid_{r=a} \tag{2.14b}$$

The boundary conditions state that tangential electric field and the normal component of the electric displacement field must be continuous at the boundary of the sphere. Furthermore, far away from the sphere the electric field must approach $-E_0 z = -E_0 r\cos(\theta)$ [38]. This evaluates to [28]

$$\psi_{in}(r,\theta) = -\frac{3\varepsilon_m}{\varepsilon+2\varepsilon_m}E_0 r\cos\theta \tag{2.15a}$$

$$\psi_{out}(r,\theta) = -E_0 r\cos\theta + \frac{\varepsilon-\varepsilon_m}{\varepsilon+2\varepsilon_m}E_0 a^3\frac{\cos\theta}{r^2} = -E_0 r\cos\theta + \frac{\mathbf{p}\cdot\mathbf{r}}{4\pi\varepsilon_0\varepsilon_m r^3} \tag{2.15b}$$

where

$$\mathbf{p} = 4\pi\varepsilon_0\varepsilon_m a^3\frac{\varepsilon-\varepsilon_m}{\varepsilon+2\varepsilon_m}$$

E_0 is the amplitude of the electric field, r is the distance from the center of the sphere to a point P, θ is the angle between the position vector and the direction of E_0 and ε_0 the permittivity of vacuum. As can be seen from 2.15b, ψ_{out} is a superposition of the electric field of an ideal dipole, denoted $\mathbf{p}$, located at the sphere center and the applied electric field [38]. The applied electric field thus induces a dipole moment at the center of the sphere. The polarizability,

denoted α describes the capability of the sphere to be polarized by the electric field. The relationship between the polarizability and the dipole moment is given as [28]

$$\mathbf{p} = \varepsilon_0 \varepsilon_m \alpha \mathbf{E}_0 \tag{2.16}$$

The polarizability can thus be written as [28]

$$\alpha = 4\pi a^3 \frac{\varepsilon - \varepsilon_m}{\varepsilon + 2\varepsilon_m} \tag{2.17}$$

Equation 2.17 is the complex polarizability of a sub-wavelength sphere. A resonant enhancement of the polarizability is met when $|\varepsilon + 2\varepsilon_m|$ is a minimum. The resonance condition is, for a slow-varying or small $\mathrm{Im}[\varepsilon]$ around the minimum, given as [28]

$$\mathrm{Re}[\varepsilon(\omega)] = \varepsilon_1(\omega) = -2\varepsilon_m \tag{2.18}$$

Equation 2.18 is known as the Fröhlich condition and is a central result in the quasi-static approximation. The Fröhlich condition enlightens the dependency of the resonance frequency (or wavelength) upon the surrounding medium. As is evident from Eq. 2.18, the spectral position of the resonance red-shifts when ε_m increases. For a Drude metal of negligible damping (described by Eq. 2.9) embedded in air ($\varepsilon_m \approx 1$) [28], the resonance condition is satisfied when $\omega = \frac{\omega_p}{\sqrt{3}}$, while for a Drude metal embedded in glass ($\varepsilon_m \approx \sqrt{1.5}$) the Fröhlich condition is met at the frequency $\omega = \frac{\omega_p}{2}$. Hence, the spectral position of the LSPR can be tuned by changing the medium which surrounds the MNP [23].

The distribution of the electric fields inside and outside the sphere volume can be extracted from Eq. 2.12 and 2.15. This yields [28]

$$\mathbf{E_{in}} = \mathbf{E_0} \frac{2\varepsilon_m}{\varepsilon + 2\varepsilon_m} \tag{2.19a}$$

$$\mathbf{E_{out}} = \mathbf{E_0} + \frac{3\mathbf{n}(\mathbf{n}\cdot\mathbf{p}) - \mathbf{p}}{4\pi\varepsilon_0\varepsilon_m} \frac{1}{r^3} \tag{2.19b}$$

where $\mathbf{p}$ is the induced dipole moment defined in Eq. 2.15. As can be seen from Eq. 2.19a, the electric field inside the particle is homogeneous. However, as described in Section 2.3, electromagnetic fields decay exponentially into metals. As a consequence, the validity of the quasi-static approximation breaks down when the MNP is larger than the skin depth of the metal (the skin depth described how deeply radiation penetrates into the metal) [39]. It should also be noted that the electric field experiences a resonant enhancement when the Fröhlich condition is satisfied. This local field enhancement is a consequence of the fact that electromagnetic energy is confined to a very small volume. As in the case of SPP, confinement below the diffraction limit can be achieved. The magnitude of the electric field is limited by the fact that $\mathrm{Im}[\varepsilon(\omega)] \neq 0$. This limitation can in principle be reduced by introducing gain media, that

is, by embedding the MNPs in a medium where $\mathrm{Im}[\varepsilon_2] < 0$. In this case, the positive imaginary part of the dielectric function of the MNP can give rise to a complete cancellation of the denominator in Eq. 2.17 [28].

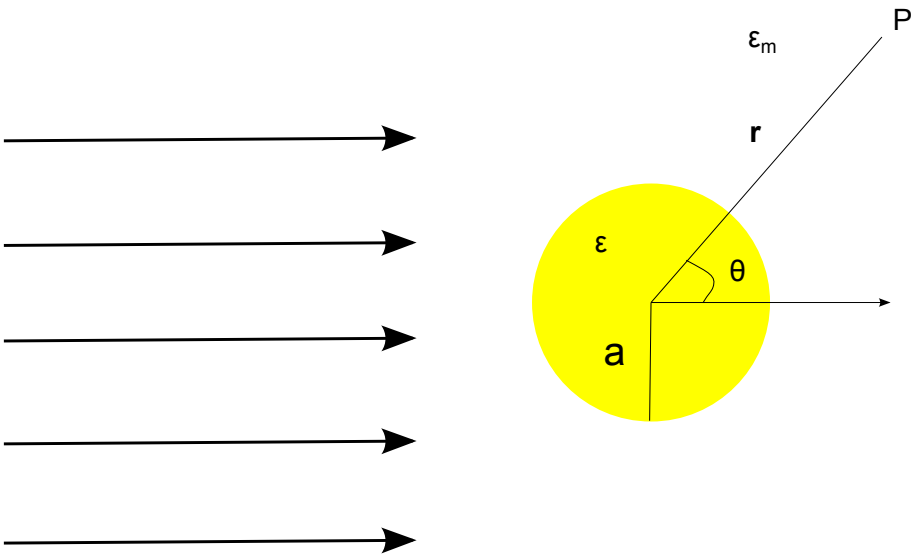

Figure 2.2: Sphere in a uniform electric field. The radius of the sphere is denoted a and the dielectric function of the sphere is assumed to be a complex number, denoted ε. The sphere is embedded in a dielectric medium whose dielectric constant is denoted ε_m. Redrawn from [38].

The metal sphere can, within the quasi-static regime, be described as an ideal dipole. This dipole scatters and absorbs light. When the Fröhlich condition is satisfied, the dipole strongly scatters and/or absorbs light. The cross-sections, that is, the likelihood of the particle to scatter or absorb light, is termed C_{sca} and C_{abs}, respectively [38]. In the quasi-static approximation C_{sca} and C_{abs} read as follows [28]

$$C_{sca} = \frac{k^4}{6\pi}|\alpha|^2 = \frac{8\pi}{3}k^4a^6\left|\frac{\varepsilon-\varepsilon_m}{\varepsilon+2\varepsilon_m}\right|^2 \tag{2.20a}$$

$$C_{abs} = kIm[\alpha] = 4\pi ka^3 Im\left[\frac{\varepsilon-\varepsilon_m}{\varepsilon+2\varepsilon_m}\right] \tag{2.20b}$$

where $k = \frac{2\pi}{\lambda}$ is the wave number, $|\alpha|$ the polarizability modulus and $\mathrm{Im}[\alpha]$ the imaginary component of the polarizability. Clearly, C_{sca} and C_{abs} experience a resonance enhancement when the Fröhlich condition is satisfied. Furthermore, as can be seen from Eq. 2.20, in small particles (rule of thumb $a < 50$ nm) the amount of light absorbed by the dipole (scaling as a^3) is greater than the amount of light scattered by the dipole (scaling as a^6). As a consequence, MNPs exhibit characteristic size-dependent colors in reflected and transmitted light [38].

Extinction is defined as the sum of absorption and scattering, that is, $C_{ext} = C_{sca} + C_{abs}$. The extinction cross-section of a sphere of volume V and dielectric function $\varepsilon(\omega) = \varepsilon_1(\omega) + i\varepsilon_2(\omega)$ is given as [28]

$$C_{ext} = 9\frac{\omega}{c}\varepsilon_m^{3/2}V\frac{\varepsilon_2}{[\varepsilon_1+2\varepsilon_m]^2+\varepsilon_2^2} \tag{2.21}$$

where c is the speed of light.

Other simple geometries, such as spheroids, can be described using the quasi-static approximation. In the case of spheroids, the polarizabliity α_i along principle axis i is given in terms of a geometrical factor. As a consequence, a spheroidal MNP support two distinct resonances caused by oscillations along the minor and major axis. The major axis resonance is redshifted relative to a sphere of the same volume. Hence, in addition to changing the surrounding medium, the spectral position of the LSPR can thus be tuned by changing the aspect ratio of the particle [28].

The metal nanoparticles studied within this thesis are produced with a nominal diameter of 30 nm or 45 nm. As a rule of thumb, the quasi-static approximation accounts for nanoparticles whose diameter is less than 100 nm. The extinction maximum of the produced arrays can therefore be predicted by the means of electrostatic theory. The EnSol solar cell will feature nanoparticles of diameters in the range 5 nm – 10 nm. Particles in this size regime are approaching the lower limit of particle dimensions that adequately can be described using the quasi-static approximation. When the MNPs are smaller than the mean free path of the conduction electrons, scattering of electrons at the surface of the particle give rise to an increase in in ε_2 of the metal. Hence, the bulk dielectric function can no longer be applied to describe the optical properties of the MNPs. So-called finite-size corrections can be included in the bulk dielectric function to account for this effect [40].

2.4.2 Mie Theory

The quasi-static approach does not include phase-changes of the incident electric field over the particle volume. As the size of a particle gets comparable to the wavelength of the electric field, retardation effects over the particle volume need to be included. G. Mie developed a complete analytical theory of scattering and absorption of electromagnetic radiation by a sphere of arbitrary size. It should be noted that the Mie theory includes the electrostatic solution of Maxwell's equations; the solution is Eq. 2.17 [41].

Although the optical properties particles produced within this thesis work can be described using the quasi-static approximation, the Mie theory reveal important properties of the LSPR effect that the quasi-static approximation cannot describe. In particular, Mie theory predicts a redshift [28] of the spectral position of the dipole resonance as the size of the particle increases. This can, qualitatively, be attributed to the larger distance between the conduction electrons and ion cores which causes a smaller restoring force and thus, a redshift of the resonance wavelength [38]. Furthermore, the retardation over the particle volume indicates the existence of higher-order resonances. Indeed, the larger the particle becomes, the more important are higher-order resonances and the oscillation of the conduction electrons can no longer

be described as one collective motion. Higher order resonances are excited at different wavelengths with respect to the dipole resonance [41].

2.5 Numerical Methods

Mie theory is an exact solution to Maxwell's equations. However, it is a single-particle approach and cannot describe the optical properties of interacting particles nor particles of complex shape. Numerous numerical methods have been developed to address either one or both of these issues. They all aim to solve Maxwell's equations using realistic boundary conditions in order to describe the optical properties of MNPs of arbitrary size and shape. These methods are constantly being improved and extended [42].

Effective Medium Theory

Effective medium theories describe the optical response of MNP(s) embedded in a dielectric medium. The heterogeneous system comprised of the MNP(s) and the ambient is represented as an effective medium characterized by an effective dielectric function [43]. The Maxwell-Garnett theory is an example of such an effective medium theory. It is an electrostatic approach and in the case of spherical MNPs the underlying principles are outlined in Section 2.4.1. However, a volume filling factor is needed in Eq. 2.17 to include the presence of multiple particles [27] and the electric field is replaced by a so-called local electric field. This local electric field incorporates contributions from the incoming electric field and the fields induced by neighboring particles [44].

In the case of substrate supported MNPs, such as MNPs deposited on a glass surface, the presence of the substrate induces a break of symmetry with respect to MNPs embedded in a homogenous medium. Including this symmetry-break by the means of an effective medium is a highly simplified approach [43].

Discrete Dipole Approximation

In the discrete dipole approximation (DDA) each MNP is represented as a cubic lattice of N polarizable points [26]. In interaction with an external electric field these points gain a dipole moment and can be studied as interacting dipoles. Any lattice point can be occupied, so the model can be used to describe the optical response of MNP of arbitrary shape. The polarization P at a given point r_j inside this cubic lattice is expressed in terms of a local electric field. This local electric field incorporates the incoming electric field as well as the induced electric field arising from interaction with other particles. Quantitatively, the polarization is given as [42]

$$P_j = \alpha_j E_{loc} \tag{2.22}$$

where E_{loc} is the local electric field at the point r_j and α_j is the polarizability. The polarizability is commonly expressed by the means of an extension of Eq. 2.17 [45]. DDA can be used to describe the optical response of substrate supported MNPs, like the ones produced in this work. The interaction between the substrate and the particles is described through the method of images charges [42], (described in greater detail in Chapter 3). As described above, the model can also describe the disk-shape form of the fabricated MNPs in this thesis work.

Boundary Element Method

In contrast to DDA where the whole volume of the MNP is divided into polarizable point, the boundary element method (BEM) only divide the boundaries of a particle into polarizable points [26]. The electromagnetic field inside each particle is therefore solely determined by the fields at the boundary of the particle [42].

The Bedeaux-Vlieger Model

The scientific software GranFilm [46], developed by Simonsen and Lazzari, has been used to calculate model extinction spectra in this thesis work. The software is based on the so-called Bedeaux-Vlieger model [47], an electrostatic model that describes the far-field optical properties of substrate supported MNPs. The MNPs are approximated as spheroids or spheres truncated by the substrate surface and substrate-particle interactions are described through the method of image charges. The transmittance of the MNP and thereby the extinction (described in Section 2.7), is found by solving Laplace equation through a multipolar expansion of the electrostatic potential [46]. A detailed description of the model can be found in Chapter 3.

The MNPs produced in the present work are disk-shaped, a particle shape that is not implemented in the GranFilm code. The disk-shaped MNPs are approximated as spheroids truncated by a glass substrates. The software was chosen because the code was available for use and the calculations themselves are not computationally demanding. Additionally, the model incorporates the presence of the substrate and includes interaction (up to quadrupolar order) between neighboring particles [43].

2.6 Resonant Properties of Metal Nanoparticles

The resonant properties of MNPs can be tuned by changing the constituent metal, the size and shape of the MNPs, the medium that surrounds the MNP(s), as well as the particle arrangement in the case of an ensemble of particles. This section summarizes the spectral trends of the LSPR, based on results from the quasi-static approximation and the Mie theory.

Constituent metal

The constituent metal is characterized in terms of its (bulk) dielectric function. Although, the dielectric function is given as a function of wavelength (or frequency), some general features can be extracted. Firstly, the wavelength of LSPR excitation is mainly determined by the shape and size of the MNP and the surrounding medium and, although to a less extent, by the real part of the dielectric function of the metal. Secondly, the LSPR linewidth (FWHM) is determined by the imaginary part of the dielectric function as well as by the size of the MNP and the polydispersity in size in the case of an ensemble of particles. The imaginary part of the dielectric function characterizes the LSPR damping mechanisms, which can be radiative or non-radiative in nature. In the former damping mechanism the energy stored in the LSPR basically decay via scattering of light. Non-radiative damping is associated with the generation of electron-hole pairs [48]. Electron-hole pairs can be generated via intraband excitations in the conduction band or via interband transitions, which in the case of noble metals is attributed to transitions from the d-orbital to the sp-orbital [28].

MNP size

The quasi-static approximation is strictly valid when the size of the particle is small compared to the wavelength of incoming light. Two size-regimes are not described by the electrostatic theory. Firstly, when the size of the particle increases, an electrodynamic approach is necessary, due to the retardation of the incoming EM field over the particle volume. As a rule of thumb, the electrostatic approach breaks down when the diameter of the MNP exceeds 100 nm [28]. Mie theory states that the spectral position of the (dipolar) LSPR redshifts with increasing particle and predict the existence of higher order resonances. Additionally, a broadening of the linewidth (FWHM) of the LSPR peak is expected as the MNP diameter increase, due to the increase in radiative damping of the resonance (see Eq. 2.20). Secondly, when the size of the particle is less than the free mean path of it's oscillating electrons, surface collisions give rise to damping (an increase in ε_2) and the dielectric function of the MNP changes with respect to the dielectric function of the bulk metal. These so called finite-size effects have been shown to give rise to a broadening of the linewidth of the LSPR peak [49].

MNP shape

Isolated spheres exhibit a single LSPR peak due to their high symmetry. This is, however, not the case for asymmetric particles. In the case of a spheroidal metal nanoparticle two spectrally separated LSPR can be observed, corresponding to electrons oscillating along the minor and major axis of the spheroid. Within the electrostatic regime, it can be shown that the dipole resonance along the major axis gradually redshifts as the aspect ratio increases with respect to a sphere of the same volume [28]. If the metal nanoparticle has the shape of an ellipsoid, three

distinct LSPR can be observed. Furthermore, for certain asymmetric particle shapes higher order resonances can be observed in the electrostatic limit. For example, in a cubic MNP the displaced conduction electrons are not distributed homogenously on the surface of the particle and higher order resonances can therefore be excited [50].

LSPR of complex structures can be studied as a hybridization of plasmons of simpler sub-structures. A metallic shell with a dielectric core can in this respect be represented as a hybrid of a metal sphere and a metal containing a spherical dielectric cavity. Firstly, a redshifted resonance with respect to the sub-structures is obtained for in-phase oscillation (i.e. bonding combination) of the metal sphere and the spherical cavity, whereas the anti-phase combination (i.e. anti-bonding combination) results in a blueshift of the LSPR [39].

Surrounding medium

The dependence of the spectral position of the LSPR upon the dielectric properties of the surrounding medium, is clearly stated in the Frönlich conduction (see Eq. 2.18). If the surrounding medium possesses a frequency-independent real and positive refractive index ($n = \sqrt{\varepsilon}$) an increase in the refractive index will cause a redshift of the LSPR.

Near-Field Coupling

In the case of an ensemble of particles, interactions between neighboring particles can change the LSPR wavelength to that of an isolated particle[28]. Such particle-particle coupling occurs when the center-to-center distance between neighboring particles is less than 3 times the particle diameter [25]. Rechberger et al. [25] studied a system consisting of two MNPs interacting via their near-field. They found that if the polarization of the incident light was parallel to the long pair axis, there was a weakening of the restoring force on the oscillating conduction electrons, due to the Coulomb attraction between the two particles, as indicated in the left panel of Fig. 2.3. This resulted in a red-shift of the spectral position of the LSPR with respect to an isolated particle. On the other hand, when the polarization of the incident light was normal to the long pair axis the restoring force increased, due to the Coulomb repulsion between the two particles (see right panel of Fig. 2.3) and a blue-shift was observed [25].

Far-field Effects

Periodic (ordered) MNP arrays can also be subjected to far-field coupling via diffraction [28]. Coupling via diffraction originates from the periodicity of the array, that is, the grating constant of the array. The grating constant determines the direction of propagation of light scattered from the MNPs. Temple et al. [51] studied the effect of the periodicity by fabricating a periodic sqaure array and a random array of MNPs of equal surface coverage. The diameter of the MNPs was in both cases 150 nm and the interparticle distance in periodic array was

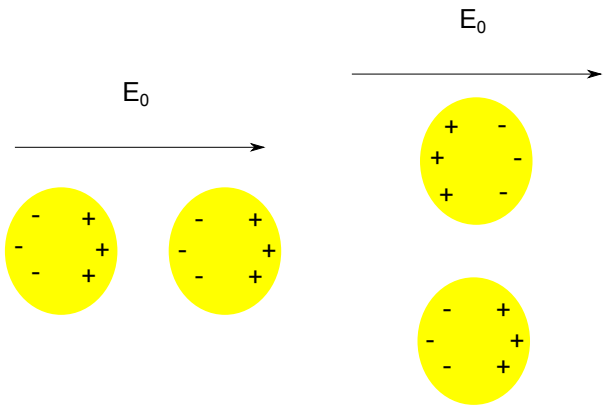

Figure 2.3: Schematic of particle-particle coupling for different polarization of incident light. Redrawn from [25]

500 nm. They found that the extinction efficiency of the two arrays was significantly different. The spectrum of the random array comprised a symmetric, broad peak, while the periodic array featured a narrower and more asymmetric peak. This discrepancy was attributed to the suppression and enhancement of scattering at different wavelengths caused by grating orders in the periodic array.

2.7 Spectroscopy

The optical properties of MNPs deposited on a non-conductive glass substrate are in this thesis work studied by the means of integrating spheres. The integrating sphere set-up employed is inspired by the work of Langhammer et al. [52] and is described in greater detail in Chapter 4.6. The experimental procedure is presented in Chapter 5.3, while the results from the optical analysis can be found in Chapter 6.4. The relative contributions of absorption and scattering to the total extinction of the MNPs can be separated using an integrating sphere, as the inner surface of the sphere is coated with a highly reflective and diffuse material that scatters light in all spatial directions with equal amounts. The sum of the total amount of light transmitted through the sample (i.e. MNPs and glass in this work) and the total amount of light reflected by the sample equals the amount of light scattered by the sample [52]. The light absorbed by the MNPs is then simply found as a consequence of conservation of energy [47]

$$1 = R + T + A \tag{2.23}$$

in which R is the reflectance, T is the transmittance and A the amount light absorbed by the MNPs. Reflectance is defined as the ratio of the intensity of the reflected light to the intensity of the incident light. In this thesis work the reflectance is calculated as [53]

$$R(\lambda) = \left(\frac{I(\lambda) - I_{B2}(\lambda)}{I_R(\lambda) - I_{B1}(\lambda)} \right) \cdot 0.98 \tag{2.24}$$

where $I(\lambda)$ is the intensity of light reflected by the sample and $I_{B2}(\lambda)$ the corresponding dark spectrum (light source blocked). $I_R(\lambda)$ is the intensity of light reflected by a reference standard, which is a standard coated with the sphere material. $I_{B1}(\lambda)$ is intensity of the dark spectrum of the reference standard. The reflectance of the sphere is 0.98.

Transmittance is defined as the ratio of the intensity of the transmitted light to the intensity of the incident light. The transmittance is calculated as [53]

$$T(\lambda) = \frac{I^{'}(\lambda) - I^{'}_{B2}(\lambda)}{I^{'}_{T}(\lambda) - I^{'}_{B1}(\lambda)} \tag{2.25}$$

where $I^{'}(\lambda)$ is the intensity of the light transmitted through the sample and $I^{'}_{B2}(\lambda)$ the corresponding dark spectrum. $I^{'}_{T}(\lambda)$ is the intensity collected at the transmittance port when the spheres are empty and $I^{'}_{B1}(\lambda)$ the corresponding dark spectrum.

The relationship between the extinction cross-section and the absorbance of a diluted sample is given by Beer-Lamberts law as [28]

$$A(\lambda) = \alpha_{ext}\tau \tag{2.26}$$

where $A(\lambda)$ is the absorbance, α_{ext} the absorption coefficient and τ the optical path length. The absorption coefficient can be written in terms of the scattering -, absorption-, and extinction cross-section of an isolated particle, given as

$$\alpha_{ext}(\lambda) = f(C_{sca}(\lambda) + C_{abs}(\lambda) = f(C_{ext}(\lambda)) \tag{2.27}$$

where f is a volume-filling factor. The calculated absorbance, in the case of particles situated on a transparent substrate, is in several cases (such as by Rechberger et al. [25]) directly termed extinction. This evaluates to [25]

$$\text{Extinction} = \text{Absorbance} = -\log(\text{Transmittance}) \tag{2.28}$$

In this thesis work the extinction of the MNPs have been calculated as presented in Eq. 2.28. In order to exclude substrate effects, the extinction of a bare glass substrate was subtracted from the extinction of the sample (i.e. MNPs and glass), as follows

$$\text{Extinction}_{MNP} = \text{Extinction}_{sample} - \text{Extinction}_{glass} \tag{2.29}$$

Chapter 3

Numerical Modeling: GranFilm

This chapter presents the underlying theory of the scientific software GranFilm [46]. GranFilm is employed to calculate the transmittance of square arrays of prolate and oblate spheroidal MNPs truncated by a glass substrate in order to obtain model extinction spectra. In addition to the transmittance, the reflectance as well as the amount of light absorbed by the MNPs can be accessed from the simulation. The results are presented in Chapter 6.5, while an introduction to other numerical methods can be found in Chapter 2.5.

The GranFilm code, developed by I. Simonsen and R. Lazzari [46], is based on the so-called Bedeaux-Vlieger model. The Bedeaux-Vlieger model describes the optical response of substrate supported nanoparticles by the means of electromagnetic excess field and surface susceptibilities [47]. The present chapter provides a short introduction to the Bedeaux-Vlieger model, followed by a description of underlying principles of GranFilm.

3.1 The Bedeaux-Vlieger model

The Bedeaux-Vlieger model [54] is grounded in classical electromagnetism. The fundamental objective of the model is to solve Maxwell's equations (Eq. 2.1) for substrate supported nanoparticles. The presence of the nanoparticles at the substrate surface is described as a distortion relative to a bare interface between two bulk media. This distortion can, within the electrostatic regime, be characterized in terms of auxiliary electromagnetic excess fields. The excess of the electric field $\mathbf{E}_{ex}$ is defined in terms of the actual, real electric field at the substrate surface $\mathbf{E}(\mathbf{r},t)$ and the electric fields far away from the substrate surface $\mathbf{E}^{\pm}(\mathbf{r},t)$ extrapolated to the interface. The superscript of $\mathbf{E}^{\pm}(\mathbf{r},t)$ denote the regions above (+) and below (-) the substrate surface. The excess of the electric field reads as follows [47, 55, 56]:

$$\mathbf{E}_{ex}(\mathbf{r},t) = \mathbf{E}(\mathbf{r},t) - \mathbf{E}^{-}(\mathbf{r},t)\theta(-z) - \mathbf{E}^{+}(\mathbf{r},t)\theta(z) \tag{3.1}$$

The plane $z = 0$ is defined to coincide with the substrate surface [55, 56]. $\theta(\pm z)$ is the so-called Heaviside step function. $\theta(z) = 0$ for $z < 0$ and $\theta(z) = 1$ for $z > 0$ [57]. The role of

$\theta(\pm z)$ is to "switch off" the electric field. The excess field is only significantly different from zero close to the substrate surface, since $\mathbf{E}(\mathbf{r},t) = \mathbf{E}^{\pm}(\mathbf{r},t)$ as $z \to \infty$ [55, 56]. Excess of other quantities are defined in an analogous manner [47].

The boundary condition imposed on $\mathbf{E}^{\pm}(\mathbf{r},t)$ at the substrate surface can be expressed in terms of these excess fields [47]. In this way, exact knowledge about the near-field is not required to gain information about the far-field (macroscopic) optical response of the substrate supported MNPs. Of course, this also means that information about the near-field of the MNPs is not gained. The total integrated excess fields are termed surface susceptibilities. The surface susceptibilities, denoted γ and β, describe the capability of the substrate surface to polarize upon interaction with light [44]. In the case of non-magnetic materials, such as MNPs, the surface susceptibilities are given as a function of the polarizabilities of the particles. As the Bedeaux-Vlieger model is valid in the electrostatic regime, the polarizabilities are found by solving Laplace equation (see Eq. 2.11).

3.2 The GranFilm approach

3.2.1 Particle shape

The Bedeaux-Vlieger model deals with two particle geometries – spheres and oblate or prolate spheroids [47]. These particle shapes encompass a great number of experimental situations and have been implemented into the GranFilm software. However, GranFilm models spheres or spheroids that are *truncated* by the substrate [46, 43], schematically depicted in Fig. 3.1.

The surface susceptibilities is a characteristic property of a boundary [55], meaning that the exact form of the surface susceptibilities of a sphere differ from those of a spheroid. The MNP arrays fabricated in this thesis work are disk-shaped. The particle shape of the GranFilm library that resembles a disk the most is a spheroid. A spheroid is an ellipse rotated around one of its axes. An ellipsoid rotated around its minor axis yields an oblate spheroid, while rotation around major axis of the ellipsoid yields a prolate spheroid [57, 55]. Hence, a spheroid is defined in terms of two radii, one of which corresponds to the particle radius while the other represents the height of the particle. Model extinction spectra are calculated for oblate and prolate spheroids. However, due to the complexity of the derivation of the spheroidal NP polarizabilities, the discussion in this chapter presents the model applied to spherical particles, since the aim is to highlight the physics rather than getting bogged down in mathematical notation.

3.2.2 The Truncated Sphere

A cross-section of a truncated sphere is depicted in Fig. 3.1. The truncation of the substrate surface, located at $z = d$ is expressed through a truncation ratio. The truncation ratio t_r is

defined as [55]

$$t_r = \frac{d}{R_\perp} \tag{3.2}$$

t_r is defined in the range $-1 < t_r < 1$. A sphere of truncation ratio -1 is completely buried in the substrate, while a truncation ratio of $+1$ resembles a sphere sitting on top of the substrate surface. [43].

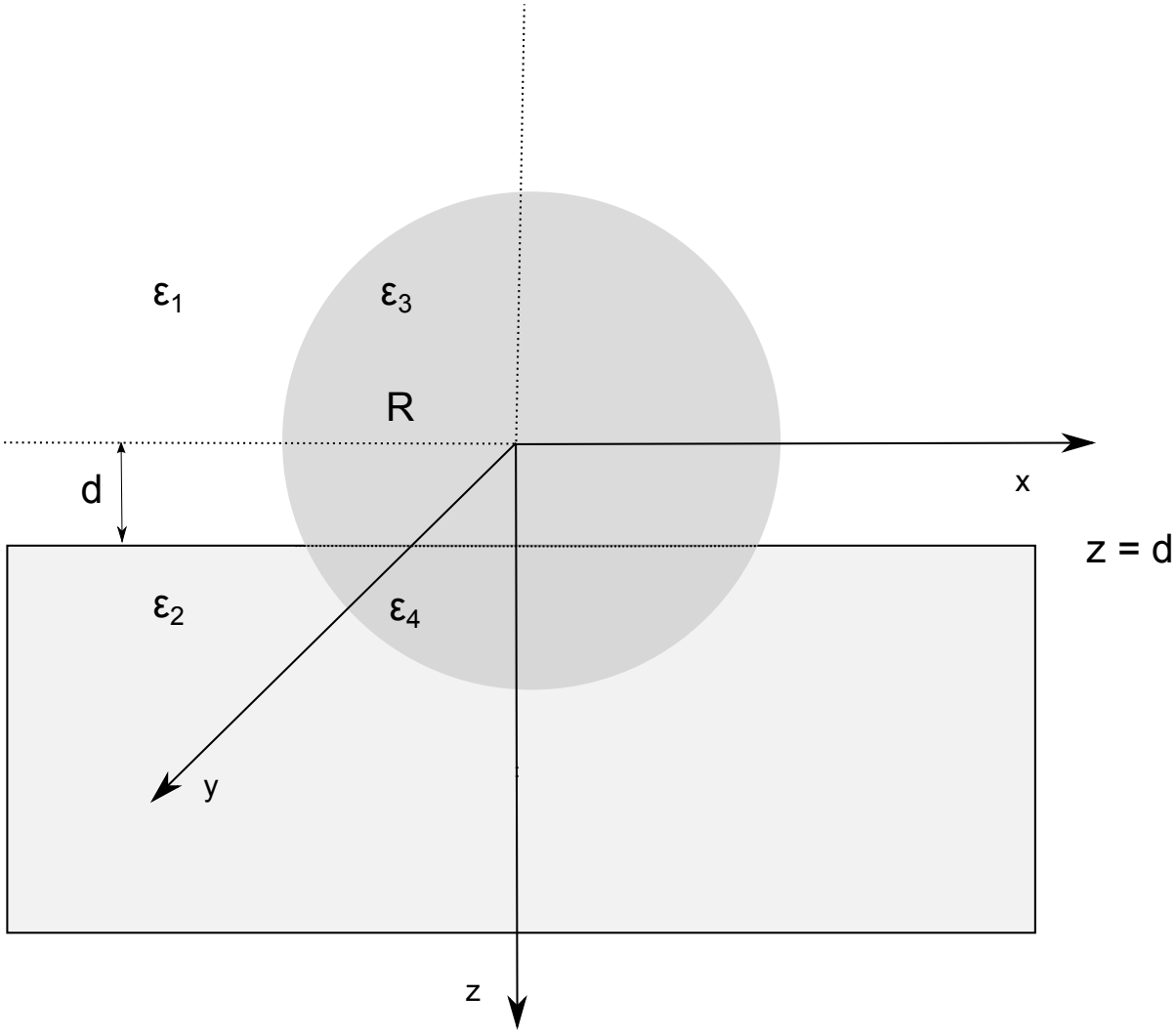

Figure 3.1: Cross-section of a truncated sphere. The origin of a Cartesian coordinate system is defined to coincide with the center of the sphere and the substate surface is located at a distance $z = d$ from the origin. The radius of the sphere is denoted R. The system is divided into four different regions, labeled in terms of their dielectric functions ε_1 - ε_4. Redrawn from [46].

The center of the main spherical coordinate system (r, θ, ϕ) is defined to coincide with the center of the sphere. Additionally, two reference frames, defined in the following section, will be used to find the polarizabilities of the substrate supported sphere [46].

3.2.3 The polarizabilities

The polarizabilities of the MNPs is found by solving Laplace equation through a multipole expansion of the electrostatic potential [43]. It is assumed that the magnitude of the interparticle distance is large compared to the size of the sphere. The calculation thus revolves around one isolated spherical particle. Interactions between neighboring particles are subsequently included by renormalizing the polarizabilities. The presence of the substrate induces a break of symmetry with respect to an isolated MNP subjected to an electric field (described in Chapter 2.4.1). The incident electric field induces a dipole moment inside the MNP. This dipolar electric field polarizes the substrate which in turn distorts the near-field of the MNPs. As a consequence, the quadrupolar polarizabilities of the MNP are excited. This series of polarization processes goes to high multipolar order and is modeled using the method of image charges [43, 58]. In this method the image of the charge distribution inside the MNP is introduced in the substrate [35].

The spherical MNP is submitted to a homogeneous electric field [43]. The objective is to solve the Laplace equation $\bigtriangledown^2\psi(\mathbf{r}) = 0$ to obtain an expression of the polarizabilities of the MNP [46]. As described in Chapter 2, Laplace equation has in principle an infinite number of solutions. However, by applying boundary conditions (given in Eq. 2.14) the potential is uniquely defined [35]. The boundary condition imposed on the solutions of the Laplace equation should be fulfilled or any two media sharing an interface. Additionally, the potential itself must remain finite everywhere, in particular when $r = 0$ and as $r \to \infty$ [55].

Laplace equation is solved separately in all four media depicted in Fig. 3.1. Laplace equation is homogenous and linear so any linear combination of solutions is also a solution. In the surrounding medium (i.e. medium 1 in Fig. 3.1) the electrostatic potential reads as follows [46]

$$\psi_1(r) = \psi_0(r) + \sum_{lm}^{l\neq 0} A_{lm} r^{-(l+1)} Y_l^m(\theta,\phi) + \sum_{lm}^{l\neq 0} A_{lm}^r \rho^{-(l+1)} Y_l^m(\theta^r,\phi^r) \tag{3.3}$$

Eq. 3.3 is known as a spherical multipole expansion. The source of the expansion is known as a multipole expansion point [56]. Eq. 3.3 has such two sources, denoted (r^r,θ^r,ϕ^r) and (ρ^r,θ^r,ϕ^r). (r^r,θ^r,ϕ^r) describes the contribution of the induced multipoles in the particle to the total potential, while (ρ^r,θ^r,ϕ^r) described the contribution of the image multipoles in the substrate to the total potential [56, 46]. (r^r,θ^r,ϕ^r) and (ρ^r,θ^r,ϕ^r) are located on the z-axis in Fig. 3.1 equidistant from the substrate surface [46]. $\psi(r)$ is the incoming potential, while A_{lm} and A_{lm}^r is the so-called expansion coefficients of (r^r,θ^r,ϕ^r) and (ρ^r,θ^r,ϕ^r), respectively. The expansion coefficients are determined by imposing boundary conditions on the electrostatic potential [47]. l and m are in principle defined as follows [47]

$$l = 0,1,2,....$$

$$m = 0, \pm 1, \pm 2, ..., \pm l$$

Since there are no free charges in the system, $l = 0$ is not included in the summation in Eq. 3.3 [47]. The spherical harmonics $Y_l^m(\theta, \phi)$ of order l and degree m is given as follows [59]

$$Y_l^m(\theta, \phi) = \sqrt{\frac{(2l+1)[(l-m)!]}{4\pi[(l+m)!]}} P_l^m(\cos(\theta))(-1)^m e^{im\phi} \tag{3.5}$$

in which $P_l^m(\cos(\theta))$ is the associated Legrendre function [59].

The electrostatic potential in the other media are expressed in an analogous manner [43]. It should be noted that there is images charges do not contribute to the total potential in the regions below the substrate surface [46, 35].

The electrostatic potential of the substrate supported MNP is strongly related to Eq. 2.13. While the latter describes the optical response of a particle embedded in a homogenous medium, the former includes the presence of a substrate as well as the interaction between the substrate and the MNP.

In order to obtain an expression for the expansion coefficients, the boundary conditions, defined in Eq. 2.14, are imposed on Eq. 3.5 and its equivalents. This gives rise to a linear system of equations for the expansion coefficients A_{lm} and B_{lm} [43]. Once the expansions coefficients are known, the electric field (derived from Eq. 2.12) can be determined – and thus the polarizabilities of the substrate supported nanoparticle can be obtained [55].

The polarizabilities of a sphere in a homogenous medium is given by Eq. 2.17. In the case of a substrate supported particle, the introduction of the image charges in the substrate causes the polarizabilities of the particle to be different parallel and perpendicular to the substrate surface [47]. The polarizabilities of the sphere are found through a multipole expansion of the polarization. To dipolar order the polarizabilities read as follows [59]

$$\alpha_\perp = \frac{2\pi\varepsilon_1}{\sqrt{\frac{2\pi}{3}} E_0 \cos\theta_0} A_{10} \tag{3.6}$$

$$\alpha_{||} = -\frac{4\pi\varepsilon_1}{\sqrt{\frac{2\pi}{3}} E_0 \sin\theta_0 e^{-i\phi_0}} A_{11} \tag{3.7}$$

where $\alpha_{||}$ and α_z are the dipolar polarizabilities of the particle, parallel and perpendicular to the substrate surface, respectively. A_{10} is the expansion coefficient of degree 1 and order 0 and A_{11} is the expansion coefficient of order 1 and degree 1.

In order to account for the interactions of a given sphere with neighboring sphere and their images the polarizabilities are renormalized [43]. Within this work, interactions between neighboring particles are included to a dipolar order. Simonsen and Lazzari [46] demonstrated that modeling the interaction of neighboring particles using this dipole approximation was sufficient when the surface coverage is less than 50 %. Furthermore, difference between the

dipolar and quadrupolar order was found to be negligible.

3.3 The Surface Susceptibilities

The capability of the interface to polarize parallel (γ) and perpendicular (β) upon interaction with light is described by the surface susceptibilities. The surface susceptibilities are related to the polarizabilities of the MNP as follows [46]

$$\beta = \rho\,\alpha_{\perp} \tag{3.8a}$$

$$\gamma = \rho\,\alpha_{||} \tag{3.8b}$$

where ρ is the density of the particles i.e. the number of particles per unit area [55].

3.4 Reflectance, Transmittance and Absorption

Light incident on a surface, defined as an interface between two bulk media of different refractive indices, is partly transmitted and partly reflected. By imposing boundary conditions to Maxwell's equation (see Eq. 2.1) the amplitude of the reflected and transmitted waves, denoted r and t respectively, can be found. In the case of parallel polarization to the plane of incidence the amplitude of reflection and transmission read as follows [55, 47]

$$r_{\parallel} = \frac{n_t \cos\theta_i - n_i \cos\theta_t}{n_i \cos\theta_t + n_t \cos\theta_i} \tag{3.9a}$$

$$t_{\parallel} = \frac{2n_i \cos\theta_i}{n_i \cos\theta_t + n_t \cos\theta_i} \tag{3.9b}$$

In the case of perpendicular polarization to the plane of incidence, the amplitudes are defined as [55]

$$r_{\perp} = \frac{n_i \cos\theta_i - n_t \cos\theta_t}{n_i \cos\theta_i + n_t \cos\theta_t} \tag{3.10a}$$

$$t_{\perp} = \frac{2n_i \cos\theta_i}{n_i \cos\theta_i + n_t \cos\theta_t} \tag{3.10b}$$

where the subscript $\parallel$ and $\perp$ denoted the polarization of incident light. n_i and n_t are the refractive indices of the media above and below the interface, respectively. θ_i the angle of incidence and θ_t the angle of transmission. Equation 3.9 and 3.10 are known as the Fresnel coefficients and characterize the optical properties of the interface.

In the theoretical calculations of this thesis work, light is incident normal to the substrate surface. At normal incidence there is no difference between paralell- and perpendicular- polarized light [47]. The reflection and transmission amplitudes can be written in terms of the

surface susceptibilities [43]. These will differ from the amplitudes of a bare interface (the so-called Fresnel coefficients described above), due to the boundary conditions imposed on the solutions of Laplace equation. At normal incidence the reflection and transmission amplitude, given as a function of the surface susceptibilities, read as follows [55, 43]

$$r = \frac{\sqrt{\varepsilon_1} - \sqrt{\varepsilon_2}\cos(\theta_t) + i\frac{\omega}{c}\gamma}{\sqrt{\varepsilon_1} + \sqrt{\varepsilon_2}\cos(\theta_t) - i\frac{\omega}{c}\gamma} \tag{3.11}$$

$$t = \frac{2\sqrt{\varepsilon_1}}{\sqrt{\varepsilon_1} + \sqrt{\varepsilon_2}\cos(\theta_t) - i\frac{\omega}{c}\gamma} \tag{3.12}$$

where ε_1 and ε_2 are the dielectric functions of medium 1 and 2, respectively (see Fig. 3.1). θ_t is the angle of transmission [43].

The reflectance R and transmittance T, defined in Chapter 2.7, can be written in terms of the amplitude of reflection and transmission [43]

$$R = |r|^2 \tag{3.13}$$

$$T = |t|^2 \frac{\sqrt{\varepsilon_2}\cos(\theta_t)}{\sqrt{\varepsilon_1}} \tag{3.14}$$

The amount of light absorb by the MNP is simply found as a consequence of conservation of energy.

3.5 The software

The first code of GranFilm [46] was written in FORTRAN 90 programming language by Ingve Simonsen and Remi Lazarri. This code, which focused on truncated spheres on a substrate, has been developed to also support truncated spheroids [55, 56, 43]. The software can be freely downloaded from [60] and is available for Mac OSX, Linux and Windows. It is a terminal program, which provides a text-formatted parameter file as input and producing a datadase (.dat) file as output.

GRANFILM is connected to the dielectric database SOPRA [61]. The database consists of a great variety of materials, ranging from metals to dielectrics. One drawback with the SOPRA database is that, for most materials, there is no information of how the sample was prepared or how the dielectric function was measured. Additionally, the database only contains bulk dielectric functions and hence there exists a lower limit with regard to the size of the MNPs. When the size of the particle becomes comparable to the mean free path of the conduction electrons the dielectric function changes with respect to the bulk dielectric function [40].

In the theoretical calculations of this thesis work, the square arrays of MNPs are modeled as truncated spheroids with a truncation ratio of zero . A truncation ratio of zero corresponds to

a spheroid in which half of the spheroid is on top of the substrate while the other half is buried inside the substrate. A truncation ratio of zero was chosen for the simplicity it provides with respect to defining the radii of the spheroids. The spheroids are defined in terms of two radii, corresponding to the experimental height and radius. The height is kept constant, while the radius varies according to the radius of the fabricated MNPs in this thesis work and in the work presented by Håvardstun [9] and Greve et al. [73]. Model extinction spectra are presented in Chapter 6.5.

3.5.1 Limitations

The Bedeaux-Vlieger model is strictly valid within the electrostatic regime. Two particle sizes are not captured by this theory. Firstly, larger MNPs cannot be described adequacy using the GranFilm software, since the Bedeaux-Vlieger model breaks down due to retardation effects over the particle volume. Secondly, particle dimensions considerably smaller than the free mean path of the conduction electrons cannot be described by the bulk dielectric function of the metal. Although not relevant in this work, so-called finite-size corrections of the dielectric function have been implemented into the GranFilm software [54, 56].

Truncated spheres and spheroids are the only particle shapes that have been implemented into the GranFilm software [43]. The LSPR wavelength is highly dependent upon the shape of the MNP [28]. The fabricated MNPs in this thesis work are disk-shaped. There are therefore discrepancies between the optical responses, in particular the LSPR wavelength, of the model and experimental MNP systems.

The surface susceptibilites govern the far-field optical properties, such as the transmittance and reflectance. However, no information about the near-field is gained. If higher order resonances are present, these may not survive to the far-field, and will therefore not be detected using the GranFilm software.

Chapter 4

Experimental Equipment

The present chapter describes the experimental equipment used to produce large arrays of MNPs situated on a non-conductive substrate, as well as the equipment used to characterize the arrays with respect to structure (size, interparticle distance and height) and optical properties. The starting point is a discussion of the underlying principles of the combined electron beam lithography (EBL) and scanning electron microscopy (SEM) system, followed by a description of the metal deposition system, the thin film analyzer and the integrating sphere set-up. The experimental procedure is described in Chapter 5. The main emphasis in this Chapter and following Chapter has been on the description of instrumentation and methods that have been established during this thesis work.

4.1 The NanoStructure Laboratory at UiB

The majority of the experimental work conducted in this thesis is performed in the Nanostructure laboratory at UiB, located at the Department of Physics and Technology. The laboratory is divided into four sections; an ISO 5 standardized cleanroom, an ISO 7 standardized cleanroom cabinet, a semi-clean room and a storage room. The ISO standard of a cleanroom is based on the maximum number of particles larger than 0.1 μm permitted in a cubic meter (particles/m^3). Outdoor air is classified as an ISO 9 standard and the allowed number of particles/m^3 decreases with standard number [62]. To maintain the cleanness of a cleanroom, temperature-controlled pressurized air enters the room through filters in the ceiling. This creates a positive pressure that forces airborne particle contamination to exit the room through integrated gaps at floor level. All personnel working in the laboratory must follow a dress code to minimize the introduction of particle contamination.

The ISO 5 cleanroom hosts a fume hood and the thin-film analyzer, which in this thesis work is used for sample processing and thickness measurements, respectively. The electron beam lithography system is located in the ISO 7 standardized cleanroom cabinet, while the semi-clean room hosts the electron beam evaporator (i.e. metal deposition system).

4.2 Electron-Beam Lithography

Electron beam lithography (EBL) comprises scanning a highly focused electron beam across a surface coated with an electron-sensitive film. This electron-sensitive film, termed resist, changes chemically upon exposure according to the energy deposited by the electron beam, so that the exposed (un-exposed) areas can be selectively dissolved in an appropriate developer solvent. For so-called positive-tone resists the developer solvent eliminates the exposed areas, whereas for negative-tone resists the invers occurs [63].

The working principle of EBL is very similar to any other lithography technique. However, EBL does not require the use of a mask such as e.g. optical lithography, in which visible or UV-light is used to form a pattern defined by a mask placed between the light source and a light-sensitive resist (photoresist). The use of a mask allows for instant exposure, but the mask basically acts as a set of slits, so the final resolution is limited by diffraction. EBL, on the other hand, allows for very high resolution (resolution of sub-10 nm scales has been demonstrated [64]). However, as the pattern is defined by scanning the beam across the surface of the sample, the throughput is low; EBL can be several orders of magnitude slower than optical lithography [64].

4.2.1 Raith E-line Electron Beam Lithography System

The EBL system (Raith E-line) in the UoB Nanostructures facility is depicted in Fig. 4.1. It is essentially a scanning electron microscope (SEM) to which a beam blanker, a high-precision laser-interferometer controlled sample stage and a pattern generator have been added. These additional features make it possible to write in a highly selective manner by the means of a focused electron beam [63].

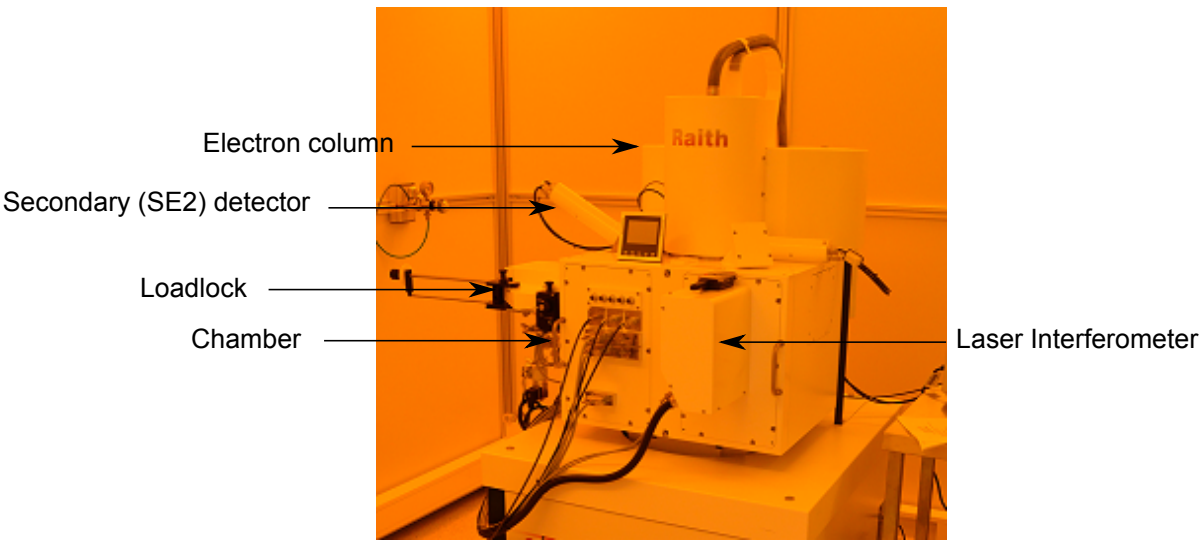

Figure 4.1: Electron beam lithography system in UiB Nanostricture laboratory. Note that the high-speed-patterning computer system is not depicted.

The electron beam is generated in the so-called electron column, schematically illustrated in Fig. 4.2. Electrons are extracted from a filament by applying a voltage between a cathode (i.e. the filament) and an anode and the acceleration voltage is determined by the potential difference between the two. The maximum acceleration voltage of the Raith e-line system is 30 keV. The aperture is a beam-width limiting hole, of which there are six in the range 7.5 µm and 120 µm. Electromagnetic lenses focuses the electron beam onto the sample surface and scanning coils control and move its position with respect to the sample surface. Finally, an electrostatic deflector operate as a beam-blanker [21]. The system is equipped with two secondary-electron detectors: an InLens detector and a secondary electron (SE2) detector. Secondary electrons are generated through the ionization of sample (i.e. resist and substrate) electrons [63]. The InLens detector only collects secondary electrons directly emitted from the sample volume, while the positively-biased electrode SE2 detector additionally detect secondary electrons generated when backscattered electrons (defined and discussed in Section 4.3) bounce off the wall of the chamber. As illustrated in Fig. 4.2, the SE2 detector is located at an angle with respect to the sample plane. Topographic information can thus be extracted from these signals. As SEM imaging involves the bombardment of electrons on a surface, non-conductive samples will accumulate charge causing a substantial drift of the electron beam which in turn gives rise to significant image distortions. To prevent such charging effects, non-conductive samples can be coated with a charge-dissipating layer (e.g. a metal).

The Raith E-line system has a CAD (Computer-Aided-Design) software for designing and editing patterns. The size of the CAD corresponds to the area over which the electron beam scans just by deflecting the beam. If this area exceeds a certain size, the resolution is reduced [65]. To maintain a high resolution, the pattern can be divided into several smaller components called write-fields (typically 100 µm $\times$ 100 µm). Neighboring write-fields are stitched together by moving the sample stage, which is measured and controlled by the laser interferometer. Alternatively, large and continuous pattern can be written in fixed-beam-moving-stage mode (FBMS mode). However, FBMS can only be used to pattern area, lines and circles.

The number of electrons deposited by the electron beam per area (or point) is termed exposure dose. In this thesis work, large periodic arrays of zero dimensional points (dots) were produced. The exposure dose of a dot is defined as [65]

$$\text{Dot dose [pC]} = \text{Dwell Time [ms]} \times \text{Beam Current [nA]} \tag{4.1}$$

The dwell time is defined as the period of time the beam exposes each point and can thus be changed by adjusting the exposure dose and/or the beam current. The latter is directly proportional to the area of the aperture. Consequently, reducing the aperture will increase the write-time. Additionally, the beam current depends upon the state of the filament. It should be noted, as described in the following section, that the exposure resolution of the electron beam is not solely dependent upon the pre-determined exposure dose. Interaction between the

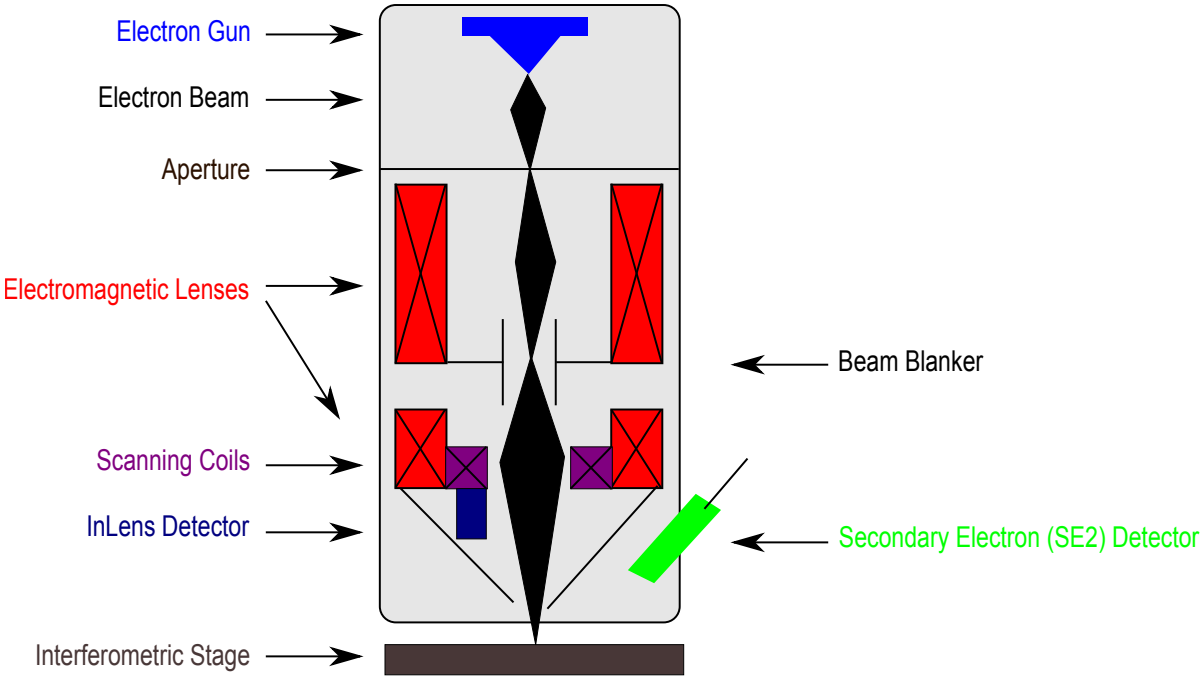

Figure 4.2: Schematic diagram of the essential components of the EBL system. Redrawn from [21].

incident electrons and the sample can cause additional resist exposure.

4.3 Electron-Beam and Resist Interactions

Interactions between the incident electrons, hereafter referred to as primary electrons, and the sample (resist and substrate) act as an intrinsic limit to the exposure resolution of the electron beam. So-called forward scattered electrons originate from collisions between the resist/substrate electrons and the primary electrons. Such small angle scattering events (scattering angle $< 90°$) broadens the beam-profile at the bottom of the resist relative to the top of the resist, creating an undercut profile (see Fig. 4.3). Forward scattering of electrons is more pronounced at low voltages (typically less than 15 keV) and the degree of forward scattering increases with the thickness of the resist [66] Although forward scattering is a limiting factor in terms of the final resolution, it is in some cases highly advantageous, as will be discussed in the following section. In addition to forward scattering, backscattering of electrons need to be considered. Most of the primary electrons have sufficient energy to penetrate through the resist and into the substrate where they undergo large angle scattering (scattering angle $> 90°$). Backscattered electrons re-emerge into the resist at a different site from which they left it, thereby causing additional resist exposure [63]. The distance between the site of incidence and the site where the backscattered electrons re-emerge into the resist, depends upon the energy of the primary beam and the substrate material [67]. At high acceleration voltages (typically higher than 15 keV), backscattering of electrons prevails over forward scattering of electrons [66] and mate-

rials of high atomic number (Z) generate more backscattered electron than materials of low atomic number [64]. Another source that can give rise to subsequent resist exposure is secondary electrons. A secondary electron originates from the ionization of a sample electron due to an inelastic collision between a primary electron and a sample electron [63]. Secondary electrons cause additional beam broadening with respect to forward scattering of electrons and largely account for the minimum resolution that can be achieved [67]. The combined effect of these scattering events is termed proximity effect. The proximity effect makes it hard to predict the highest resolution that can be achieved using an EBL system. Sub-10-nm features has been patterned using PMMA [64].

Quantitatively, the proximity effect is described via a so-called proximity function. The proximity function is typically defined as the sum of two superimposed (overlapped) Gaussian distributions, one of which is attributed to the forward scattering of electrons, while the other describes the backscattering of electrons [67]. It read as follows [68]

$$f(r) = \frac{1}{(1+\eta)\pi}\left[\frac{1}{\alpha^2}\exp(-\frac{r^2}{\alpha^2}) + \frac{\eta}{\beta^2}\exp(-\frac{r^2}{\beta^2})\right] \tag{4.2}$$

in which r is defined as the distance from the point of electron beam incidence, α is the width (full width at half maximum) of the forward scattered electron function, β the width of the backscattered electron function and η the ratio of the energy deposited by backscattered electrons to the energy deposited by forward scattered electrons.

4.3.1 The Resist

PMMA (Poly(methyl methacrylate)) is a widely used very-high resolution positive-tone resist for EBL [63]. It is a synthetic polymer of methyl methacrylate dissolved in a solvent, typically anisole (methoxybenzene) or chlorobenzene, of desired concentration. The molecular weight (i.e. the length of the polymer chain) of PMMA vary in the range 50.000 (50K) to 2.2 million. During exposure, PMMA is broken into smaller, more soluble fragments, a process known as chain-scissoring. The exposed areas are subsequently dissolved in a developer solvent. In general, PMMA becomes less soluble as the length of the polymer chain increase [69].

PMMA is spun onto the substrate at a set rotational speed to form a thin coating. The final thickness of the PMMA resist depends on the viscosity of the diluted PMMA, the adhesiveness to the surface and the rotational speed. The spin-coat is followed by a hotplate or furnace bake to evaporate residual solvent, thereby annealing the PMMA film.

In the present work, a single-layer PMMA scheme and a bi-layer PMMA scheme were employed to produce large arrays of MNPs by the means of EBL. A lift-off process was used to remove the un-exposed PMMA after metal deposition (procedure described in Chapter 5) which in turn removes the metal at these areas. Bi-layer PMMA was employed for the first time at the UiB Nanolab in this thesis work. The lift-off process requires a so-called undercut beam-profile, schematically depicted in Fig. 4.3. The undercut prevents the sidewalls of the

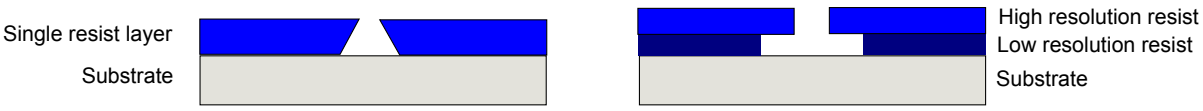

Figure 4.3: Sketch of the desired undercut-profiles obtained using a single layer of resist (left) and a bi-layer resist (right). The general purpose of such profiles is to separate the deposited metal-film on the substrate and the metal-film deposited elsewhere.

resist to be coated during metal deposition, that is, it creates a discontinuous metal layer. Such undercut profiles originate from forward scattering of primary electrons. However, strong forward scattering of electrons is a limiting factor in terms of final resolution [63]. This resolution issue can be addresseed by using a bi-layer resist scheme. In a bi-layer scheme a higher resolution (i.e. lower sensitivity, higher molecular weight) resist is coated on top of a lower resolution (i.e. higher sensitivity, lower molecular weight) resist. The difference in resolution give rise to a wider beam profile at the bottom resist layer, as illustrated in the right panel of Fig. 4.3, which aids the lift-off process. A higher acceleration voltage relative to the single-layer scheme can thus be used and, consequently, a higher resolution can be obtained [63].

4.3.2 The Substrate

In order to study the optical properties of the produced MNP arrays the underlying substrate should be transparent to light in the visible range. From an EBL (and SEM) perspective, a conducting substrate is highly favorable as it prevents surface-charging effects. ITO covered glass slides was initially chosen as the substrate in the work presented by Håvardstun [9], as it is electrically conductive and transparent. However, the MNPs coupled photons to the ITO waveguide (a waveguide hosts propagating photons). This was evident as a suppression of the extinction peak as well as the appearance of several other peaks in the extinction spectra (Extinction = -log(Transmittance) [25]) of gold NP arrays deposited onto ITO. Thus, the optical properties of the MNPs could not be extracted using ITO as the underlying substrate. In order to eliminate such substrate effects, borosilicate glass coverslips (No. 1 coverslips Thermo Scientific) are used as a substrate (dimensions: 22 mm $\times$ 22 mm $\times$ 0.15 mm) throughout the work presented in this thesis. A non-conductive substrate complicates the production procedure, because a charge dissipating layer (e.g. a thin metal layer) is required above or below the resist to avoid charge accumulation in the substrate during exposure [70].

4.4 Electron Beam Evaporator

Electron beam evaporation is a controlled method of depositing a thin film onto a surface. In short, the deposition process comprises locally heating a source material in a crucible inside a vacuum chamber to its evaporation point by the means of a high-energy electron beam. The

vapor of the source material condenses onto the substrate surface as a thin, uniform film.

The electron beam evaporator (Temescal FC 2000) in the UiB Nanostructures facility is depicted in Fig. 4.4. The available source materials to date are gold, aluminium, nickel, titanium and silicon dioxide. Prior to the deposition, source material, angle of deposition and final thickness of the film are defined by the user in the Temescal Control System software. In fabrication of MNPs that requires a lift-off, the metal must be deposited at normal incidence to prevent the sidewalls of the developed resist from being coated. The electron beam is accelerated by a 10 kV power supply (CV-12SLX) and focused onto the crucible of the source material. The system contains two shutters positioned between the crucible and the sample holder. At the point of metal evaporation, a first shutter opens while the other covers the sample holder and the source material condenses onto a quartz crystal. Due to the additional mass, the resonance frequency of the quartz crystal changes. This change in resonance frequency is used as a measure of the deposition rate. When the desired thickness is reached, the second shutter opens and the source material condenses onto the sample surface at a given period of time depending on the pre-determined thickness.

Figure 4.4: The electron beam evaporator in the Nanostructure Laboratory

4.5 Thin-Film Analyzer

The ISO 5 cleanroom hosts a Filmetrics F10-RT thin-film analyzer depicted in Fig. 4.5. It consists of a tungsten halogen light source (spectral range 380 nm - 2000 nm) and two VIS-NIR grating spectrometers (spectral range 380 nm - 1050 nm) connected to a computer. One

spectrometer collects the light directly reflected off a sample while the other detects the light directly transmitted through the sample, as illustrated in Fig. 4.6. Prior to the measurements the materials and their nominal thickness are defined by the user. In order to find the thickness of a thin-film on a flat surface the FilmMeasure software analyzes the reflectance and transmittance spectra of the sample by comparing them to a series of calculated spectra. The match between the measured spectrum and the calculated spectra give rise to a goodness of fit, a number in the range 0 - 1. In this context, 1 is a perfect match corresponding to an accurate measurement.

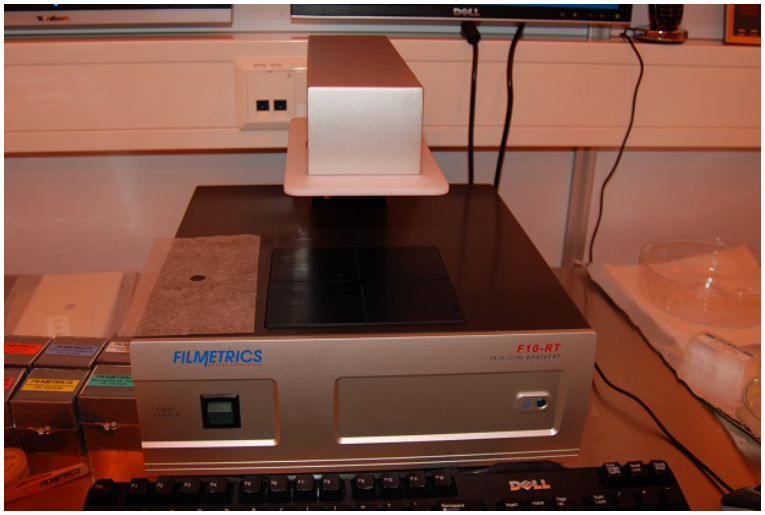

Figure 4.5: The thin-film analyzer in the Nanostructure laboratory

The thin-film analyzer is used to measure the thickness of the PMMA resists. PMMA thickness measurements are presented in Chapter 5.1.2. Additionally, the height of the MNPs are determined using this system. These results are presented in Chapter 6.2.2. Although not employed in this work, the thin-film analyzer can be used to collect the transmittance spectra of the MNPs in order to obtain the extinction of the MNPs.

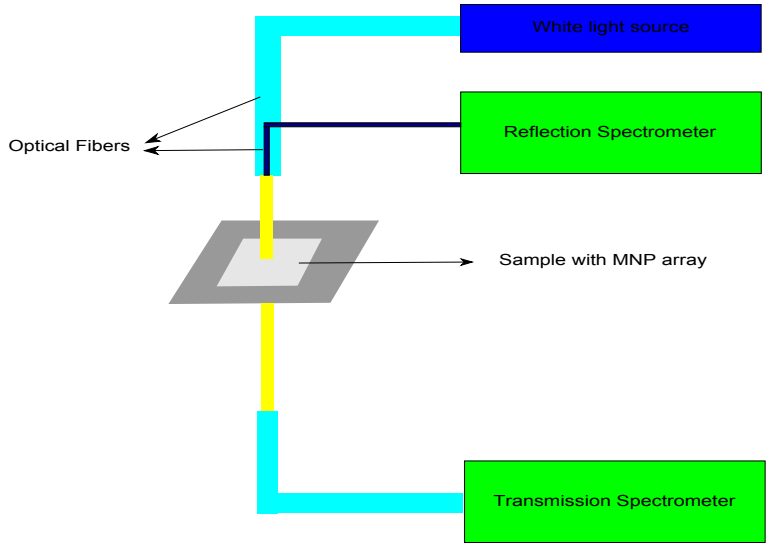

Figure 4.6: Schematics of the set-up used to determine the thickness of the PMMA resist at different spin speed as well as measuring the height of the MNP arrays. Redrawn from [21].

4.6 Integrating Sphere Set-Up

In its simplest form, an integrating sphere is a spherical cavity coated with a ideal diffusely reflecting material (i.e. a so-called Lambertian reflector). The set-up is illustrated in Fig. 4.7 and depicted in Fig. 4.8. Light that enters the sphere is scattered multiple times at the inner wall of the sphere. As a consequence of this scattering, the light within the sphere is uniform, meaning that any spatial, angular or polarization variations at the entrance port are lost. The detector of an integrating sphere collected the total amount of light scattered in all spatial directions [52]. As described in Chapter 2.7 this separation allows for separating the contributions of absorption and scattering to the total extinction of a sample.

The direct light path from the entrance or sample port to the detector port must be blocked, as this light will have a non-uniform distribution. To block these light paths, a so-called baffle is employed in large spheres. Smaller spheres, like the ones used in this work, do not require a baffle, due to small radii of the spheres in combination with the low acceptance angle of the optical fiber [72, 21]. The sample port, entrance port and detector port represent an intrinsic source of error in an integrating sphere. Firstly, the ports themselves are not coated with the highly reflective material so the light is not scattered in all directions. Secondly, a certain amount of information will be lost. As a rule of thumb, the total area of the ports should be less than 5% of the internal surface of the sphere to minimize these errors [72].

As evident from figure 4.6, the thin-film analyzer is capable of recording the transmittance spectrum of a sample, which is needed to obtain the extinction spectrum (extinction = -log(transmittance) [25]). However, only the light directly transmitted/reflected through/off the sample is collected. Absorption of light by the MNPs is expected to contribute to the to-

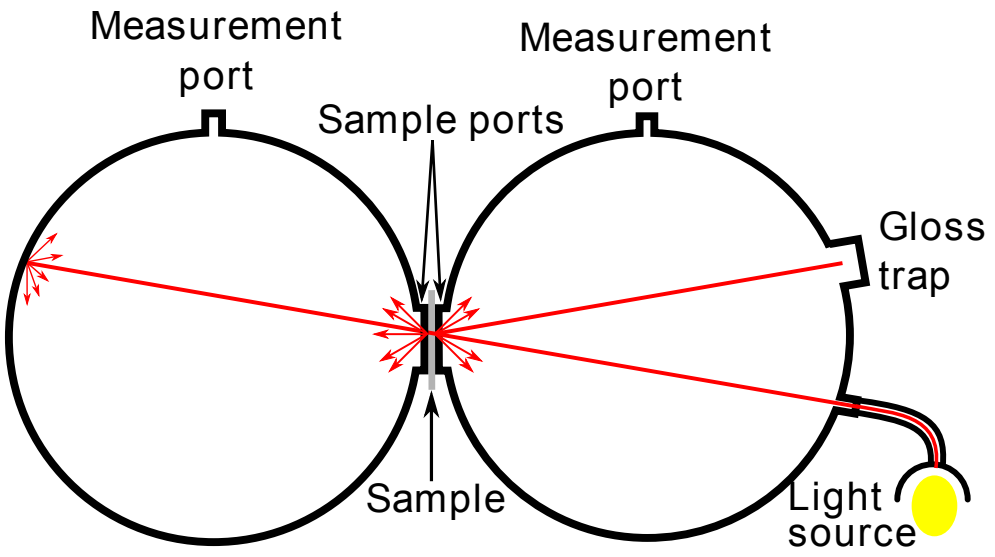

Figure 4.7: Illustration of the integrating sphere set-up. Light that enters the sphere is scattered multiple times at the inner wall of the sphere. The detector of an integrating sphere collected the total amount of light scattered in all spatial directions [52]. This makes it possible to separate the contributions of absorption and scattering to the total light extinction of a sample. Figure taken from [21]

tal extinction. This loss in intensity cannot be detected using the thin-film analyzer due to the small acceptance angle of the fiber. An integrating sphere, on the other hand, collects the light scattered in all spatial directions. The amount of light absorbed by the sample is simply found as a consequence of conservation of energy.

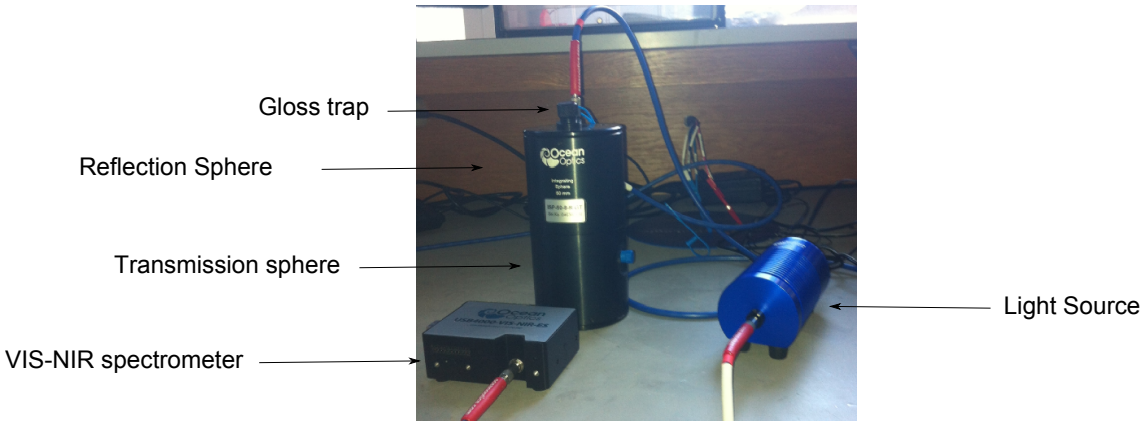

Figure 4.8: The integrating sphere set-up used to obtain the extinction spectra of the produced MNP arrays in this thesis

The integrating sphere set-up used in this thesis is inspired by the work of Langhammer et al. [52]. A tungsten halogen light source (Ocean Optics HL-2000) with a wavelength range of 380 nm -2000 nm is employed. The light is guided to the spheres using an optical fiber (Ocean-Optics P400-2-VIS-NIR) with a diameter of 400 µm and a spectral range of 400 nm - 2100 nm. The spot size (i.e. the diameter of the beam at the sample port) is approximately

3 mm. The set-up consists of two spheres, one of which detects the light transmitted through the sample while the other detects the light reflected off the sample. The transmission sphere (Ocean Optics ISP-50-8-I) and the reflection sphere (Ocean Optics ISP-50-8-R-GT) has an internal diameter of 50 mm and a sample port with a diameter of 8 mm. The reflectance sphere is equipped with a so-called gloss-trap, which is a light-trap inside the sphere used to exclude or include the specular portion of the reflected light. The light entrance port is mounted at an angle of 8° with respect to the surface plane. Consequently, the gloss-trap is positioned at an angle of -8°. The spectral range of the spheres is 200 nm - 2500 nm. The reflectivity of the internal coating is > 98 % in the wavelength range 400 nm - 1500 nm and greater than 95 % in the range 250 nm - 2500 nm. The spectral range of the VIS-NIR spectrometer (Ocean Optics USB400-VIS-NIR ES) is 350 nm -1000 nm. It employs an entrance slit of 25 µm. The maximum number of peaks that the spectrometer can resolve is determined by the spectral resolution, which in this case is approximately 1.5 nm.

Chapter 5

Experimental Procedure

The present chapter describes the experimental procedure for fabricating large periodic arrays of disk-shaped MNPs on a non-conductive substrate by the means of EBL. The procedure for fabricating large arrays (16 mm^2 - 25 mm^2) of MNPs of diameters in the range 45 nm - 150 nm using EBL was established by Håvardstun [9]. The objective of this thesis work has been to improve the fabrication method established by Håvardstun to enable the fabrication of smaller nanoparticles (diameters down to 20 nm) by the means of a bi-layer resist scheme. Furthermore, the topic of this thesis work has been to extend and improve the investigation of the optical properties of the MNPs by using an integrating sphere set-up.

5.1 Electron Beam Lithography Production Steps

This section presents a detailed description of the procedure for fabricating disk-shaped MNPs using EBL. It is important to bear in mind that each step cannot be realized independently; the resulting pattern (resolution) is determined by the accumulative effect of each step.

5.1.1 Solvent Cleaning

Prior to sample-processing all equipment (e.g. beakers, tweezers) was rinsed in three different solvents to remove particle contaminations;

1. Acetone (Emparta ACS, Merk KGaA)
2. Methanol (Emparta ACS, Merk KGaA)
3. 2-Propanol (Emparta ACS, Merk KGaA)

The bare glass substrates were placed in an ultrasonic bath for 10 minutes in acetone, followed by 10 minutes in 2-propanol, as indicated in Figure 5.1. The ultrasonic bath was used to agitate the solvent which in turn removes contaminants on the substrate surface. Subsequently, the substrates were blown dry using pure nitrogen gas and stored in individual sample containers.

Figure 5.1: Image of the ultrasonic bath used for substrate cleaning. Note that the sample holder used in the cleaning process is depicted.

5.1.2 Resist Coating

PMMA (poly(methyl methacrylate)) diluted in anisole was used as a positive-tone resist in this work (described in greater detail in Chapter 4.3.1). Two different resist scheme were employed

- PMMA 950K in anisole (Allresist, Ar-P672.08) at a ratio of 2:3 as a single-layer resist
- PMMA 495K in anisole (Microchem 495K PMMA A8) at a ratio of 2:3 and PMMA 950K (Allresist Ar-P672.02) in anisole (not diluted) as a bi-layer resist scheme

950K and 495K refers to the molecular weight of PMMA i.e. the length of the PMMA chains.

The cleaned glass substrate was placed on a sticky silicon wafer inside the spin coater (Chemat technology KW-4A), as depicted in Fig. 5.2. Subsequently, a small vacuum pump was turned on to prevent the substrate from falling off during the spin-process. PMMA was dispersed onto the glass substrate using a pipette. The spin-coat process is divided into two stages. Firstly, the pre-spin stage disperses the PMMA at low speed and secondly, the high-spin stage homogenizes the PMMA-layer at higher speed. Thereupon, the coated substrate was placed on a hotplate (UniTemp GmbH – Eurotherm 2132) and baked to evaporate residual solvent and harden the PMMA-film.

A thick resist-layer(s) was used in this thesis work as this ease the lift-off process (discussed in Chapter 4.3 and 4.3.1). In the single-layer resist scheme a thickness of approximately 180 nm was used, whereas in the bi-layer resist scheme the total thickness of the resists were approximately 150 nm. To realize the desired thickness of the PMMA-film, the thin-film analyzer was used to measure the thickness of PMMA-films obtained at different spin-speeds. Due to the transparent nature of PMMA and glass, silicon wafers were used as the underlying substrate for the thickness measurements. So-called thickness versus spin-speed curves for

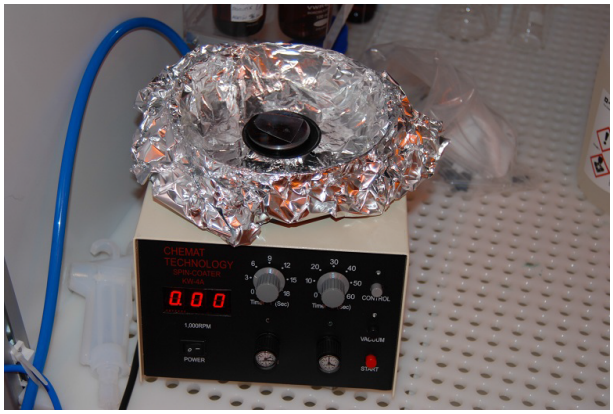

Figure 5.2: The spin coater at the Nanostructure laboratory.

PMMA 950K and PMMA 495K diluted in Anisole at a ratio of 2:3 are presented in Fig. 5.3. The thickness of PMMA 950K (not diluted) was not measured for all spin speeds. The manufacturer Allresist stated that the thickness obtained at 4000 rpm was approximately 70 nm, which was the desired thickness.

In the single layer resist scheme the low speed-stage was set to 500 rpm for 6 seconds and the high spin-stage was set to 4000 rpm for 60 seconds. Directly after the spin-coat process, the substrate was soft-baked on a hotplate at 175°C for 5 minutes. As illustrated in Fig. 5.3, this gave rise to a PMMA thickness of 180 $\pm$ 1 nm. In the bi-layer resist scheme PMMA 495K (PMMA : anisole = 2:3) was used as the bottom resist layer. The low spin-stage was set to 500 rpm for 6 seconds and the high spin-stage was set to 6000 rpm, followed by a soft-bake on the hotplate for 3 minutes at 175°C, giving rise to a PMMA thickness of 82 nm $\pm$ 1 nm. Subsequently, PMMA 950 K (not diluted) was spin-coated on top of the PMMA 495K layer. The low spin stage was set to 500 rpm for 6 seconds and the high spin stage was set to 4000 rpm, followed by a soft-bake for 6 minutes at 175°C to obtain a thickness of 69 $\pm$ 1 nm.

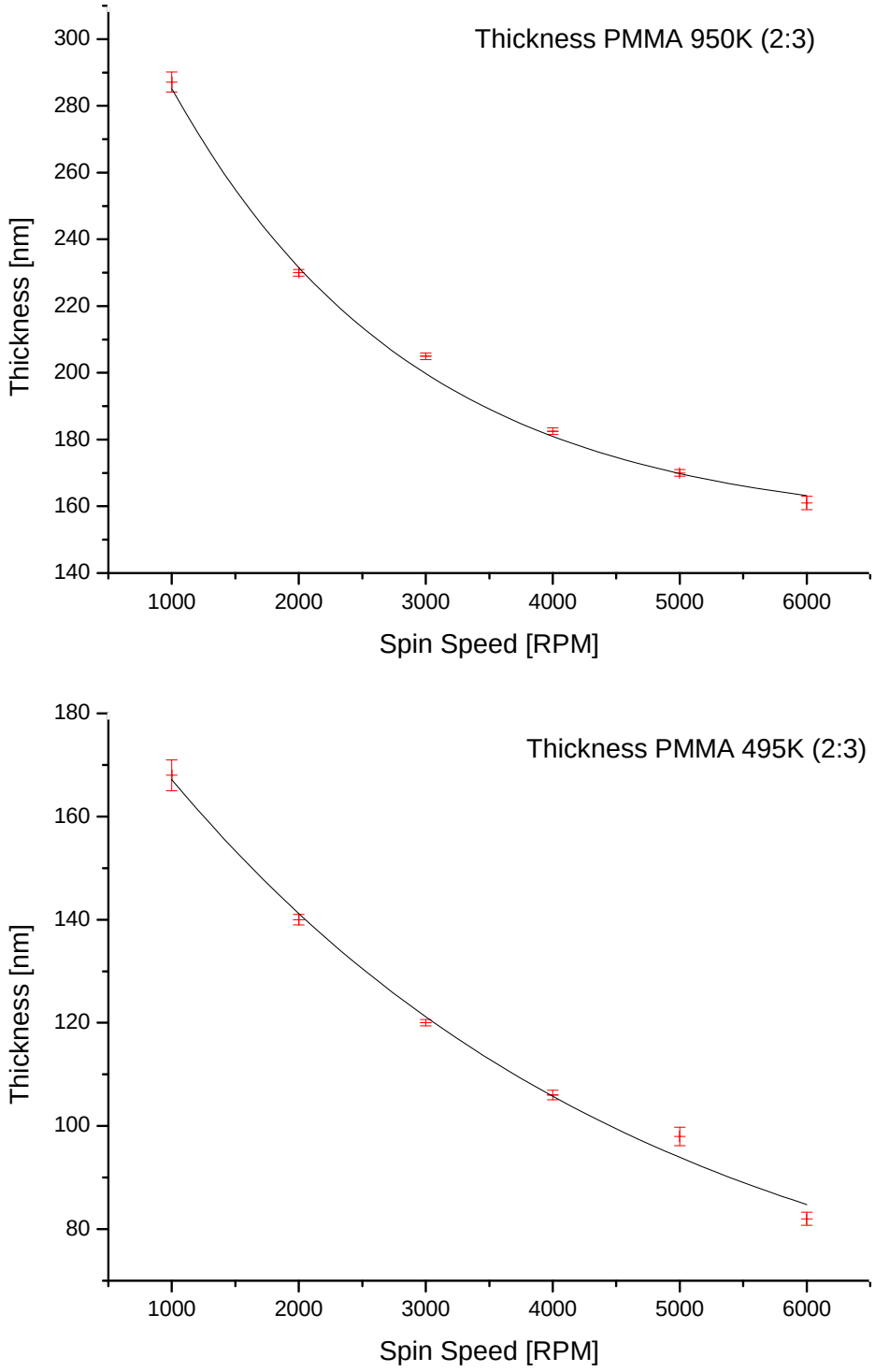

Figure 5.3: Thickness-versus-spin-speed curves. The thickness was measured using the thin-film analyzer and the curves are fitted using 20 datapoints. Y-markers are the standard deviation based on four measurements at different sites on the sample. X-markers is based on a $\pm 1\%$ error of the RPM value given by the spin coater manufacturer (Chemat technology KW-4A). Top panel: Thickness-versus-spin-speed curve for PMMA 950K (PMMA:anisole = 2:3). Bottom panel: Thickness-versus-spin-speed curve for PMMA 495K (PMMA:anisole = 2:3)

5.1.3 Deposition of a conductive layer

The non-conductive nature of the glass substrate required a charge dissipating layer to prevent accumulation of charge in the glass substrate and the associated deflection of the electron beam during exposure. A 4 nm thick layer of Chromium was deposited on top of the resist-coated glass substrate using the electron-beam evaporator. The deposition procedure is described in Section 5.1.8.

5.1.4 Production of Dose Matrices

The optimal exposure doses (described in Chapter 4.2.1) of the large arrays were found by writing multiple write-fields (defined in Chapter 4.2.1) of increasing exposure dose. One such array is called a dose matrix. An illustration to how dose matrices are prepared is given in Fig. 5.4. As the resulting pattern depends upon the type of resist and substrate used for exposure, dose matrices were only written on glass-substrate coated with PMMA (one or two layers) and Chromium (4 nm). The nominal exposure dose was chosen based on the work presented by Håvardstun [9] and the exposure dose varied around this nominal dose.

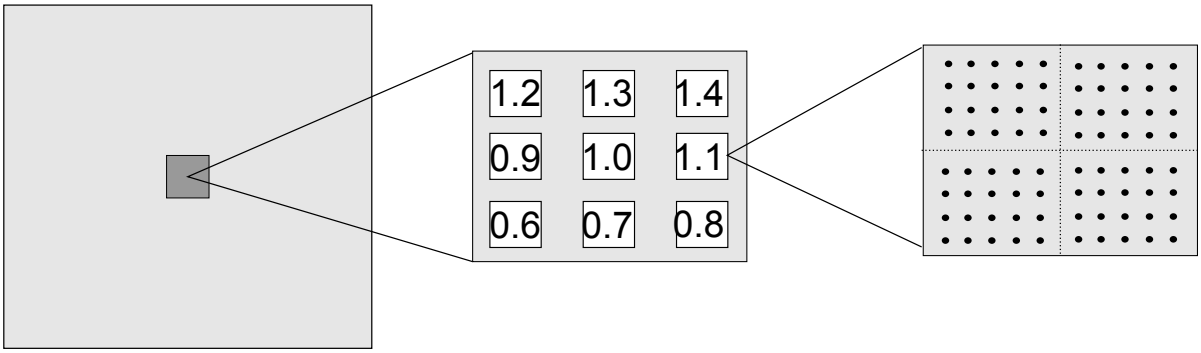

Figure 5.4: Schematics describing the preparation of dose-matrices. Each sqaure is given a number to indicate the dose factor (multiple of the nominal exposure dose). Each square consists of 2 $\times$ 2 100µm $\times$ 100 µm write-fields, so that the stitching between neigboring write-field as well as the size and shape could be evaluated. Redrawn from [9]

CAD-files (100 µm $\times$ 100 µm) containing a 2D periodic array of circles (area exposure) with a given diameter and periodic spacing were prepared. Each circle within each write-field is defined by deflecting the electron beam in a circular motion. Dose matrices were written with an exposure dose ranging from 20 pC/cm^2 to 100 pC/cm^2 using an aperture of 20 µm and an acceleration voltage of 15 keV. Additionally, CAD's (100 µm $\times$ 100 µm) of single coordinate points (dot exposure) with a periodic spacing were prepared. Each dot within each write-field is defined by centering the beam at each point in a given period of time defined by the dwell time (see Equation 4.1). Dot dose matrices were written with an exposure dose ranging from 0.0001 pC to 0.01 pC using an acceleration voltage of 15 keV for the single-layer PMMA and 20 keV for the bi-layered PMMA (a higher acceleration voltage could be applied

in bi-layered PMMA scheme due to the difference in sensitivity of the two layers, see Chapter 4.3.1). The aperture was 10 µm or 20 µm. Although the pattern defined by 2D circles gave more freedom in terms of defining the shape of the MNPs (e.g. by designing an ellipse to pattern a circle), the dot matrices featured the smallest MNPs and were therefore chosen for large array writing.

As discussed in Chapter 6.3, it was found that the proximity effect (desribed in Chapter 4.3) had to be taken into account to achieve the desired particle diameter. This was accomplished by fabrcating dot-dose matrices were the particle size was optimized for a fixed interparticle distance.

5.1.5 Electron Beam Writing Procedure

The sample (i.e. glass substrate coated with PMMA and Chromium) was mounted under two clips in the e-line sample holder. It was found by iteration that mounting the sample under two clips, as opposed to just under one, reduced the tilt in the sample plane caused by the clip. Suspended polystyrene beads were deposited at a corner of the sample surface using a toothpick. The polystyrene beads have a diameter of approximately 100 nm and a well-defined circular shape and were therefore used as a focusing aid. After the loading procedure was executed, the voltage was turned on and the aperture was chosen. In the single-layer resist scheme the acceleration voltage used for large-array writing was 15 keV and the aperture was 20 µm. In the bi-layer resist scheme the acceleration was 20 keV, while the aperture was 20 µm. Thereupon, the stage was moved with respect to the electron beam to the site of the polystyrene beads. At this site, the working distance (i.e. the distance between the final lens and the sample surface), the stigmation and the aperture were aligned at increasing magnifications to find the optimum focus and the clearest SEM image (i.e. minimal aberration). Figure 5.5 depicts polystyrene beads at a high magnification. Subsequently, the working distance was aligned close to the start and end position of the exposure area. The average of these two working distances was used for the exposure. The focus plane of the electron beam is highly sensitive to changes in the sample plane. A minor change in the sample plane increases the spot size of the electron beam which in turn increases the diameter of the exposed point. It was highly important to use the average working distance obtained as described above as opposed to the optimum working distance at the site of the polystyrene beads to minimize polydispersity of the particles diameter.

A write-field alignment was then performed to adjust the electromagnetic deflection system inside the column to the high-precision interferometer stage. A suitable site for write-field alignment is a particle contamination (e.g a dust particle) with separable features at low magnifications (around 5000 X). The write-field alignment was performed first manually at increasing magnifications by dragging vectors from given positions to the chosen site on the particle contamination. Secondly, an automatic write-field alignment was performed at very high mag-

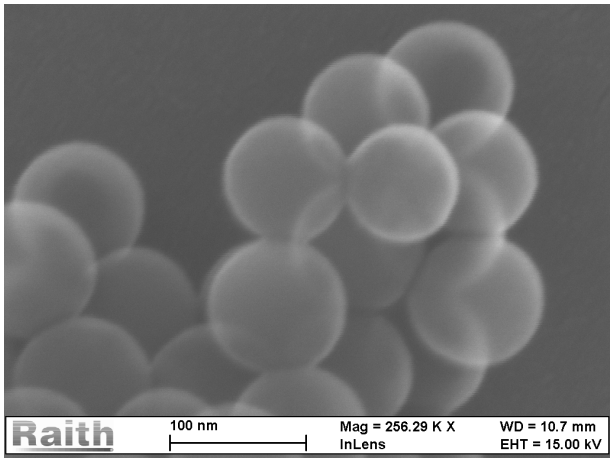

Figure 5.5: SEM image of polystyrene beads situated on the substrate surface. Depositing polystyrene beads at the corner of the substrate surface was used as a focusing aid.

nifications. In the automatic procedure the software interpret the position of the chosen site by the means of image contrast and brightness. The correction vectors assessed from the procedure ensured stage movement of high accuracy. Optimizing the write-field alignment was highly important to minimize stitching-errors in the junction between write-fields.

The sample holder features a Faraday cup (a conductive cup). After completing the write-field alignment, the beam current was measured at the site of the Faraday cup holder. The CAD file comprising the pattern was then imported and given a dose factor (multiple of nominal dose). Finally, the dwell time was calculated (see Equation 4.1) and the exposure initiated. The EBL-writing parameters used for large-array writing are presented in Table 6.2.

5.1.6 Wet Etch of the Conductive Layer

The sample was placed in a chromium etchant (Transene company inc.) bath for a few seconds to remove the chromium-layer. Thereupon, the sample was soaked in deionized water and finally rinsed with 2-propanol.

5.1.7 Chemical development of the resist

The developer solvent used in this thesis work is MIBK:IPA (1:3). MIBK:IPA (AR 600-56, Allresist GmbH) consists of methyl 2-methylpropyl ketone and 2-propanol at the ratio 1:3. To dissolve the exposed areas of the PMMA-resist, the sample was immersed in MIBK:IPA for 2 minutes. Subsequently, the sample was rinsed with 2-propanol in order to stop the developing process and finally blown dry using pure nitrogen gas.

5.1.8 Metal Deposition Procedure

A homogenous thin-film of metal was deposited onto the sample using the electron beam evaporator (Temescal FC-2000). Four different source materials were used in this work

- 4nm Chromium
- 20 nm Gold
- 20 nm Nickel
- 20 nm Aluminum

Chromium was used as a charge dissipating metal layer, while gold, nickel and aluminum were used for fabricated large arrays for optical analysis. Due to its relatively low cost, dose matrices were fabricated using nickel.

The process chamber is maintained at high vacuum. To initiate the loading/unloading procedure the process chamber thus has to be vented to bring it to ambient pressure. Samples, as well as complementary samples for thickness measurements, were mounted onto the sample holder by the means of clips. The type of source material, the angle and rate of deposition as well as the nominal thickness was defined manually in the Temescal software. In this work, the metal was deposited onto the sample at normal incidence with a deposition rate of 0.2 nm/sec. The automatic deposition process was initiated by pumping the chamber down to 1.5×10^{-6} mbar. The high voltage supply was then turned on to power the electron beam. After the deposition, the samples were un-mounted and placed in individual sample containers. Finally, the process chamber was pumped to high vacuum and the high voltage turned off.

5.1.9 Lift-Off Procedure

N-Methyl-2-pyrrolidone (NMP) was used to dissolve the un-exposed PMMA areas on the sample which in turn removes the metal-layer. A glass petri dish was filled with NMP and heated to 80°C on a hotplate (Stuart CB160), while the temperature was monitored using a thermometer. The sample, with the metal layer facing upwards, was placed in the petri dish when the temperature of the NMP had stabilized at 80°C. After a few minutes the metal layer started to crack. 10 minutes into the process, sheets of metal loosened from the sample. After 15 minutes the metal layer was completely removed. Subsequently, the sample was carefully removed from the petri dish, rinsed with 2-propanol and blown dry using pure nitrogen gas.

In the procedure established by Håvardstun [9], the set-point temperature was 70°C and the petri dish was gently shaken if the metal layer did not crack after a few minutes. It is, however, believed that shaking the petri dish increases the number of missing particles in arrays with particle diameters ≤ 45 nm, as depicted in Fig. 5.6. Using a set-point temperature of 70°C without shaking the petri dish was quite time consuming (up to 1.5 hours). Therefore,

the set-point temperature was increased to 80°C and the petri dish and the sample were left untouched during the process. This increase in temperature did not have any negative effect on the resulting pattern.

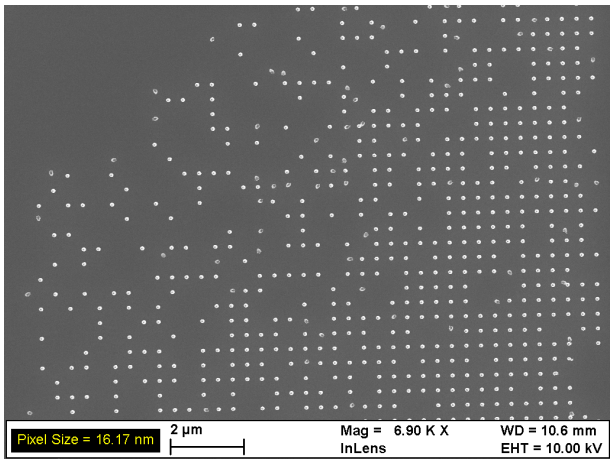

Figure 5.6: SEM image of MNPs subjected to a poor lift-off process. It is believed that the large amount of missing particles stem from shaking the petri dish during lift-off.

5.2 Structural Characterization

5.2.1 SEM

SEM images were used to characterize and measure the shape and size of the MNPs as well as the interparticle distance. Additionally, overview images obtained at lower magnifications were used to evaluate particle arrangement, write-field stitching and the degree of missing particles and impurities.

The accumulation of charge in the non-conductive glass substrate gives rise to a substantial drift of the electron beam. This causes significant image distortions. The finest images of the fabricated arrays were obtained at a voltage of 5 keV and an aperture of 7.5 µm using either the InLens or the SE2 detector. The SEM characterization of the fabricated arrays is presented in Chapter 6.2.1.

In the work presented by Håvardstun [9] it was demonstrated that the accumulation of charge caused a shrinking-effect of the measured dimensions relative to the nominal dimensions. To avoid such charging effects, dose matrices were coated with a 4 nm thick layer of chromium or a 4 nm thick layer of gold-palladium. The latter was sputtered onto the sample by the means of a sputter coater. Dose matrices could thus be images at an acceleration voltage of 10 keV and an aperture of 30 µm.

5.2.2 Height Measurements

The height of the MNPs was evaluated using the thin-film analyzer. In principle, the thickness of the metal-film can be measured prior to lift-off. However, to avoid scratches in the metal film, a complementary glass substrate was coated in the metal-deposition procedure and used for thickness measurements. It is therefore assumed that the thickness of the metal-film resembles the height of the MNPs. The thickness of the metal film was measured at five different sites on the sample.

5.3 Integrating Sphere Measurements

An integrating sphere set-up (described in Chapter 4.6) was used to characterize the optical properties of the fabricated MNP arrays. The set-up can in principle be used to separate the contribution of absorption and scattering to the total extinction. As discussed in Chapter 6.4 and in Appendix A, only the extinction spectra are presented in this thesis work. Nevertheless, this section includes the procedure for obtaining the data needed to separate the absorption and scattering to the total extinction.

All measurements are conducted using the Ocean Optics software SpectraSuite. Prior to use, each sphere was calibrated. The calibration was performed by letting the SpectraSuite software set an integration time based on a reference spectrum. The reference spectrum of the transmission sphere is the light source (i.e. spectrum of an empty sphere), while a diffuse reference standard (WS-1 Reflectance Standard) formed the reference of the reflection sphere. The integration time is defined as the time of period the detector collects light. In general, the longer the integration time, the higher the intensity of the detected signal. Hence, the integration time was adjusted automatically to maximize the signal without saturating the detector. Furthermore, the software was set to average a certain number of scans, to improve the signal-to-noise ratio. Calibration of the spheres must be a part of the standard procedure for use because removing the optical fiber, placing the sample at the sample port etc., allows dust to enter the spheres which changes the throughput of the spheres. The acquisition parameters used in all measurements conducted in this thesis are given in Table 5.1.

Table 5.1: Acquisition parameters used in integrating sphere measurements

Sphere	Integration time [ms]	Scans to average
Reflection Sphere	1350	20
Transmission Sphere	350	100

The gloss trap coated with the same material as the interior of the sphere was used in all the reflectance measurements in order to include the specular component of the reflection.

In order to calculate the extinction spectra and the corresponding scattering and absorption cross-sections of the MNP arrays the following spectra needed to be collected.

- Reference spectrum of the light source and the corresponding dark spectrum in both spheres
- Reflectance spectrum and dark spectrum of the reference standard in the reflection sphere
- Dark Spectrum of sample, glass substrate and empty sphere in both spheres
- Reflectance spectrum of sample and glass substrate
- Transmittance spectrum of sample and glass substrate

Transmittance spectrum and dark spectrum of the light source in the transmission sphere as well as reflection spectrum and dark spectrum of the reference standard in the reflection sphere were needed for post measurement data processing (see Chapter 2.7). The reflectance and transmittance spectra of the glass subtracted from the extinction of the MNP array (MNP and glass substrate) to obtain the extinction of the MNPs.

Chapter 6

Results and Analysis

This chapter presents the experimental results obtained in this work together with theoretical calculations. The chapter is divided into two sections. Firstly, the produced MNPs will be characterized by the means of SEM images and thin-film measurements. In this analysis is size, shape, height, interparticle distance (center-to-center spacing), particle arrangement, degree of missing particles and defects of prime focus. Subsequently, the proximity effect is discussed with respect to the fabrication of dense arrays of MNP of size $\leq$ 45 nm. Secondly, the extinction spectra of the produced MNP arrays obtained using the integrating sphere set-up (see Chapter 4.6) will be presented and analyzed as a function of size and interparticle distance. The measured extinction spectra collected in the present work and in the work of Håvardstun [9] and Greve et al. [73], will then be compared to model extinction spectra calculated using the GranFilm code (see Chapter 3) as well as to experimental spectra obtained by others.

6.1 Samples

A total of five samples were produced as large MNP arrays by the means of EBL (see Chapter 4.2.1) for optical analysis using integrating spheres (described in Chapter 4.6). Standard spectroscopy techniques, such as an integrating sphere, can be employed to study the optical properties because the size of the arrays (9 mm^2 – 16 mm^2) exceeds the light spot size the sphere (approximately 3 mm in diameter). Sample name, nominal diameter, nominal height and interparticle distance are given in Table 6.1. Tabulated values are based on SEM images of small arrays (typically 200 µm $\times$ 200 µm) that were produced to find the optimal acceleration voltage, aperture and exposure dose for large arrays fabrication (described in Chapter 5.1). A charge-dissipating layer (4 nm chromium or 4 nm gold palladium) was deposited on top of these small arrays to avoid accumulation of charge in the glass substrate and the associated degradation of SEM-image quality. The potential increase in diameter originating from this final coating layer is not subtracted from the nominal values. A detailed discussion of the fabrication method can be found in Chapter 5.

Two different PMMA resist schemes, a single-layer resist scheme and a bi-layer resist scheme, were adapted to produce large arrays of MNPs. Establishing an EBL procedure for producing of large arrays by the means of a bi-layer resist scheme was one of the objectives of this work. In a bi-layer resist scheme, a higher resolution PMMA layer is deposited on top of a lower resolution PMMA layer. As discussed in Chapter 4.3 and 4.3.1, the difference in resolution between the two layers ease the lift-off process with respect to the conventional single–layer resist scheme. The sample Au30_90 was produced using a bi-layer PMMA resist scheme, while Au45_150, Ni45_150, Al45_150 and Au45_150 were produced employing a single layer of PMMA resist. The respective interparticle distances are chosen to evaluate how the magnitude of the spacing affects the optical response of the MNPs. A center-to-center spacing equal to or greater than 3 times the particle diameter eliminates near-field coupling between neighboring particles [25]. Hence, Au45_150, Ni45_150, Al45_150 and Au30_90 resemble a periodic ensemble of isolated MNPs, while Au45_100 represent an array of MNPs interacting via their near-field. The optical analysis is presented in Section 6.4.

Table 6.1: Sample name, nominal diameter and nominal diameter of the large MNP arrays produced in this work. The samples are named according to the consituent metal, the nominal diameter and the interparticle distance, respectively.

Sample name	Nominal diameter [nm]	Int.part distance (x,y) [nm]	Height [nm]
Au45_150	45	150,150	20
Ni45_150	45	150,150	20
Al45_150	45	150,150	20
Au45_100	45	100,100	20
Au30_90	30	90,90	20

The EBL writing parameters used in this work are tabulated in Table 6.2. It should be noted that Table 6.2 is not arranged in chronological order with respect to time of production. Additionally, the samples Ni30_60 and Ni20_60 were not written as large arrays. Large array production of the former was initiated several times without success. Each write-field (100 µm $\times$ 100 µm) of Ni30_60 comprises 1666 $\times$ 1666 coordinate points, corresponding to $\approx$ 2.8 million MNPs. The size of this CAD file might have exceeded the file size limit of the e-line software. Multiple write-fields were successfully written, indicating that this is not the case. The production failure is therefore attributed to an e-line software issue that could not be resolved within the timeframe of this work. The company Raith is investigating the problem. Large-scale production of Ni20_60, on the other hand, was never intended. A 100 µm $\times$ 100 µm array of Ni20_60 was produced using an acceleration voltage of 20 keV and an aperture of 10 µm. This reduction in aperture, increases the depth of field and decreases the beam

current, as discussed in Chapter 4.2.1. According to Eq. 4.1, a 3 mm $\times$ 3 mm array of Ni20_60 would take 48 hours to complete, not including the amount of time it takes for the stage to settle between each write-field or the amount of time the electron beam needs to stabilize at a new location. The long write-time of Ni20_60 can, at least to some extent, be reduced through further optimization of the writing-parameters and the writing-parameters are therefore included in the Table.

The low throughput illustrates the main drawback of EBL in terms of fabricating large-area arrays. However, EBL offers high control of particle shape, particle size and particle orientation. As discussed in Chapter 2, the extinction peak (i.e. the LSPR wavelength) is highly sensitive to changes in the above-mentioned parameters. Production of MNPs by the means of EBL thus minimizes inhomogeneous broadening of the extinction peak caused by polydispersity in particle size and shape [51]. This is of prime importance in this thesis work as the long-term objective is to optimize the EnSol solar cell production parameters.

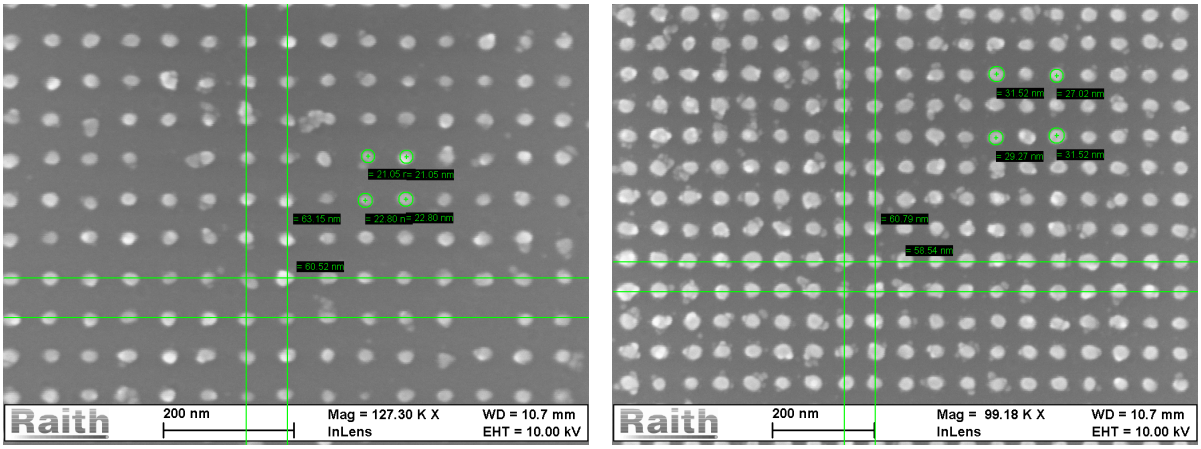

Figure 6.1: Left panel: SEM image of Ni20_60. Right panel: SEM image og Ni30_90. In both cases, a charge-dissipation layer (4 nm of chromium) was deposited on top of the matrices to avoid accumulation of charge in the glass substrate. The matrices were produced using a bi-layer resist scheme. The lift-off process is more feasible in a bi-layer scheme relative to a single layer resist scheme, due to the difference in sensitivity between the two PMMA layers (see Fig. 4.3). The writing parameters are tabulated in Table 6.2.

Table 6.2: EBL writing parameters for MNP arrays. Note that Ni30_60 and Ni20_60 were not written as large array.

	Au45_150	**Ni45_150**	**Al45_150**	**Au45_100**	**Au30_90**	**Ni30_60**	**Ni20_60**
Resist scheme	Single	Single	Single	Single	Bi-layer	Bi-layer	Bi-layer
Int.part distance (x,y) [nm]	150,150	150,150	150,150	100,100	90,90	60,60	60,60
NP diameter [nm]	45	45	45	45	30	30	20
Total area [mm^2]	4×4	4×4	4×4	4×4	3×3		
Acceleration voltage [keV]	15	15	15	15	20	20	20
Aperture [µm]	20	20	20	20	30	20	10
Measured beam current [nA]	0.122	0.115	0.124	0.119	0.287	0.138	0.029
Exposure dose [pC/dot]	6×10^{-3}	6×10^{-3}	6×10^{-3}	3×10^{-3}	3×10^{-3}	3×10^{-3}	2×10^{-3}
Writing hours [hours]	15.5	16	15.5	24	14		

6.2 Structural Characterization

The size, shape, height, interparticle distance, particle arrangement and degree of missing particles of the MNP arrays form the fundamental of the structural characterization within this thesis work. The height of the MNP will be evaluated by the means of the thin-film analyzer (described in Chapter 4.5), while the remaining characteristics are based on SEM images.

6.2.1 SEM Characterization

SEM images were obtained to characterize the shape, size and interparticle distance within each MNP array as well as to evaluate the particle arrangement, degree of missing particles, stitching errors and defects. As borosilicate glass is non-conductive, accumulation of charge in the substrate gives rise to a substantial drift of the electron beam, evident as significant image distortions (see Fig. 6.1 relative to Fig. 6.2 - 6.6). To minimize charge artifacts, SEM images were obtained using an acceleration voltage of 5 keV and an aperture of 7.5 µm. Nevertheless, the drift of the electron beam still caused distortions in the images, even at high raster scan speeds. None of the samples were subsequently coated with a conductive layer as this would distort the optical analysis. SEM images of each sample, one overview image and one close-up, are presented in Fig. 6.2 - Fig. 6.6.

Particle diameter and interparticle distance were measured at five different sites on the sample; at each of the four corners and in the center of the array. Five interparticle distances and five diameters were measured at each site. This selection is assumed to be representative for the whole array. Table 6.3 presents the average particle diameters in x - and y - direction and the corresponding interparticle distances based on the SEM images. Standard deviation is used as error bars. As is evident from Table 6.3, the standard deviation of the particle diameter is typically small, indicating that the variations in particle size within the array are small. The exception is Au30_90 where the standard deviation of the particle diameter is high with respect to the other arrays. Although not evident from Table 6.3, the particle diameter of Au30_90 increased along the diagonal of the array. Each particle within the array, as with the other arrays, is defined as coordinate points in the CAD file. These coordinate points are exposed as single pixels, so the resulting particle diameter is determined by the exposure time at each point (and electron-scattering events in the resist/substrate). Hence, small variations in the sample plane alter the focus plane of the electron beam which in turn increases the spot size of the electron beam. The increasing particle diameter and consequently the large standard deviation are therefore attributed to a tilt in the sample plane. That being said, standard deviation is not the proper statistics to use for quantifying such systematic drift. It has, however, been applied in order to quickly compare the measurements.

Table 6.3: MNP diameter and interparticle distance based on SEM images. The tabulated values are the average diameters and interparticle distances based on five measurements at five different sites on each array. Five particle diameters and five interparticle distances were measured at each site. Standard deviation is used as error bars.

Sample	**NP diameter (y) [nm]**	**NP diameter (x) [nm]**
Au45_150	42 ± 3	40 ± 4
Ni45_150	43 ± 3	40 ± 4
Al45_150	43 ± 3	41 ± 3
Au45_100	43 ± 3	42 ± 4
Au30_90	30 ± 8	31 ± 7
	Int.part distance (y) [nm]	**Int.part distance (x) [nm]**
Au45_150	140 ± 2	132 ± 4
Ni45_150	141 ± 3	135 ± 4
Al45_150	141 ± 3	134 ± 4
Au45_100	97 ± 4	94 ± 2
Au30_90	89 ± 1	87 ± 2

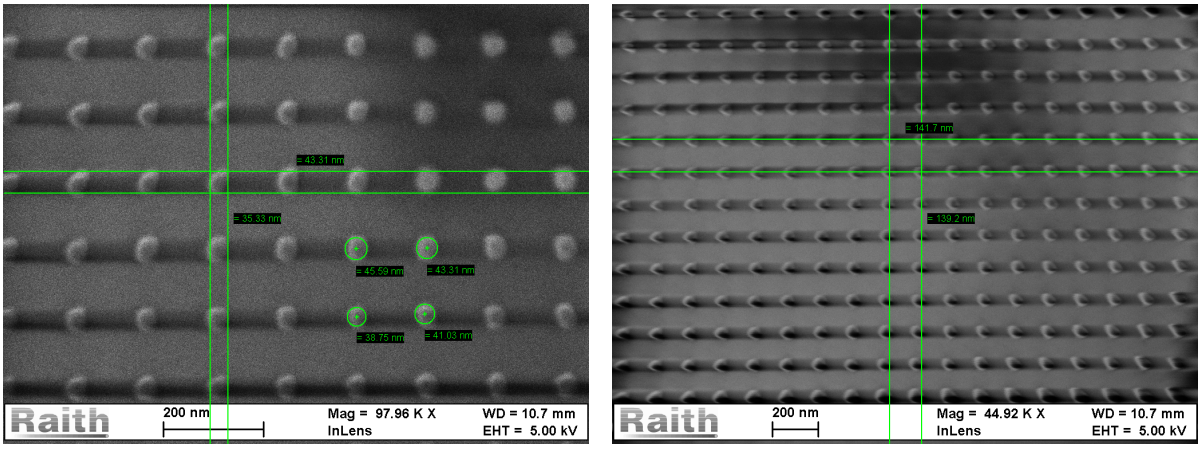

Figure 6.2: SEM images of Au45_150. The image distortion and shadow effect evident in the images are caused by accumulation of charge in the non-conductive glass substrate. Left panel: A close-up image used to determine the size and interparticle distance within the array. The average particle diameter along the x-axis and y-axis was found to be 40 nm $\pm$ 4 nm and 42 nm $\pm$ 3 nm, respectively. The corresponding interparticle distances were measured to be 132 nm $\pm$ 4 nm and 140 nm $\pm$ 2 nm. Right panel: Overview image of the array used to evaluate particle arrangement, degree of missing particles and defects.

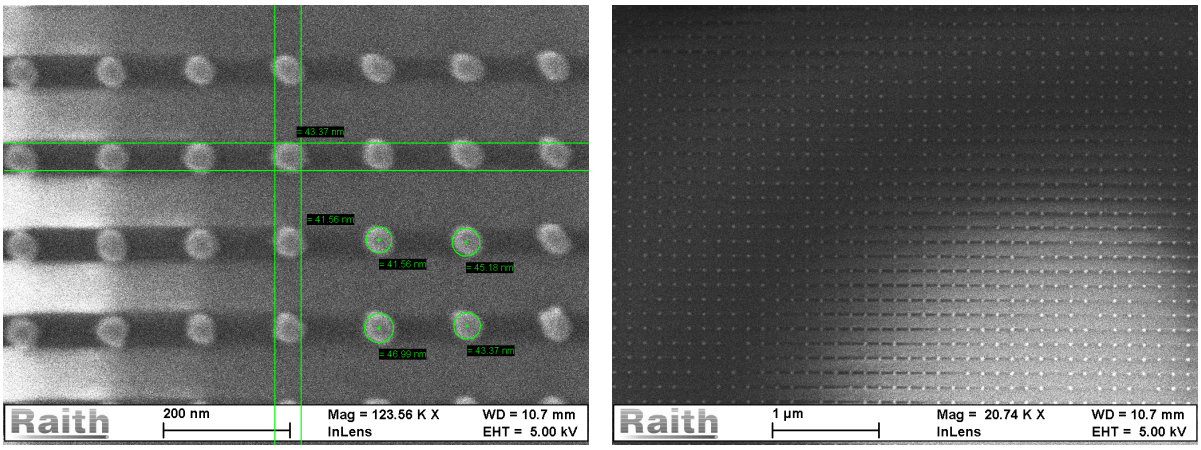

Figure 6.3: SEM images of Ni45_150. Note the effect of accumulation of charge in the glass substrate. Left panel: A close-up image used to evaluate size and interparticle distance within the array. The average particle diameter along the x-axis and y-axis were found to be 40 $\pm$ 4 and 43 $\pm$ 3 nm, respectively. The corresponding interparticle distances were 135 $\pm$ 4 nm and 141 $\pm$ 3 nm. Right panel: Overview image of the array.

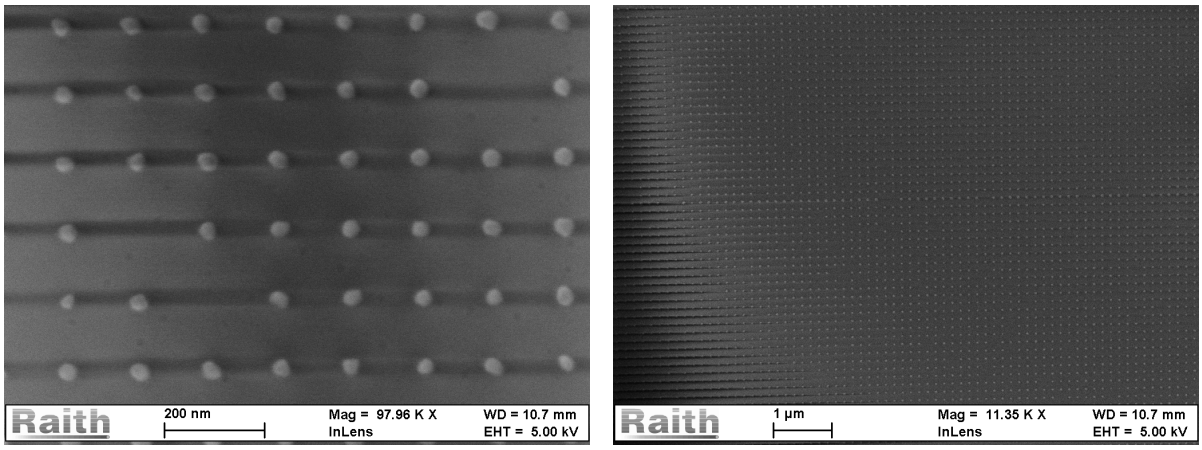

Figure 6.4: SEM images of Al45_150. Left panel: A close-up image used to evaluate particle size and interparticle distance within the array. Note the missing particle sites. As will be discussed below, this was not a frequent feature within the array. The average particle diameter along the y-axis and x-axis was measured to be 43 $\pm$ 3 nm and 41 $\pm$ 3 nm, respectively. The interparticle distance along the y-axis was found to be 141 $\pm$ 3 nm, while the interparticle distance along the x-axis was 134 $\pm$ 4 nm,. Right panel: Overview image of the array.

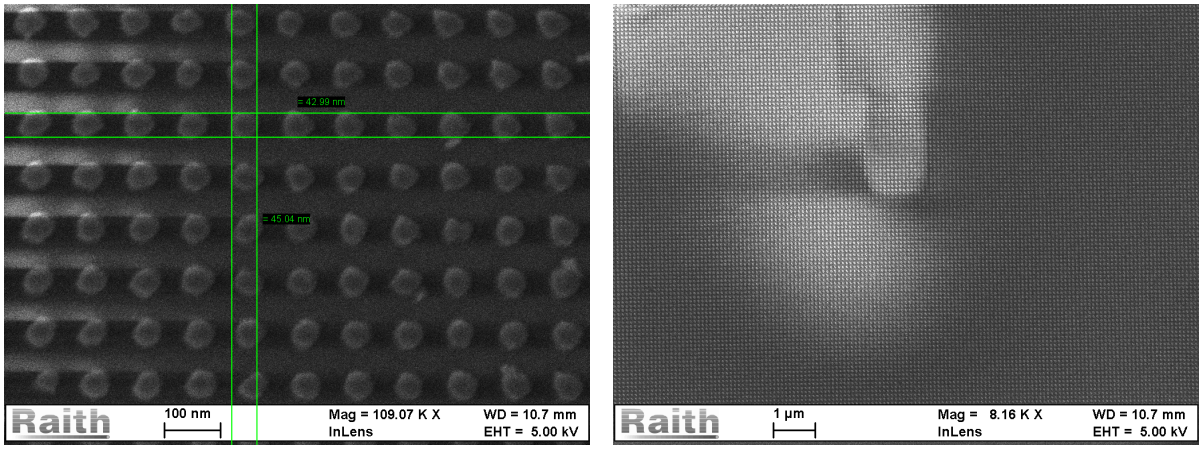

Figure 6.5: SEM images of Au45_100. Left panel: SEM image used to determine the size and interparticle distance within the array. The average particle diameter and interparticle distance along the x-axis and y-axis was found to be 42 $\pm$ 4 nm, 43 $\pm$ 3 nm and 94 $\pm$ 2 nm and 97 $\pm$ 4 nm, respectively. Right panel: Overview image of the array.

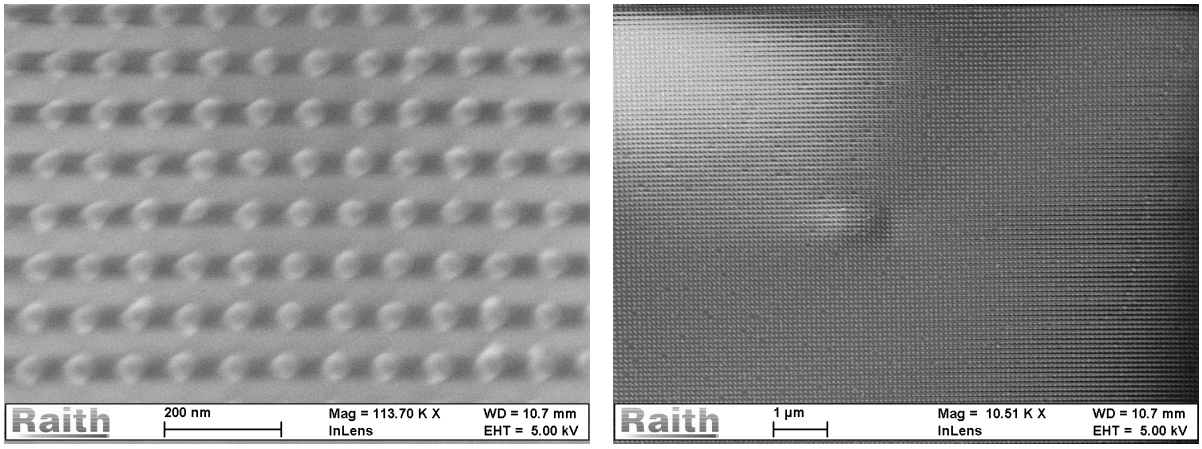

Figure 6.6: SEM images of Au30_90. Left panel: SEM image used to determine the size and interparticle distance within the array. The average particle diameter along the x-axis and y-axis were found to be 30 ± 8 nm and 31 ± 7 nm. The corresponding interparticle distances were 89 ± 1 nm and 87 ± 2 nm. Right panel: Overview image of the array. Note that the degree of missing particles is larger relative to the SEM images above.

Charging Effect

As evident from Table 6.3 the measured particle dimensions differ significantly from the nominal dimensions tabulated in Table 6.1. In the work presented by Håvardstun [9], it was found that the accumulation of charge in the glass substrate caused the interparticle distance as well as the diameter of the MNPs to shrink relative to the nominal dimensions. Håvardstun quantified the effect by sputter coating one of the produced samples with a 3 nm thick layer of gold palladium (AuPd). The dimensions of the coated array matched the nominal size and interparticle distance. The effect was assumed to be independent of particle size and interparticle distance and a correction factor, defined as the ratio of coated sample dimensions to uncoated sample dimensions, was applied to all arrays to obtain charge-corrected sample dimensions. Undoubtedly, the shrinking effect is also observed in the arrays produced in the present work. However, the arrays will be used for optical analysis beyond the scope of this thesis work and were therefore not subsequently coated with a conductive layer as this would distort the optical analysis. The nominal dimensions are therefore based on small MNP arrays (200 µm $\times$ 200 µm), so the polydispersity in size within each array is in practice negligible. Table 6.4 presents the average particle diameter and interparticle distance measured on the small arrays. Standard deviation is used as error bars. The tabulated values are based on five measurements of particle diameter and interparticle distance at five different sites on the matrix; near each corner and at the middle of the matrix. As can be seen from Table 6.3 and Table 6.4 the number of MNPs situated on the glass-substrate seem to influence the magnitude of the shrinking of the interparticle distance, which approaches unity as the particle density (number of particles/array) increases. Said in other words, on contrary to correction factor obtained in the work of Håvardstun [9]

which was described as a constant, the correction factor of the present work seems to change with the interparticle distance in a systematic fashion. Additionally, in Au45_150, Al45_150 and Ni45_150, the horizontal interparticle distances shrunk significantly more than the corresponding vertical distances. This horizontal shrinking effect originates most likely from the direction the beam scans to obtain an image. The electron beam scans from the left top to the right bottom along the horizontal axis across an area, which causes the horizontal direction of the image to be more influenced by the charge-shrinking effect than the vertical direction. This horizontal shrinking is also, although to a less extent, observed in the particle diameter. To gain further insight of the charging effect the samples need to be coated with a conductive material.

Table 6.4: Particle diameter and interparticle distance of the dose matrices with parameters used for large-array writing (see Table 6.2). The tabulated values are based the average of five measurements at five different sites on the matrices. Standard deviation is used as error bars.

Sample	**Particle diameter (x,y) [nm]**	**Interparticle distance (x,y) [nm]**
Au45_150	45 ± 1	150 ± 1
Ni45_150	45 ± 1.5	150 ± 1.5
Al45_150	45 ± 2	149 ± 1
Au45_100	45 ± 1.5	100 ± 1
Au30_90	30 ± 2	90 ± 1

To summarize, the particle diameter and the interparticle distance within each produced array were determined by the means of SEM images. Accumulation of charge in the glass substrate and the associated degradation of SEM-image quality complicated the characterization in addition to shrinking the particle dimensions relative to the nominal dimensions. SEM images of smaller arrays indicate that the shrinking effect is systematic, in such a way that the interparticle distances approaches the nominal spacing as the particle density increases.

Particle Arrangement and Defects

The sizes of the arrays are so large that defects such as missing particles and stitching errors are in practice inevitable. Nevertheless, with respect to the large size of the arrays the presence of defects was found to be insignificant with respect to the optical analysis. It should however be noted that accumulation of charge in the glass substrate complicated this analysis significantly.

The left panel of Fig. 6.7 depicts a metal layer which has not been successfully removed from Au45_100 (such large layers were not found in any of the other arrays), while the right

panel feature missing particles in Al45_150. The resulting pattern produced using EBL is determined by the accumulative effect of each production step (described in Chapter 5). Defects can in principle originate from any step of the process. The fabrication was performed under as identical conditions as possible. Nevertheless, small variations spin-coat speed or baking time/temperature can change the thickness of the resist. Temperature variations in the ISO 7 cleanroom cabinet can affect the writing procedure. The time of period the sample was immersed in the developer solvent, the temperature and purity of the solvent can alter the solubility of the exposed PMMA. Finally, the temperature of the NMP-solvent can influence the lift-process process.

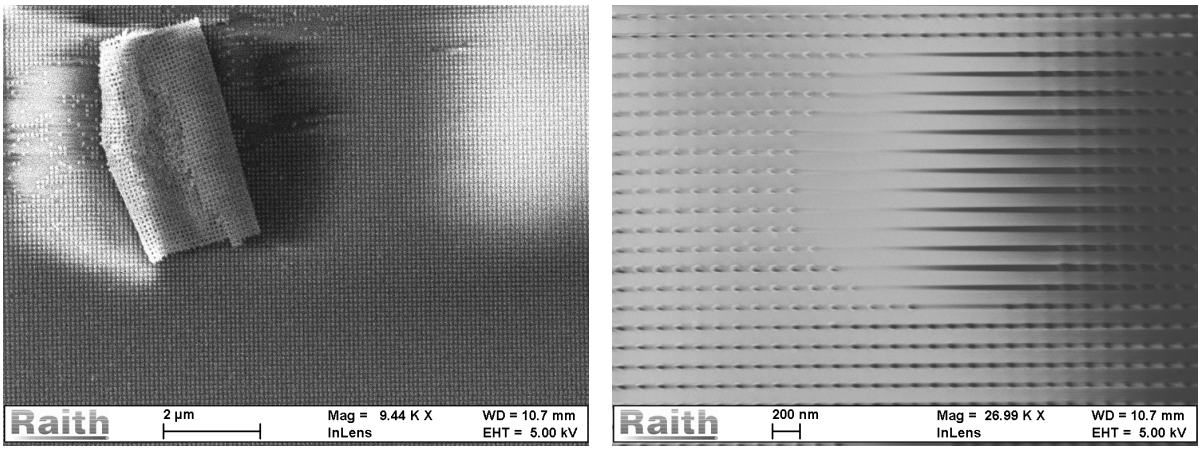

Figure 6.7: Left panel: Metal layer left-over in the Au45_100 array. Such large metal left-overs was not observed in any of the other arrays. Right panel: Missing particles in Au45_150.

The degree of missing particles in Au45_150, Al45_150, Ni45_150 and Au45_100 were found to be minor. Based on SEM- overview images, the degree of missing particles is found to less than 1 in a 1000, except at the edges of the arrays. Missing particles at the edges can be attributed to the lift-off process or scratches in the metal-film. Furthermore, the electron dose is at its minimum at these sites (discussed in greater detail in Section 6.3) so the edges are more likely to be underexposed than the rest of the array. Au30_90 featured many missing particle sites relative to the other arrays. These sites were, as with the other arrays, most pronounced at the edges of the array. However, throughout the array missing particle sites were present. It is not understood why the degree of missing particles was so large. Au30_90 was produced using a bi-layer resist scheme. In all the small arrays that were produced, a bi-layer resist scheme was found to reduce the degree of missing particle sites.

Stitching error originates from inaccurate movement of the stage at the junction between write-fields (100 µm $\times$ 100 µm). Every array featured stitching errors and the observed interparticle distances in between write-fields were larger than the interparticle distance within the write-field. That being said, the magnitude of the stitching error does not continuously increase throughout the array. It typically exceeded the nominal interparticle distance by 20 nm to 100 nm. The CAD-file was designed to minimize the presence of write-fields (i.e. particles)

that overlap by increasing the distance between neighboring write-fields, to avoid strong near-field coupling between adjacent particles at these sites. Said in other words, the CAD-file of e.g. Au45_150 was 99.75 µm × 99.75 µm rather than 100 µm × 100 µm. It is important to note that increased interparticle distance at the junction between write-field also can distort the optical analysis. In the produced samples that resembles isolated MNPs (i.e. Au45_150, Ni45_150 and Al45_150, Au30_90), an increased interparticle distance can give rise to far-field coupling via diffraction [74]. In Au45_100, where near-field coupling is expected, neighboring particles will not interact via their near-field when the interparticle distance exceeds a certain distance [74]. Au45_100 is the densest array produced within this work. The percentage of particles subjected to stitching error in Au45_100 is approximately 0.4 %. In the estimate is the fact that the outermost write-field only has three neighboring write-field ignored. In the optical analysis stitching errors will be neglected.

6.2.2 Height Measurements

The thin-film analyzer (described in Chapter 4.5) was employed to determine the height of the MNPs. The height measurements are not based on the samples themselves, but on complementary glass substrates that were coated in the metal deposition process (see Chapter 4.4). During the deposition process, the thickness of the metal-film is continuously measured by the means of a quartz crystal. Due to deposition of metal during the shutdown procedure (typically 1 nm – 2 nm) the final thickness assessed by the quartz crystal exceeded the magnitude of the nominal thickness (20 nm).

In principle, the thickness of the sample-film could have been measured prior to the lift-off process. However, this could scratch the metal-film and was therefore not done. It is therefore assumed that the thickness of the complementary glass substrate resembles the height of the MNPs. Each metal film was measured at five different sites, near the four corners and in the middle, with a goodness of fit > 0.95. Table 6.5 presents the average height of the MNPs. Standard deviation is used as error bars. The measured thickness exceeds the nominal thickness of the films (20 nm) of approximately 5 nm – 6 nm. Nevertheless, the film is highly uniform, which is one of the main attributes of the electron beam evaporator. To evaluate the height of the MNPs in further detail atomic force microscopy (AFM) could have been employed. However, this was not possible within the framework of this thesis, since the UiB nanolab does not have an AFM with proper height calibration so the sample would have had to be taken elsewhere.

Table 6.5: Height of the MNP array determined using the thin-film analyzer. The tabulated values are based on five measurement at different sites on the sample. Standard deviation is used as error bars.

Sample	Height [nm]
Au45_150	26 ± 1
Ni45_150	23 ± 2
Al45_150	25 ± 1
Au45_100	26 ± 1
Au30_90	26 ± 1

6.3 The Proximity Effect

As described in Chapter 4.3, the so-called proximity effect works as an intrinsic limit to the final resolution in EBL patterning. It was found that the proximity effect needed to be taken into account when finding the optimum dose for large array writing. As depicted in Fig. 6.8, the diameter of the MNP increases as the interparticle distance decreases. The respective dose was 5.25×10^{-3} pC, the acceleration voltage was 15 keV and the aperture 20 µm. Note that the particle diameter increases significantly more when the interparticle distance decreases from 150 nm to 100 nm (increase of $\approx$ 18 nm) versus 400 nm to 200 nm (increase of $\approx$ 4 nm).

The proximity effect can be modeled as two superimposed Gaussian functions, one of which describes backscattered electrons while the other is attributed to the forward scattering of electrons [68]. Each function is characterized by its width (FWHM), that is, the magnitude of the length that the forward scattered and backscattered electrons travel. The width depends upon the thickness of the resist, the substrate material and the energy of the incident electron beam. Forward scattering of electrons only broadens the beam profile, so the forward scattering function feature a narrow distribution. On contrary, backscattered electrons can give rise to subsequent resist exposure at another site from which they left the resist. Hence, the backscattered function features a wide distribution. This additional resist exposure will further be enhanced if several functions are placed in near vicinity (i.e. when patterning multiple features in near vicinity) as the backscattered functions overlap [75]. The increase in diameter evident in Fig. 6.8 is therefore attributed to increasing overlap among neighboring backscattered proximity functions.

The realization that the proximity effect needed to be taken into account in order to obtain desired particle dimensions was one of the reasons for adapting a bi-layer resist scheme. In the

bi-layer resist scheme the lower resist layer function as a substrate which reduces the degree of backscattered electrons. That being said, a bi-layer resist scheme will by no means eliminate the proximity effect.

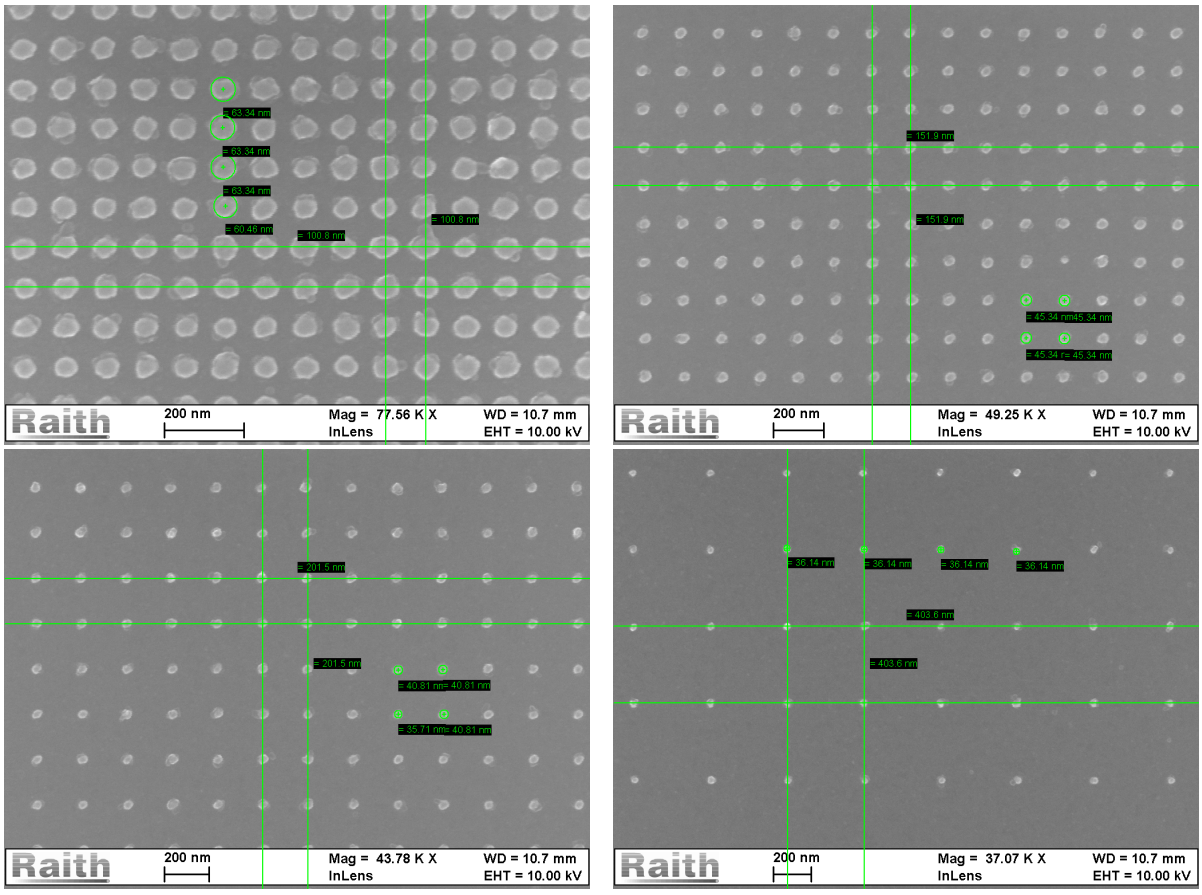

Figure 6.8: SEM images illustrating the proximity effect. The exposure dose used to obtain the matrices are in all cases 5.25 $\times 10^{-3}$ pC. Note that the particle dimensions decreases less and less as the interparticle distance increases.

6.4 Optical Analysis

The present section encloses the optical analysis of this work. The optical properties of the MNP will be evaluated as a function of size, constituent metal and interparticle (center-to-center) distance. The section is divided into two parts; firstly, the extinction spectra obtained from the integrating sphere measurements will be presented and analyzed and secondly, model extinction spectra calculated using the GranFilm code will be analyzed with respect to corresponding experimental spectra obtained in the present work and in the work of Håvardstun [9] and Greve et al. [73]. The objective is to determine the extinction maxima i.e. the spectral position of the LSPR and compare the findings to results obtained by others.

6.4.1 Integrating Sphere Measurements

The integrating sphere set-up employed in the present work consists of a tungsten halogen light source (white light) with a wavelength range of 300 nm – 2000 nm. The spot size of the light source is approximately 3 mm in diameter so no lenses have been used to focus the light beam. Originally, the integrating sphere set-up was employed in order to separate the relative contribution of scattering and absorption to the total extinction of the MNP. However, the measured reflectance of the glass substrate is lower than it should be. This is likely attributed to light-loss mechanisms inside the sphere, but it is yet not truly understood. Preliminary results from the reflectance measurements are presented in Appendix A. This section presents the extinction spectra of the MNP arrays. The objective is to determine the wavelength in which the resonance condition is satisfied (discussed in Chapter 2) i.e. to determine the extinction maxima. The samples are characterized by their nominal diameter and interparticle distance (see Table 6.4), due to the charging effect described in Section 6.2.1.

All raw data have been baseline corrected in post measurement data processing as described in Chapter 2.7. Extinction is plotted as a function of incident wavelength in the spectral range 400 - 1000 nm, due to limitations in the performance of the light source outside this range. To improve the signal-to-noise ratio the SpectraSuite software was set to average 100 scans (see Chapter 5.3), with an integration time of 300 ms per scan. The measured extinction maxima is tabulated Table 6.6. The standard deviation was first estimated by fitting the plot to a Gaussian distribution. However, the resulting standard deviation of the mean was very small (less than 1 nm in all fitted distributions). Arguably, the resolution of the spectrometer is 1.5 nm so the standard deviation of mean should be small. Nevertheless, to be on the safe side, the standard deviation of extinction maximum is estimated as the difference between the peak position itself and the edge of the shoulder of the peak.

As is evident from Table 6.6 the extinction spectra of Al45_150 and Ni45_150 are not obtained. Although a UV-VIS spectrometer (wavelength range 200 nm – 1100 nm) as well as a deuterium tungsten halogen light source (wavelength range 200 nm - 2000 nm) was at hand, the optical fiber suffered from transmission loss which resulted in minimal or no signal in the wavelength range (250 nm – 400 nm) where the LSPR was expected to be. It was not possible to obtain a suitable optical fiber within the time frame for the thesis.

Table 6.6: Measured extinction maxima of the samples Au45_150, Au45_100 and Au30_90. Standard deviation is estimated as the difference between the peak position and the edge of the shoulder of the peak.

Sample	**Extinction maximum [nm]**
Au45_150	550 ± 2
Au45_100	568 ± 3
Au30_90	585 ± 4

Extinction Spectrum of Glass Substrates

The extinction spectrum of a bare glass substrate is given in Fig. 6.9. The reflectance and transmittance spectra of a total of five glass coverslips were collected. A reflectance standard (WS-1 Diffuse Reflectance Standard) was used as reference in the reflection sphere, while an empty sphere was used as reference in the transmission sphere. The corresponding dark spectra were used as baseline. The extinction spectrum presented in Fig. 6.9 is the average spectrum based on the five trasmittance spectra. Standard deviation, plotted at every 50 data point is used as error bars. The manufacturer Thermo Scientific states that the transmittance of the glass coverslips is approximately 94 % across the wavelength range 400 nm – 800 nm, which corresponds to an extinction of ≈ 0.03 [76].

Although not evident from Fig. 6.9, it should be noted that the borosilicate glass coverslips absorbs light in the UV-regime (below 340 nm) [76]. In all of the remaining spectra presented in this thesis, the extinction of a naked glass substrate has been subtracted from the extinction of the MNP to eliminate substrate effects, that is, to extract the MNP extinction spectra.

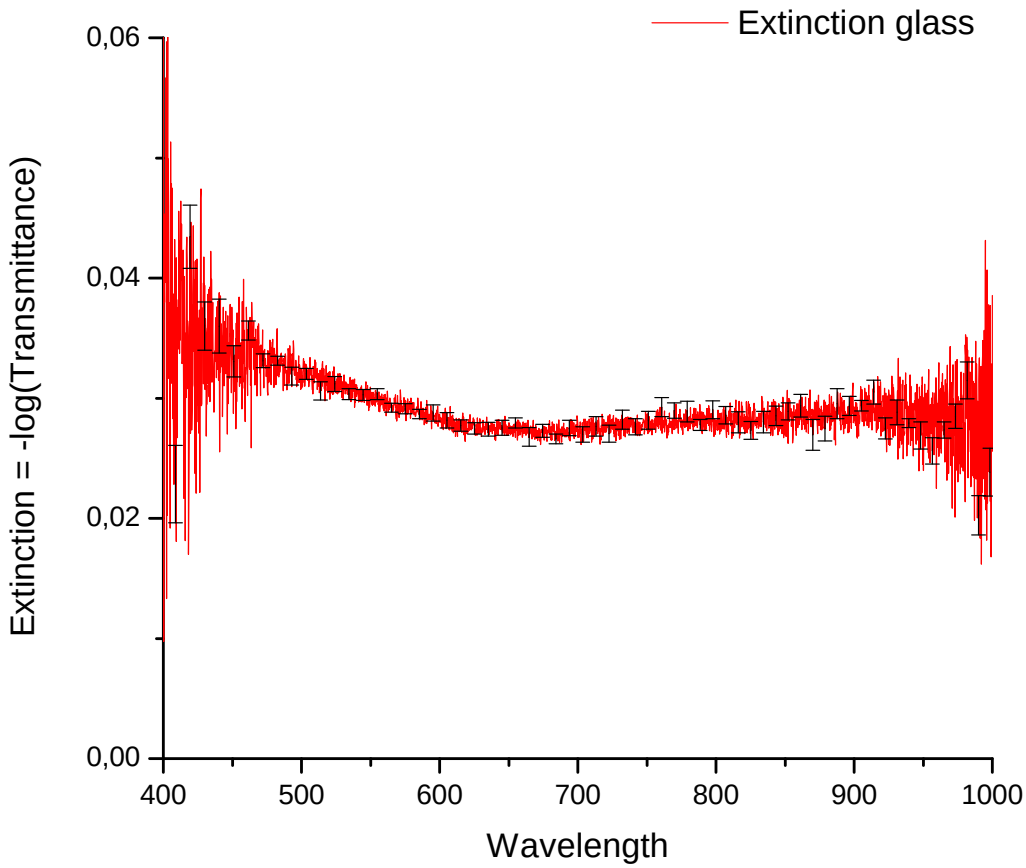

Figure 6.9: Average extinction spectrum based on five bare glass substrates. Standard deviation per 50 point is used as error bars.

Effect of near-field coupling on the LSPR wavelength

The extinction spectra of Au45_150 and Au45_100 are depicted in Fig. 6.10. The particles of the former array has a nominal diameter of 45 nm $\pm$ 1 nm and an interparticle distance of 150 nm $\pm$ 1 nm, while the particles of the latter array has a nominal diameter of 45 nm $\pm$ 1.5 nm and an interparticle distance of 100 nm $\pm$ 1 nm. The increased extinction intensity of Au45_100 with respect to Au45_150 originates from the increased surface coverage. The increase in intensity at the left tail of the spectra are attributed to interband transitions in gold [52], giving rise to the characteristic asymmetric shape of the peak.

The array Au45_150 represents isolated MNPs. However, polydispersity in particle diameter causes inhomogeneous broadening of the extinction peak with respect to a single MNP [52]. The SEM images revealed that the particles took a slightly elliptic shape (aspect ratio 1.1 $\pm$ 0.1). The wavelength of LSPR excitation is known to be highly dependent upon the shape of the MNP, so a slightly elliptic particle shape can influence the resonance condition. Guler and Turan [77] studied gold NP produced by EBL that exhibit an elliptic form, although with a larger aspect ratio (1.37) than the one observed in this work. A broad linewidth was

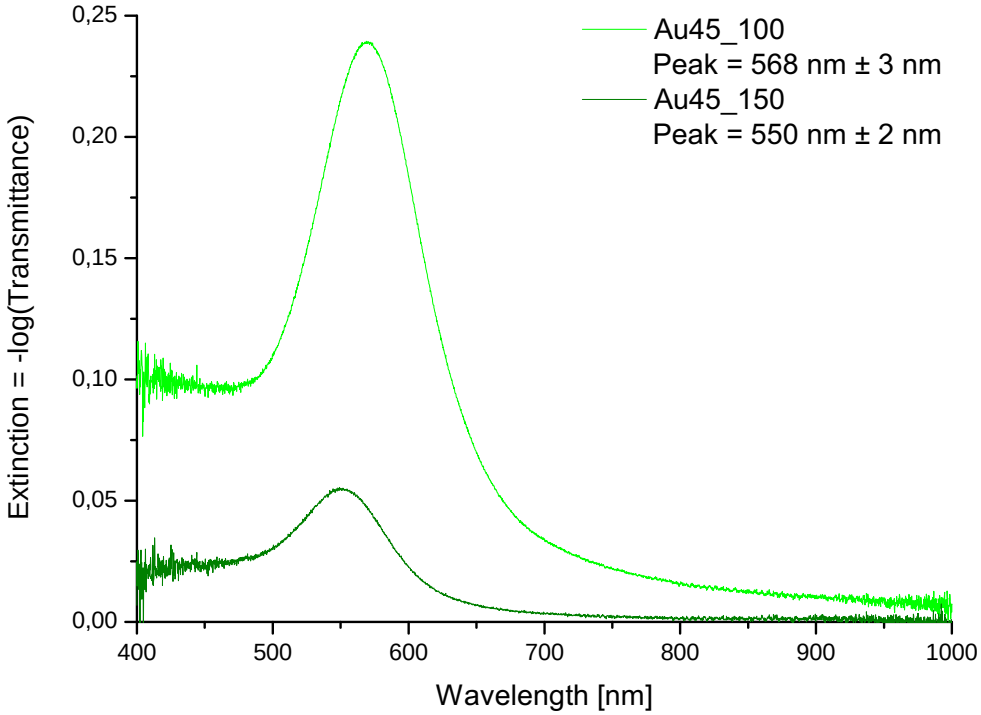

Figure 6.10: Extinction spectra of Au45_150 and Au45_100 collected by the means of an integrating sphere. The increased intensity of the latter relative to the former stems from the increased surface coverage, while the redshift and broadening of the extinction maxima originates from neighboring MNPs coupling via their near-field.

observed when the gold NP-array was illuminated under unpolarized light due to oscillations along each of the principle axes of the ellipsoids. Hence, the elliptic shape of the MNP can cause a broader linewidth. Nevertheless, based on the work presented by Håvardstun [9], the elliptic shape of the gold NPs is most likely attributed to the accumulation of charge in the glass substrate and does not necessarily resemble the actual particle shape. The extinction peak of Au45_150 is located at 550 nm $\pm$ 2 nm. Langhammer et al. [52] studied the optical properties of non-interacting gold NP with a diameter of 38 nm and 51 nm and a height of 20 nm deposited on glass by the means of hole-mask colloidal lithography (HCL). The LSPR wavelengths were found to be 540 nm $\pm$ 30 nm for the smaller gold disks and 580 nm $\pm$ 30 nm for the larger gold disks. This is in good agreement with the LSPR wavelength of 550 nm $\pm$ 2 nm of the Au45_150 array presented in Fig. 6.10. It should be noted that the height of the MNP produced within this thesis work is found to be 26 nm $\pm$ 1 nm. The height of silver NP has been demonstrated to strongly influence the LSPR wavelength. Jensen et al. [78] fabricated triangular shaped silver nanoparticles of diameter 90 nm $\pm$ 6 nm using nanosphere lithography to study the sensitivity of the extinction maxima upon the nanoparticle height. The extinction maximum of a silver NP of height 58 nm was found to be 501 nm, whereas the extinction maximum of a silver NP of height 53 nm was found to be 517 nm. The extinction maximum thus redshifted when the height of the particles decreased.

In Au45_100 neighboring particles are expected to interact via their near-field [25]. A great amount of research exists on near-field coupling between adjacent particles using different polarization of light [74, 25]. The light signals collected at the output port of an integrating sphere set-up are, as described in Chapter 4.6, virtually unpolarized independent upon incident polarization. Nevertheless, the effect of near-field coupling upon the LSPR wavelength will be evaluated in terms of incident polarization. Rechberger et al. [25] studied this effect in a system consisting of two gold NP, which were treated as interacting dipoles. When the polarization of the incident light was parallel to the long-pair axis the LSPR broadened and redshifted relative to an isolated dipole. This was attributed to the Coulomb attraction between the dipoles, which gave rise to a weakening of the restoring force on the oscillating electrons. On the other hand, when the incident light polarization was perpendicular to the long-pair axis the restoring force was reduced, evident as a blueshift of the LSPR as well as a broadening of the peak. Under unpolarized light illumination, the parallel polarization prevail [79], so the net result is a broadening and a redshift of the LSPR position, as observed in Fig. 6.10.

Effect of MNP size on the LSPR wavelength

The arrays Au30_90 and Au45_150 should in principle exhibit similar optical properties, as the nominal surface coverage of the two arrays is identical as well as the constituent metal. However, the nominal particle diameter of Au30_90 is 30 nm $\pm$2 nm while the nominal particle diameter of the Au45_150 is 45 nm $\pm$ 1 nm. As a consequence, the LSPR wavelength of the former should blueshift relative to the latter. Furthermore, Juve et al. [49] concluded that radiative decay becomes negligible when the size of the MNP is less than 30 nm. Hence, disregarding the polydispersivity in the size distribution, the bandwidth of the two extinction spectra should be similar. As can be seen from Fig. 6.11, this is not the case. The LSPR position of Au30_90 is significantly redshifted with respect to Au45_150. As discussed in Section 6.2.1, the size distribution of Au30_90 is the largest of the produced arrays. Additionally, the particle diameter was found to increase along the diagonal of the array. Hence, the MNP diameter of Au30_90 frequently exceeds the nominal diameter and particle-particle coupling most likely influences the extinction spectrum. The effect of near-field coupling upon the extinction spectrum is discussed in detail in the section above. The closing remarks are; the redshift and broadening of the extinction maximum of Au30_90 relative to Au45_150 originates from near-field coupling between neighboring particles, while the increase in extinction efficiency is attributed to the increase in surface coverage. This indicates, as discussed by Langhammar et al. [52], that a center-to-center spacing of magnitude 3 times particle diameter is the smallest interparticle distance at which the optical properties of the MNPs resembles single-particle properties.

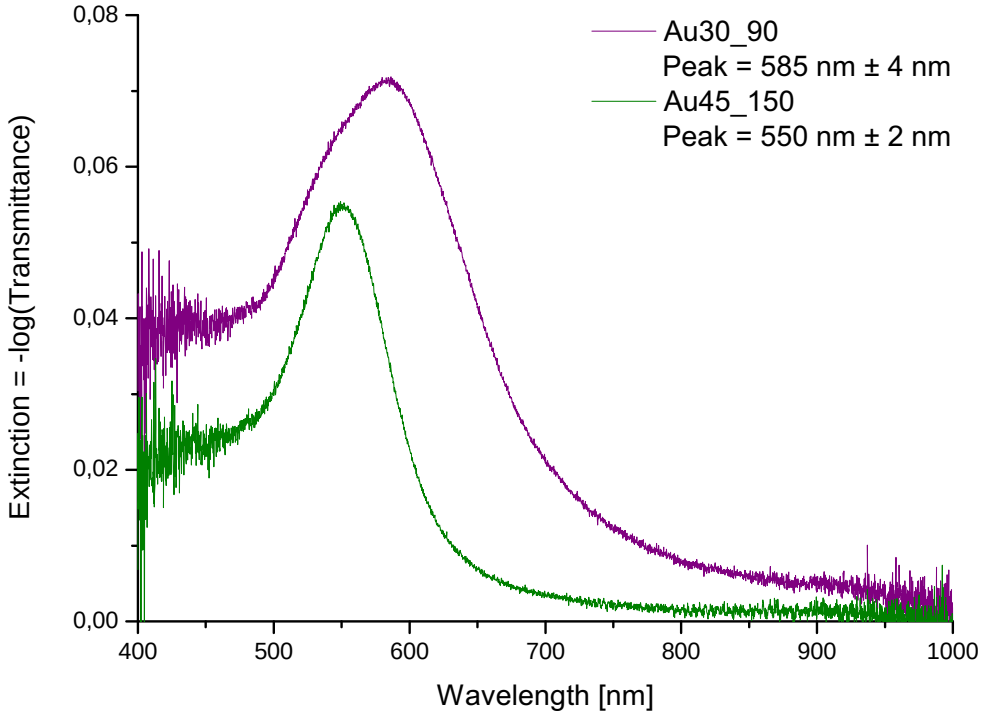

Figure 6.11: Measured extinction spectra of Au45_150 and Au30_90. The LSPR wavelength of Au30_90 is significantly redshifted and broadened with respect to Au45_150. This is attributed to near-field coupling between neighboring particles.

6.5 Modeling the NP Spectroscopy Data

This section presents model extinction spectra of spheroidal MNPs truncated by a glass substrate calculated using the GranFilm code (described in Chapter 3). Model spectra are compared to experimentally measured extinction spectral obtained in the work by Håvardstun [9] and Greve et al. [73] (Modeling of old measurements) as well as in the present work (Modeling of new measurements). If not otherwise specified the extinction spectra are collected by the means of an integrating sphere (see Chapter 4.6). As stated above, due to the limitations on the light source of the integrating sphere set-up, the spectra are presented in the spectral range 400 nm – 950 nm. The extinction is plotted as –log(Transmittance) as a function of wavelength (described in Chapter 2.7).

Table 6.7 presents the parameters used in the theoretical calculations of this thesis. The particle radii and the interparticle distances represents the nominal diameter and interparticle distance of the produced MNP arrays within the work by Håvardstun[9] and Greve et al. [73] and the present work. The model particles are truncated by a glass substrate and the ambient medium is either air or SiO_2. Håvardstun [9] coated one gold NP array (nominal Au diameter = 150 nm, nominal interparticle distance = 450 nm) with 40 nm of SiO_2 to study the effect of the surrounding medium upon the LSPR wavelength. Tuning the optical response of MNPs of

surrounded by SiO_2 is highly relevant, as the long-term objective of this thesis is to produce model solar cells, in which the MNPs are embedded in a glass matrix. The truncation ratio is kept constant throughout this work and the model MNP are arranged in a periodic square array. The model spectra are calculated using unpolarized light incident normal to the MNP arrays (MNP facing the incident light). The bulk dielectric functions of the various media are taken from the SOPRA database [61]. However, this database does not contain the dielectric constant of borosilicate glass. The manufacturer Thermo Scientific states that the dielectric constant of borosilicate coverslips is approximately $\sqrt{1.52}$ across the visible range of the electromagnetic spectrum [76]. The dielectric constant of the substrate was therefore set to be $\sqrt{1.52}$.

Table 6.7: Input parameters used in the GranFilm runs of this thesis

Parameter Set	
Metal	Gold, Aluminium, Nickel
Surrounding medium	Air, Silica (SiO_2)
Substrate	Glass ($\varepsilon = \sqrt{1.52}$)
Radius/Height	25 nm
Diameter	30 nm, 45 nm, 150 nm
Truncation Ratio t_r	0
Interparticle distance	90 - 450 nm
Arrangement	Square Array
Inter-particle interaction	Dipolar

6.5.1 Modeling of Old Measurements

The section encloses a comparison of model extinction spectra calculated by the GranFilm code (see Chapter 3) to measured extinction spectra recorded in the work of Håvardstun [9] and Greve et al. [73]. Håvardstun established an EBL production method for fabricating large MNP arrays as well as a procedure for analyzing the optical properties of the arrays. As in the present work work, the objective was to analyze the optical properties of the fabricated arrays for solar cell applications. The extinction spectra of the gold and aluminium MNP arrays presented in this section is recorded by the means of the thin-film analyzer (see Chapter 4.5). The nominal diameters of the MNPs were in the range 45 nm - 150 nm with a fixed interparticle distance of 450 nm. Unpolarized light was incident normal to the MNP arrays and the light transmitted directly through the array was collected. A schematic of the set-up can be found in Fig. 4.6. The following subsections are named according to the name of the samples in the work of Håvardstun and Greve et al. [9, 73]. A comparison between extinction spectra obtained using the thin-film analyzer and the integrating sphere set-up is given in Section 6.6.

AuG

The extinction spectrum of a 4 mm $\times$ 4 mm gold NP array, in which the nominal diameter of the particles are 150 nm, the interparticle distance 450 nm and the height 25 nm is depicted in Fig. 6.12 together with a model extinction spectrum of truncated spheroidal NP with a diameter of 150 nm, an interparticle distance of 450 nm and a height of 25 nm.

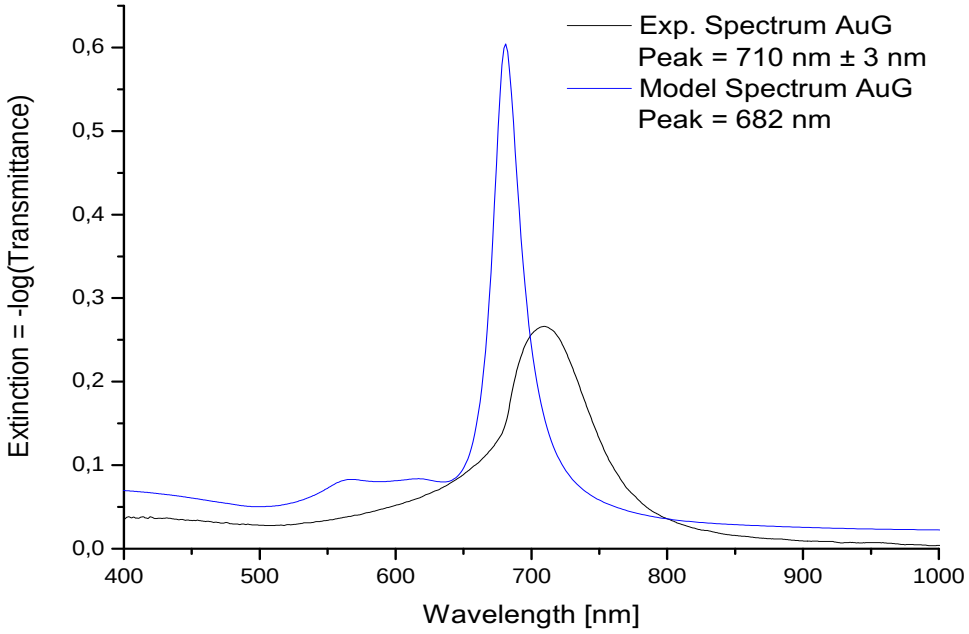

Figure 6.12: Modeled and measured extinction spectrum of AuG. The model spheroids have a diameter of 150 nm, a height of 25 nm and an interparticle distance of 450 nm. The nominal diameter, height and interparticle distance of the Au NP were 150 nm, 25 nm and 450 nm, respectively.The discrepancies between the two spectra are attributed to the difference in shape and size as well as to the polydispersity in particle diameter present in the fabricated array.

The resonance condition of the model spectrum is satisfied at 681 nm, while the spectral position of the LSPR wavelength of the measured spectrum is found to be 710 nm $\pm$ 3 nm. This redshift of the latter relative to the former is related to the difference in shape and size of the two MNP systems. The actual MNPs are disk-shaped, whereas the modeled MNPs are truncated spheroids. As a consequence, the actual MNPs have a larger volume than the modeled MNPs. According to Mie theory, described in Chapter 2.6, a larger distance between the conduction electrons and the ion cores reduces the restoring force, which in turn causes a lowering of the resonance energy (or in this context an increase in resonance wavelength). There is no exact theory of the absorption and light scattering of non-spherical NPs [80]. In order to qualitatively evaluate the effect of the difference in size, a model extinction spectrum of truncated gold NPs of identical volume to that of the nominal volume of the fabricated gold NPs is presented in Fig. 6.13. This corresponds to truncated spheroids with a diameter of 180 nm and a height of 25 nm. It is important to emphasize that the shape of the MNPs in

the two systems are not alike, they just share the same volume. The LSPR wavelength of the model system is in this case found to be 703 nm, which is in much better agreement with the experimental result. This indicates that it is the difference in volume that primarily causes the redshift.

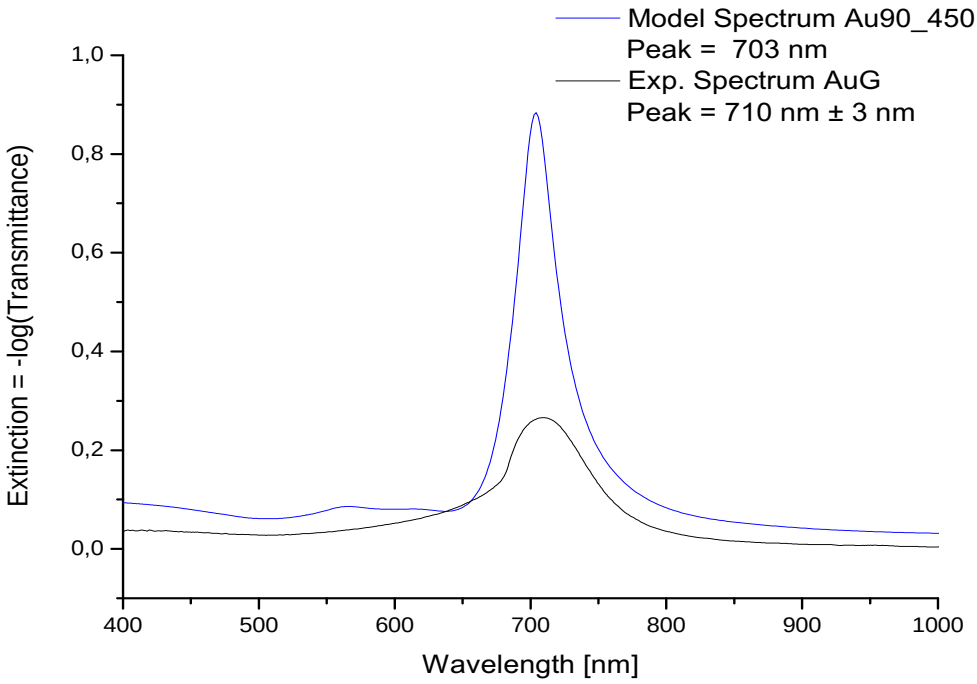

Figure 6.13: Model spectrum of truncated spheroids with a diameter of 90 nm, a height of 25 nm and an interparticle distance of 450 nm. These dimensions corresponds to the nominal volume of AuG_1, whose extinction also is depicted.

The measured spectrum has a broader linewidth (FWHM) than the corresponding model spectrum. First and foremost, this broadening of the LSPR stems from the polydispersity in MNP size within the array. EBL is a fabrication method where such inhomogeneous broadening can be minimized, but compared to a monodisperse model system it is by no means negligible. Additionally, periodic arrays of identical MNPs can be subjected to far-field coupling via diffraction when the interparticle distance exceeds the distance at which near-field coupling prevails [28]. As mentioned in Chapter 4.5, the experimental detector has a low angle of acceptance, meaning that to a large extent only the light directly transmitted through the sample (i.e. the zeroth order of diffraction) is collected. The GranFilm detector, on the other hand, collects all diffraction orders. Temple et al. [51] studied the effect of periodicity by fabricating square arrays of gold NP and comparing the optical properties of the square array to a randomly distributed array of equal coverage. The diameter of the gold NP (in the random and ordered array) was 150 nm and the interparticle distance in the ordered array was 500 nm. The extinction spectrum of the random array featured a broad and more or less symmetric peak, while the peak of the periodic array was narrower, higher and asymmetric. The extinction maximum of the square array was significantly redshifted relative the peak position of the

randomly distributed one. They attributed this difference to the constructive and destructive interference of scattered waves caused by diffractive orders. However, the polydispersity in particle size in the produced array as well as the difference in shape and size between the two systems makes it hard to evaluate whether diffraction orders are present in the model system. The periodicity of the fabricated array is further evaluated in Section 6.6 and is found not to induce far-field coupling via diffraction. The discrepancies between the model and measured extinction spectra are therefore attributed to the polydispersity in particle size in the produced array (causing a broadening of the peak) and difference in shape and size between the two systems (causing a redshift of the produced array).

The increased intensity at left tail of the extinction is attributed to interband transitions in gold. However, the model spectrum features a plateau at around 550 nm that is not present in the measured spectrum. The model system support two dipolar resonances, a low energy (long wavelength) resonance which is highly dependent upon the shape and size of the MNP as well as a high energy (short wavelength) resonance which is a characteristic property of the constituent metal (i.e. non-dispersive). The latter resonance can only be excited by perpendicular polarization of incident light and can therefore not be present as the light is incident normal to the MNP array. Furthermore, the plateau cannot be a quadrupole resonance since higher order resonances are excited at longer wavelengths than the dipolar resonance [41]. The presence of the plateau is not truly understood. It can be further evaluated by plotting the calculated potentials of the modeled system. However, within the timeframe of the present work, this was not accomplished.

AlG

Figure 6.14 present the model and measured extinction spectra of aluminium NP. The nominal particle diameter of the fabricated array is 150 nm, the interparticle distance 450 nm and the height 25 nm. The model spectrum is calculated using identical parameters. As in the case of AuG, the measured extinction spectrum is significantly redshifted with respect to the modeled one. However, in the case of AlG this redshift is only partly attributed to the discrepancies in size and shape between the model and fabricated aluminium NPs. A thin layer of Al_2O_3 (aluminium(III) oxide) forms spontaneously when aluminium is in contact with air. This Al_2O_3-layer will reduce the diameter of the aluminium particle and increase the refractive index of the local surrounding medium (the refractive index of Al_2O_3 is approximately 1.8) and this is not included in the GranFilm calculations. Langhammer et al. [48] concluded that this oxide layer affected the spectral position of the LSRP in the following ways; firstly, the increase of refractive index of ambient resulted in a redshift and secondly the decrease of the size of the aluminium MPs gave rise to a blueshift. The net result was a redshift of the peak position, indicating that the increase of refractive index of the surrounding medium prevails over the decrease in size. Therefore, the larger discrepancies of the extinction maxima of the

model and measured aluminium systems with respect to the AuG (see Fig. 6.12) is attributed to this final coating-layer on the produced aluminium NPs.

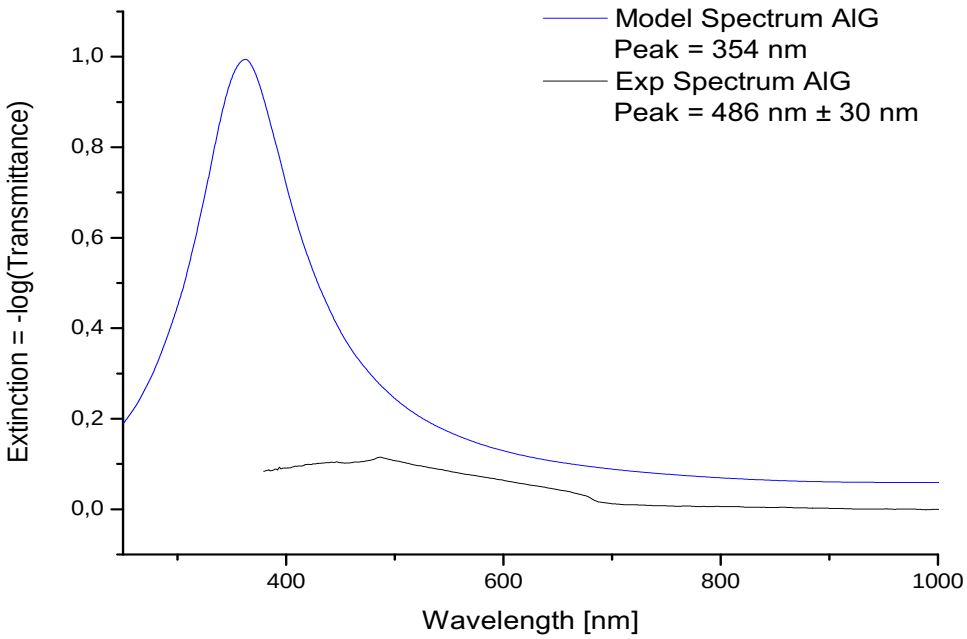

Figure 6.14: Modeled and measured extinction spectrum of AlG_1. The model spheroids have a diameter of 150 nm, a height of 25 nm and an interparticle distance of 450 nm. The nominal diameter, height and interparticle distance of the aluminium NP were 150 nm, 25 nm and 450 nm, respectively. The corrected particle diameter along the major and minor axis were 135 nm $\pm$ 4 nm and 120 nm $\pm$ 2 nm, while the corresponding interparticle distances were found to be 440 nm $\pm$ 15 nm and 435 nm $\pm$ 15 nm, respectively. Note that the wavelength range have been increased to fully include the model LSPR peak.

AuG_SiO2

Håvardstun [9] coated a gold NP array, of identical particle dimensions as AuG (see Fig. 6.12), with 40 nm of SiO_2 in order to qualitatively study the effect of the surrounding medium upon the extinction maximum. Figure 6.15 presents the measured and modeled extinction spectra of AuGSiO2. The Frönlich condition (described in Chapter 2.4.1) states that increasing the refractive index of the surrounding medium causes a redshift of the LSPR resonance. A quick estimate of the magnitude of the redshift can be made by excluding the substrate effect and study an isolated MNP (i.e. by embedding a MNP in a homogenous medium). For a Drude metal of negligible damping (see Eq. 2.9) the Frönlich condition is satisfied when $\omega = \frac{\omega_p}{\sqrt{1+\varepsilon_m}}$. The bulk plasma frequency of gold is $\approx 2.2 \times 10^{15}$ s^{-1} [28] and the refractive index ($n = \sqrt{\varepsilon}$) of glass and air is 1.5 and 1, respectively. The Frönlich condition implies that the extinction maxima will redshift with 45 nm when changing the surrounding medium from air to glass. This is in good agreement, both experimentally and theoretically, with the extinction maxima

presented in Fig. 6.12 and Fig. 6.15. The discrepancies between the model extinction and the measured extinction are as discussed above, attributed to the difference in size, shape and particle-size distribution between the two systems.

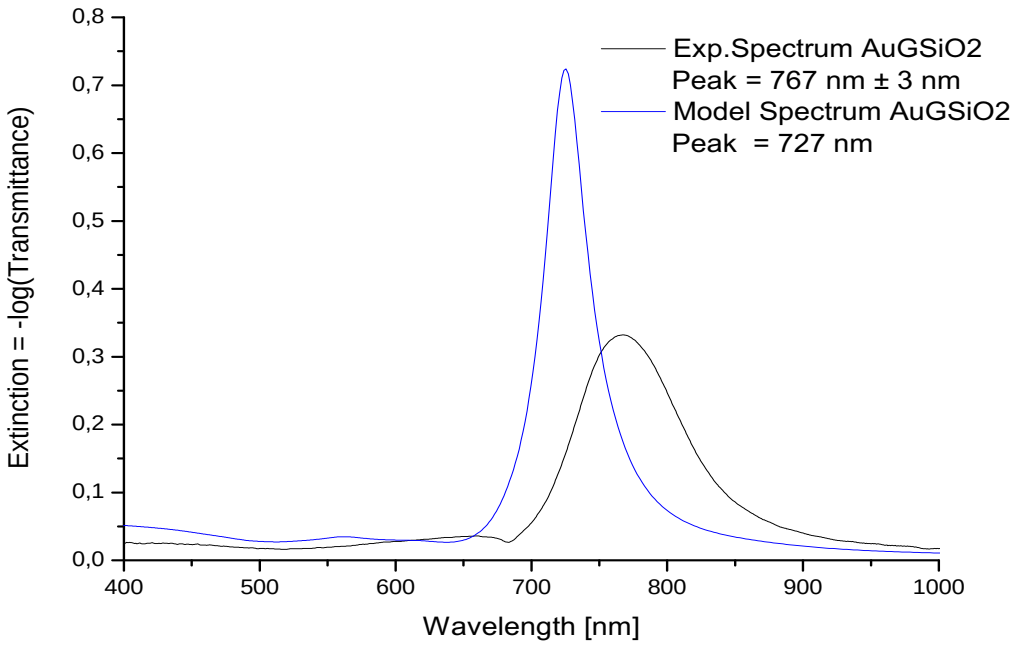

Figure 6.15: Modeled and measured extinction spectra of AuGSiO2. The model spheroids have a diameter of 150 nm, a height of 25 nm and an interparticle distance of 450 nm. The nominal diameter, height and interparticle distance of the Au NP were 150 nm, 25 nm and 450 nm, respectively. The corrected particle diameter along the major and minor axis were 138 nm $\pm$ 6 nm and 123 nm $\pm$ 4 nm, while the corresponding interparticle distances were found to be 440 nm $\pm$ 20 nm and 440 nm $\pm$ 15 nm, respectively. The array is coated with a 40 nm layer of silica.

Au_dot

Figure 6.16 presents the measured and model extinction spectra of Au NPs with a nominal diameter of 45 nm and an interparticle distance of 450 nm. AuG_dot1 featured a large size distribution; ranging between 40 nm and 80 nm. This is evident in the extinction spectra as a large linewidth. However, an exact value of the linewidth could not be obtained due to the noise level of the data, which is attributed to the low surface coverage (($\approx 8 \times 10^{-3}$). Nevertheless, the trends outline above is obtained. The spectral position of the measured spectrum is redshifted with respect to the model spectrum and the FWHM is narrower in the case of the modeled MNPs. The minor peak located in the model spectrum at approximately 650 nm is discussed in greater detail in Section 6.5.2.

To summarize; the extinction spectra obtained using the GranFilm code have been compared to the experimental spectra obtained in the work of Håvardstun [9] and Greve et al.

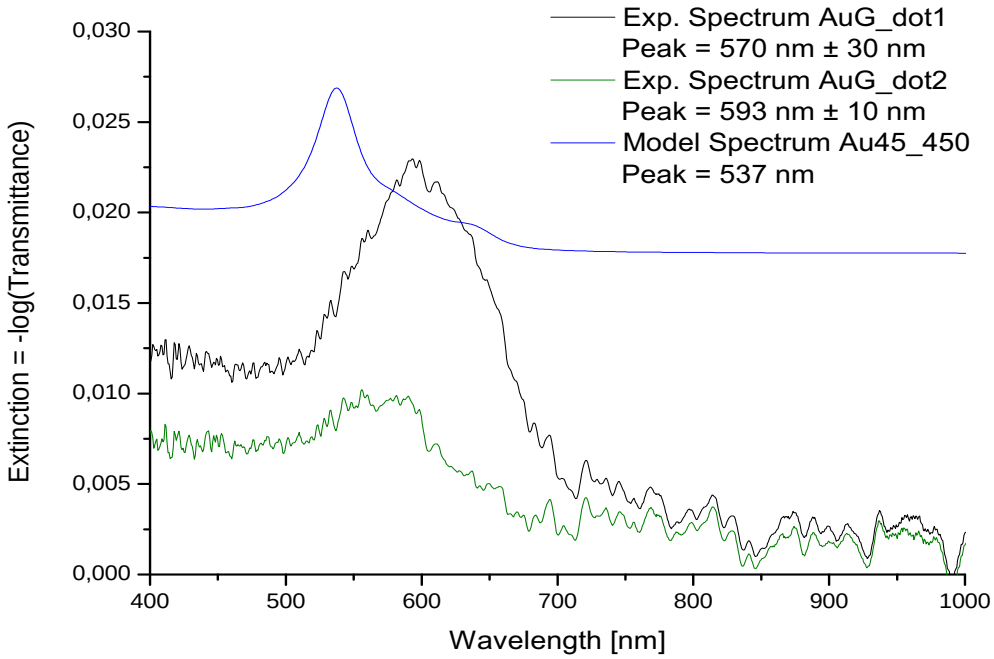

Figure 6.16: Modeled and measured extinction spectra of AuGdot_1 and AuG_dot2. The nominal diamater and interparticle distance of the Au NP were 45 nm and 450 nm, respectively. AuGdot_1 featured a large size distribution, the corrected diameter was found to be 65 $\pm$20 nm. The corrected interparticle distance of the AuGdot_1 array along the minor and minor axis were 450 nm $\pm$ 15 nm and 445 nm $\pm$ 15 nm. The corrected diameter of AuG_dot2 was 44 nm $\pm$ 3 nm and the corrected interparticle distance along the major and minor axis was 440 nm $\pm$ 15 nm.

[73]. The underlying theory of GRANFILM is valid in the quasi-static regime [43]. In order to maintain the validity of the quasi-static approximation a rule of thumb is that D $<$ 100 nm [81], where D is the particle diameter. A MNP with diameter of 150 nm is in principle not adequacy described by electrostatic theory due to the phase-retardation of the incident field over the particle volume. Nevertheless, as a first analysis of the optical properties of the produced arrays GranFilm has a lot to offer. The spectral position of the LSPR of Au NP could be determined within a wavelength range of 100 nm. All respective spectra featured two characteristics:

- The volume of the measured MNPs is larger and the shape of the two MNPs system is different. The net result is a redshift of the LSPR wavelength in the measured spectra with respect to the model spectra.

- The FWHM of the measured spectra are broader than the corresponding model ones. This is attributed to polydispersity in size within the produced arrays

6.5.2 Modeling of New Measurements

This section encloses a comparison of model extinction spectra obtained by the GranFilm code and measured extinction spectra collected in this work. The nominal dimensions of the produced samples are tabulated in Table 6.1. All measured spectra are obtained using the integrating sphere set-up. A schematic as well as a description of the set-up can be found in Chapter 4.6. The produced arrays are characterized by their nominal diameter and interparticle distance (see Table 6.4), due to the charging effect described in Section 6.2.1.

Au45_150

Figure 6.17 presents the model extinction spectrum of truncated spheroids with a diameter of 45 nm and a height of 25 nm situated in a square array of interparticle distance 150 nm as well as the measured extinction spectrum of Au45_150. The extinction maxima are found to be 550 nm $\pm$ 2 nm and 535 nm for the measured and model spectra, respectively. The minor peak at approximately 650 nm present in the model spectrum could be interparticle transitions in gold. However, interband transitions, that is, electron-hole generation and decay of excited electrons from the d-orbital to the sp-orbital is expected for wavelengths less than 520 nm [82]. The minor peak (present in all the spectra below) might be the quadrupole resonance, as higher order resonances are redshifted with respect to the dipolar resonance [41]. However, this is only speculations. The presence of the minor peak is not truly understood. It can be further evaluated by plotting the calculated potentials of the modeled system. However, within the timeframe of the present work, this was not accomplished.

GranFilm is an electrostatic model. As a rule of thumb, particles with diameter less than 100 nm can be well described using electrostatic approaches [52]. Hence, the model should describe the optical response of MNPs of diameter 45 nm well. Indeed, it is found that the extinction maximum can be determined within a wavelength range of 15 nm $\pm$ 2 nm.

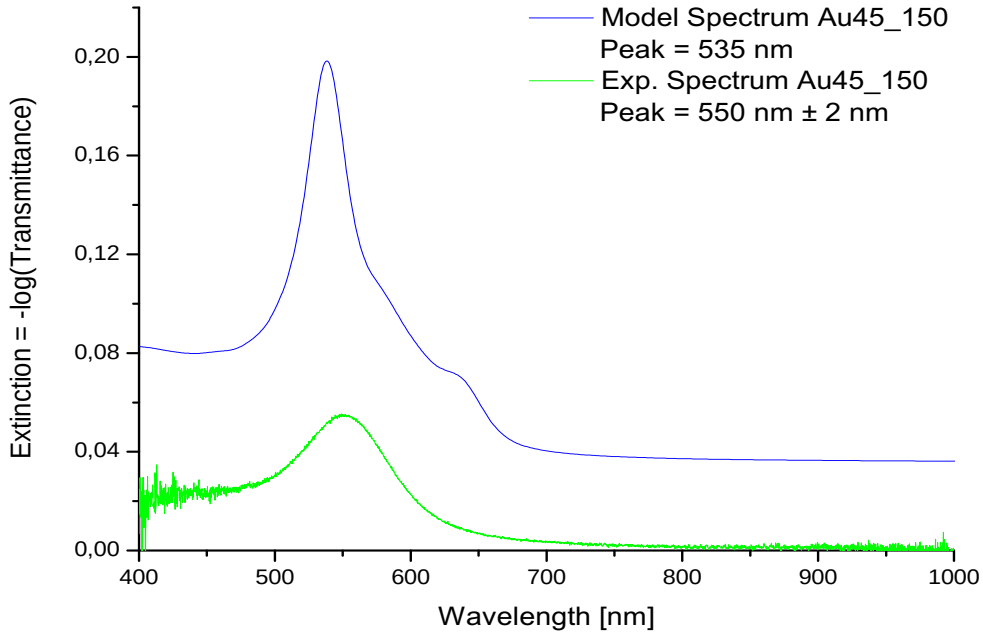

Figure 6.17: Modeled and measured extinction spectra of Au45_150. The particle diameter of Au45_150 was found to be 43 nm ± 2 nm and 40 nm ± 4 nm along the y- and x-axis, respectively. The corresponding interparticle distances were 140 nm ± 2 nm and 132 nm ± 4 nm. The sample-dimension measurements are obtained under charging conditions and is therefore smaller than the expected dimensions of the array. The discrepanties in LSPR wavelength originates from the difference in volume and size.

Au45_100

The extinction spectrum of Al45_100 is presented in Fig. 5.18 in addition to the corresponding model extinction spectrum. In such dense arrays, neighboring particles are expected to interact via their near-field. Under unpolarized light illumination, the net effect of this coupling is a redshift and a broadening of the LSPR peak relative to an isolated MNP [25]. However, in Fig. 6.17 the model spectrum seems to be significantly less redshifted than the experimental one. A model spectrum in which quadrupolar particle-particle interactions were taken into account was calculated to see if this affected the magnitude of the redshift. The discrepancies between the dipole model system and the quadrupolar model system were found to be negligible. However, this does not necessarily indicate that the size distribution within the array is broad, since a broad size distribution is accompanied by a decrease of the peak maximum and the height of the peaks in Fig. 5.18 are found to be in excellent agreement. In order to study size distribution within the array in greater detail the sample must be coated with a conductive layer. The extinction maximum can be determined within a wavelength range of 28 nm ± 3 nm.

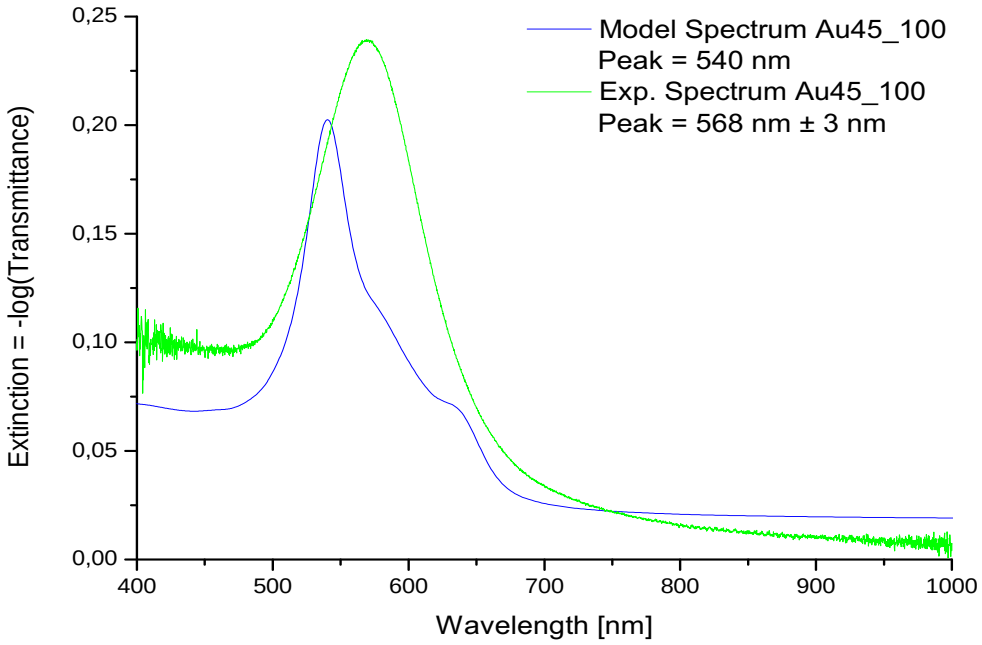

Figure 6.18: Model and measured extinction spectra of Au45_100. The particle diameter of Au45_150 was found to be 43 nm ± 2 nm and 42 nm ± 4 nm along the major and minor axis, respectively. The corresponding interpartle distances were 97 nm ± 4 nm and 94 nm ± 2 nm, respectively. In both spectra, particles are expected to interact via their near-field.

Au30_90

The measured extinction spectrum of Au30_90 as well as the extinction spectra of two model systems is presented in Fig. 6.19. The model extinction spectra are based on spheriodal gold NPs of diameter 30 nm and 40 nm, a height of 25 nm and an interparticle distance of 90 nm. The measured spectrum is significantly redshifted and broadened with respect to the two model spectra. The broadening is attributed to the broad size distribution within the array, the average particle diameter was found to be 30 nm ± 8 nm and 31 nm ± 7 nm along the y-axis and x-axis, respectively. As the particle diameter exceeds the nominal size of the array, neighboring particles are expected to couple via their near-field, which causes a redshift as well as a broadening of the extinction maxima. Nevertheless, based on the measured particle dimensions, the extinction spectrum of the LSPR of Au30_90 should not be significantly redshifted with respect to the model spectra of gold nanoparticles with a diameter of 40 nm. This indicates that the shrinking effect caused by the accumulation of charge in the glass substrate does perhaps not approach unity as the particle density increases, but remains constant as assumed in the work presented by Håvardstun [9]. However, the good agreement between the model and measured spectra of Au45_150 and Au45_100 support the assumption of a systematically changing charge-correction factor. The discrepancies between the model and measured spectra are therefore attributed to the broad size distribution within the produced array. The extinction

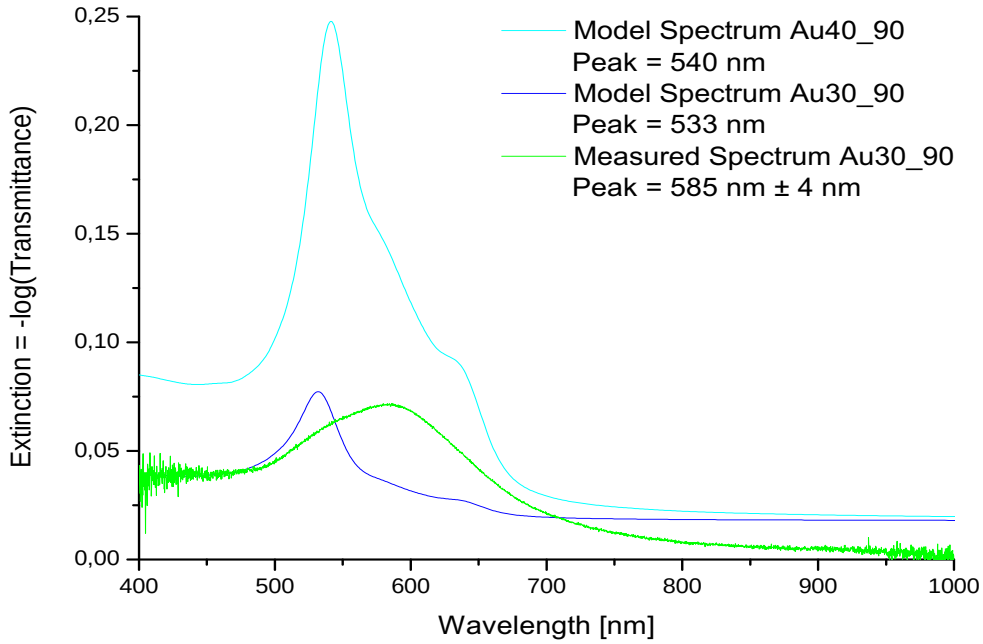

Figure 6.19: Model and measured extinction spectra of Au30_90. The particle diameter of Au45_150 was found to be 30 nm ± 8 nm and 31 nm ± 7 nm along the major and minor axis, respectively. The corresponding interpartle distances were 89 nm ± 1 nm and 87 nm ± 2 nm, respectively

maximum can be determined within a wavelength range of 53 nm ± 4 nm.

Al45_150

A model extinction spectrum of Al45_150 are given in Fig. 6.20. The extinction maximum is located at 290 nm. Although a UV-VIS spectrometer (wavelength range 200 nm – 1100 nm) as well as a deuterium tungsten halogen light source (wavelength range 200 nm - 2000 nm) was at hand, the optical fiber suffered from transmission loss which resulted in minimal or no signal in the wavelength range (250 nm – 400 nm) where the LSPR was expected to be. Langhammer et al [48] studied the LSPR peak of aluminium disk deposited on a glass substrate. As described above, when aluminium is in contact with air a thin layer of Al_2O_3 forms. This spontaneous coating will reduce the diameter of the aluminium particle and increase the refractive index of the surrounding medium (n of Al_2O_3 is approximately 1.8). By the means of a spheriodal electrostatic theory Langhammar et al. quantified the effect of this final coating layer. They assumed that the thickness of the AlO_2 was 3 nm. In the case of an ensemble of aluminium NPs with a diameter of 61 nm the resonance wavelength was found to redshift approximately 35 nm (from 300 nm ± 30 nm to 335 nm ± 30 nm) due to this oxide layer. These results indicate that the extinction maximum of Al45_150 will be located at approximately 325 nm.

By ignoring the effect of the constituent metal, the discrepancies of the two Au45_150 systems can be used to estimate the extinction maximum. The spectral position of LSPR in Al45_150 is therefore expected to be in the range 320 nm – 360 nm ± 30 nm.

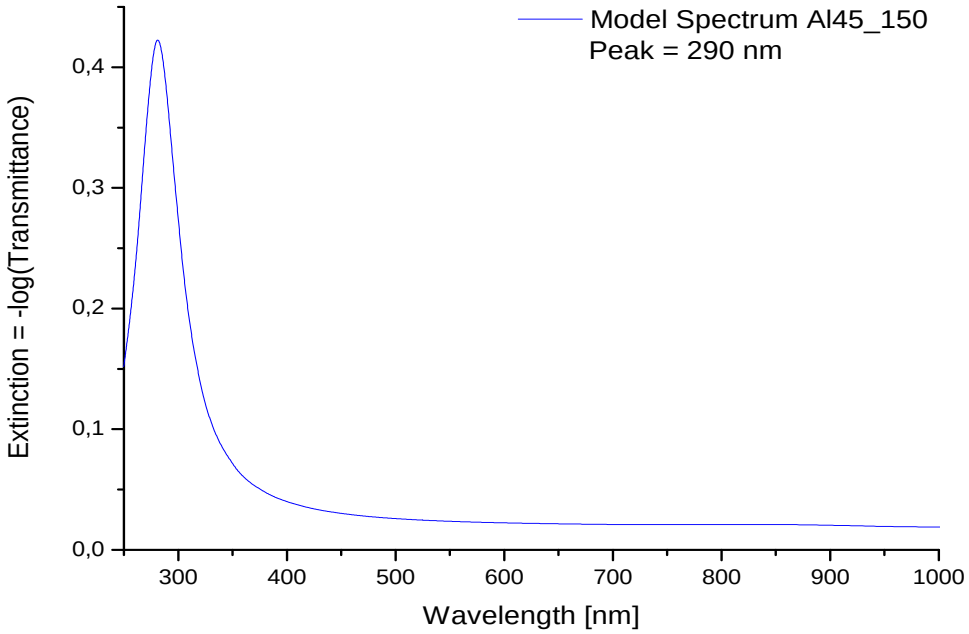

Figure 6.20: Model extinction spectrum of Al45_150. The peak is located at 290 nm. Experimental extinction spectrum of Al45_150 could not be obtained due to limitations in the optical fiber. Nevertheless, the extinction maximum is expected to be located at around 320 nm - 360 nm ± 30 nm.

Ni45_150

A model extinction spectrum of Ni45_150 are presented in Fig. 6.21. A first peak is located at 370 nm. As discussed above, the experimental extinction spectrum of Ni45_150 could not be obtained, because the optical fiber suffered from transmission loss.

In contrast to noble metals, such as gold and silver, nickel NPs have not received a great amount of attention with respect to its optical properties. Nevertheless, it has been experimentally and theoretically verified that nickel NP support LSPR [83]. Pirazadeh et al. [84] studied nickel nanodisks deposited on fused silica by the means of hole-mask colloidal lithography. The extinction maximum of nickel NPs of diameter 110 nm and a height of 20 nm was found to be located at 495 ± 40 nm, while nickel disks with a diameter of 52 nm and a height of 20 nm was located at 360 nm ± 40 nm. The peaks, as in Fig. 6.21, were not as pronounced or as intense as the extinction peak of noble metal. The nickel resonance is weaker due to the larger imaginary part of the dielectric function (see Chapter 2.2) [83]. Pirazadeh et al. [84] also observed a second peak located at around 270 nm that exceeded the intensity of the LSPR peak. This second peak was attributed to interband transitions in Nickel.

The same trends observed byPirazadeh et al [84] is found in the model spectrum of Ni45_150. The emerging peak at low wavelengths is attributed to interband transitions in nickel. It is therefore expected, based on the difference in size and shape betweeen the model and experimental system as well as the polydispersity of size of the produced array, that the extinction peak of Ni45_150 is located in the range 300 nm - 400 nm.

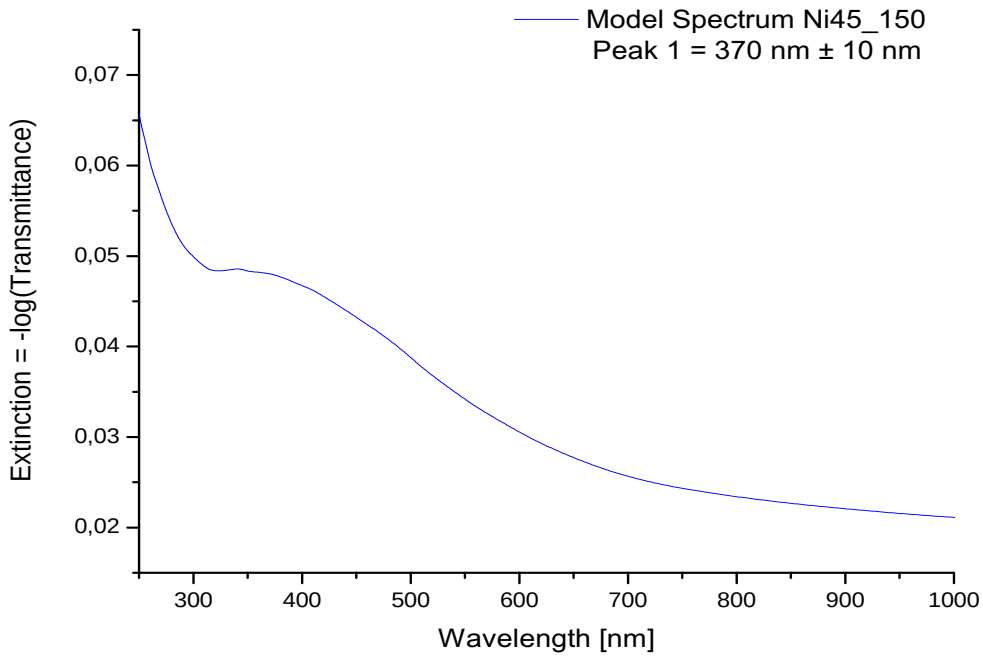

Figure 6.21: Model extinction spectra of Ni45_150. A first peak is located at 370 nm $\pm$ 10 nm.

6.6 Integrating Sphere versus Transmission Spectroscopy

The thin-film analyzer can, as described in Chapter 4.5, only detect the light directly transmitted through a sample (i.e. specular transmission). An integrating sphere, on the other hand, captures the light transmitted in all spatial directions (i.e. diffuse and specular transmission). As discussed in Section 6.5.1, Temple et al [51] studied the effect of far-field coupling via diffraction by fabricating a square array of gold NP and comparing the optical properties of the square array to a randomly distributed array of equal coverage. The extinction spectrum of the random array featured a broad and more or less symmetric peak, whereas the peak of the periodic array was narrow, higher and asymmetric. The extinction maximum of the square array was significantly redshifted relative the peak position of the randomly distributed one. They attributed this difference to the constructive and destructive interference of scattered waves caused by diffractive orders. Hence, if the periodicity causes far-field coupling

via diffraction, the extinction spectra collected by the means of an integrating sphere should feature the same characteristics as the extinction spectrum of the ordered array in the work of Temple et al, while the extinction spectra obtained using the thin-film analyzer would share the same attributes as the disordered array. Note that AuG_dot has been excluded due to the noise level of the data. As is evident from Fig. 6.22 and 6.23, the arrays are not subjected to far-field coupling via diffraction. The AuGSiO2 spectra are almost identical, while the extinction spectra of AuG feature some discrepancies. This might be attributed to a degradation of the MNPs arrays over time, which should not be present in AuGSiO2 as the silica coating shields the array. In summary, the arrays fabricated by Håvardstun [9] exhibit single-particle optical properties.

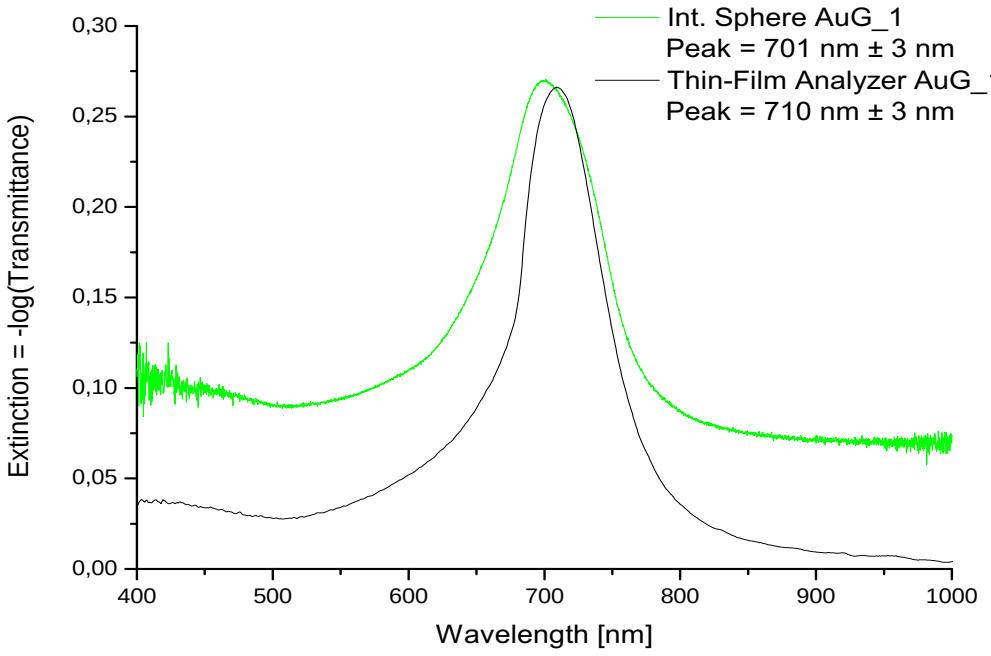

Figure 6.22: Extinction Spectra of AuG obtained using the integrating sphere set-up and the thin-film analyzer. By comparing the two spectra it is found that AuG exhibit single-particle optical properties.

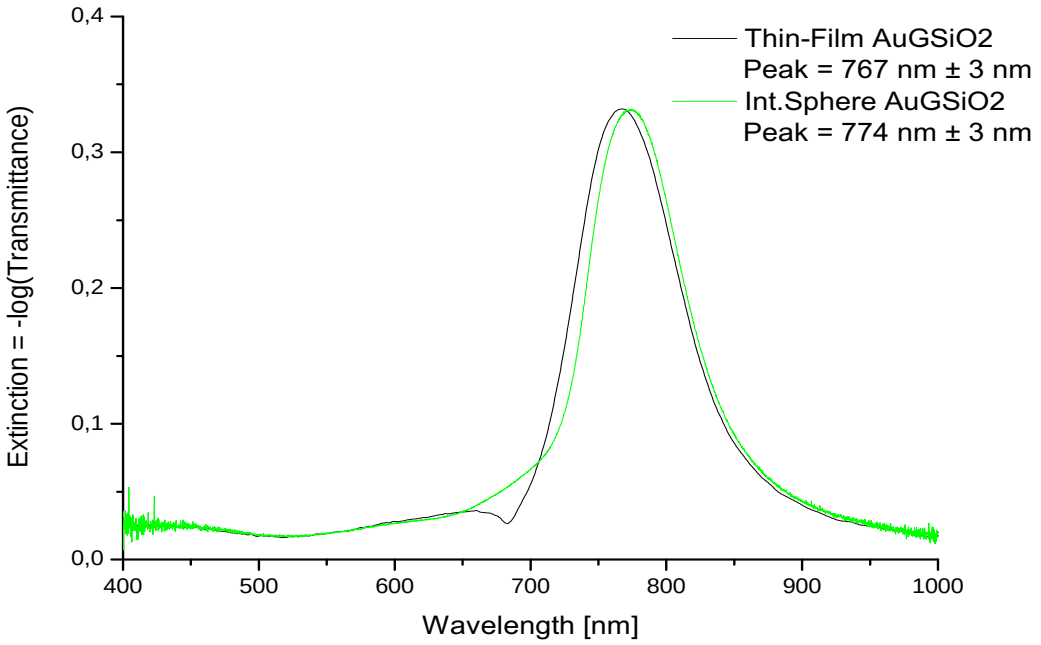

Figure 6.23: Extinction Spectra of AuGSiO2 obtained using the integrating sphere set-up and the thin-film analyzer.By comparing the two spectra it is found that AuGSiO2 exhibit single-particle optical properties

6.7 Comparing the New Results with Existing Work

The results from the optical analysis obtained in this work work have been compared to published work obtained by others. The results are summarized in Table 6.8. All tabulated values are based on disk-shaped MNPs deposited on a transparent substrate. Only arrays of interparticle distance larger than 3 times the diameter of the particle is tabulated.

Table 6.8: Extinction maxima obtained by others in studies on gold and aluminium NPs. The samples are produced using electron beam lithography (EBL) or hole-mask colloidal lithography (HCL). The extinction maxima obtained by other research group was read of plot. The extinction maxima could be determined within a wavelength range of ± 30 nm. In all the tabulated values are the interparticle distance larger than three times the particle diameter.

Research Group	AuNP Diameter [nm]	AuNP Height [nm]	Extinction maximum [nm]	Production method
Niklasson et al. [85]	28	15	540 ± 30	EBL
This work, Au30_90	**30 ± 2**	**26 ± 1**	**585 ± 4**	**EBL**
Langhammer et al. [52]	38	20	540 ± 30	HCL
This work, Au45_150	**45 ± 1.5**	**26 ± 1**	**550 ± 2**	**EBL**
Langhammer et al. [52]	51	20	580 ± 30	HCL

Research Group	AlNP Diameter [nm]	AlNP Height [nm]	Extinction maximum [nm]	Production method
Langhammer et al. [48]	51	20	430 ± 30	HCL
This work, Al45_150	**45 ± 2**	**25 ± 1**	**320 - 360 ± 30**	**EBL**
Temple et al. [51]	150	20	650 ± 30	EBL

Chapter 7

Conclusion and Suggestions for Further Work

The objective of this thesis work has been to investigate the optical properties of arrays of MNPs both experimentally and theoretically. Large arrays of MNPs have been fabricated by the means of EBL and the optical properties investigated using a new integrating sphere set-up. In addition a theoretical framework for a deeper understanding of the experimental results has been established. The experimental and theoretical analysis of the optical properties confirmed that the extinction maximum is highly dependent on the size of the MNP, the magnitude of the interparticle distance within the array and the constituent metal. Using unpolarized light, near-field coupling between neighboring particles has been found to redshift the extinction maximum with respect to the optical properties of a single-sized particle array. It was furthermore found that the agreement between the electrostatic model and experimental results were good. The LSPR wavelength is also found to be in good agreement with published literature which in most cases is based on much smaller arrays. The theoretical model was also applied on the experimental data obtained by Håvardstun [9], supporting the finding of his work. A new method relying on a bi-layer resist scheme has been established in the UiB NanoStructure Laboratory for both improving the experimental results and allowing the fabrication of significantly smaller particles. Gold nanoparticles with a diameter of 20 nm and an interparticle distance of 60 nm was successfully demonstrated applying this method.

Based on SEM analysis of the 20 nm particles it is believed that producing even smaller particles using EBL will be challenging, especially with respect to electron scattering events in the resist/substrate. Furthermore, the array must be produced within an acceptable time. Therefore, in order to produce large MNP arrays, the write-parameter presented in Table 6.2 should be further optimized. Optimizing the write-parameters to reduce the write-time usually comes with a tradeoff in terms of final resolution.

In the present work, the production of gold nanoparticles with a diameter of 20 nm and an interparticle distance of 60 nm by the means of a bi-layered PMMA was successfully demonstrated. However, based on SEM images of the dose matrices it is believed that producing smaller particles using EBL will be hard, especially with respect to electron scattering events in the resist/substrate. Furthermore, the array must be produced within an acceptable time-

frame. Therefore, in order to produce large MNP array of diameter 20 nm the write-parameter presented in Table 6.2 should be further optimized. However, optimizing write-parameters to reduce the write-time usually comes with a tradeoff in terms of final resolution.

EBL has successfully been shown to produce MNPs with cross-sectional shape (e.g. squares, triangles [51]) different from the disk (i.e. a cylinder). As the extinction maximum is highly dependent upon the shape of the MNPs, production and optical investigation of MNPs with different cross-section shape is suggested to be included in the investigation and optimization of the EnSol solar cell.

The integrated sphere set-up needs to be further investigated. The set-up can in principle separate the contribution of absorption and scattering to the total extinction. This separation can be used to study the absorption efficiency as a function of MNP size to find at which diameter absorption becomes the dominating contributor to the total extinction. The absorption efficiency is directly related to the non-radiative decay of the LSPR and the associated generation of hot electrons; the fundamental process through which the EnSol solar cell will produce electricity. The MNPs of the array Au45_150, Al45_150 and Ni45_150 produced within this thesis work were found, based on SEM images, to take a slightly elliptic shape. Although the elliptic shape is believed to be attributed to the charging effect, it can be further evaluated (without coating the array) by studying the optical response of the arrays using polarized light. The integrating spheres cannot provide any valuable information in this respect, since the spheres emit unpolarized light independent upon incident polarization. Also, the thin-film analyzer cannot be used since polarization is not conserved at normal incidence. This analysis thus requires a set-up capable of varying the angle of incidence.

The UiB has already started the process of fabricating model solar cells. In this case, ITO-covered glass coverslips coated with a thin layer (thickness has not yet been determined) of SiO_2 is used as the underlying substrate. ITO, being transparent and conductive, function as the front electrode contact. The $SiO2_2$ layer electrically isolate the MNPs from the ITO. In addition, a thin layer of SiO_2 is deposited on top of the gold NPs, followed by a thin-layer of metal. The metal function as the back electrode contact.

Appendix A

Prelimenary Integrating Sphere Measurements

This appendix presents preliminary results from the integrating sphere measurements. An integrating sphere was employed in this work so that the contributions of absorption and scattering to the total extinction could be separated.In the introductory experiments, pure glass slides were investigated. The measured reflectance of the glass is lower than it should be indicating that some light is lost. This appendix presents the reflectance and transmittance spectrum of the glass substrate and discusses possible reasons that can give rise to the observed underestimate of the reflectance of glass.

A.1 Reflectance and Transmittance of Glass

Figure A.1 presents the reflectance spectrum of glass collected using the integrating sphere set-up. The manufacturer of the glass coverslips Thermo Scientific [76] states that the transmittance of the glass is approximately 0.94 across all visible wavelengths. A bare glass coverslips, being transparent across all visible wavelength, does not absorb light. As a consequence of conservation of energy the reflectance and transmittance must sum up to 1. Hence, the reflectance of the glass must be around 0.06 across all visible wavelengths. As is evident from Fig. A.1, this is not the case; the reflectance is too low indicating that some list is lost. The ultimate consequence of this underestimate is an underestimate of the amount of light absorbed by the MNPs (see Equation 2.23).

The sample port, entrance port and detector port are not coated with the sphere material and consequently, light will not scatter in all spatial directions at these sites. This is not taken into account and the underestimate of the glass reflectance might be attributed to losses at these sites. However, ports not in use were closed with plugs to minimize such losses. Furthermore, if these losses were significant they should also be present in the transmission sphere. The transmittance of glass is found to be around 0.94 (corresponding to an extinction of 0.03, see Fig. 6.9) in the wavelength range 400 nm - 1000 nm. It is therefore not believed that the underestimate of the reflectance of glass is due to port-losses.

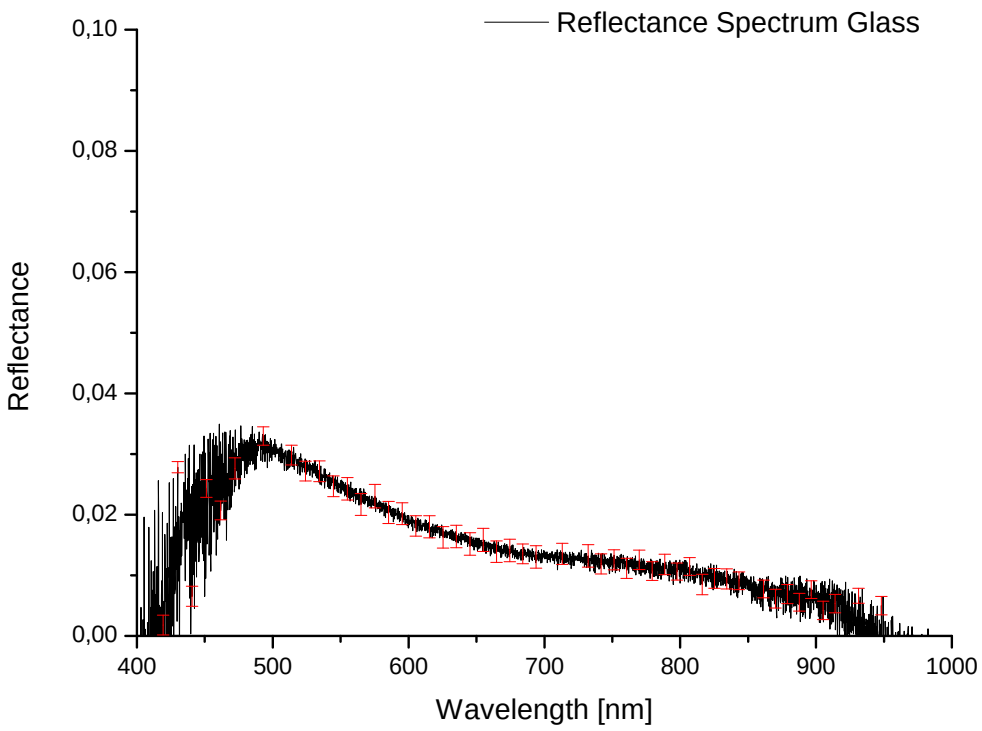

Figure A.1: Average reflectance spectrum of the glass substrate. The spectrum is the average reflectance based on five glass samples. Standard deviation is used as error bars. The noisy tails of the spectrum are attributed to the limited performance of the light source.

The spheres, as discussed in Section 4.6, do not come with a baffle due to the small acceptance angle of the optical fiber and the small radii of the spheres. If the detector collects un-scattered source light, this would give rise to an overestimate of the reflectance (the source light would drown out diffuse signals). Furthermore, a bare glass surface reflects light in the specular direction, so it is highly unlikely that light is reflected off the glass surface in the direction of the detector. By removing the gloss-trap (i.e. excluding the specular component of the reflected light) the reflectance of glass was found to be zero, so the underestimate is not caused by un-scattered source light.

In the post measurement data processing it is taken into account that the coating material of the integrating sphere, experiences some optical losses during the reflection (the factor 0.98 in Equation 2.24). Furthermore, in the reflectance spectrum presented in Fig. A.2 the reflectance of the light source (i.e. an empty sphere) has been subtracted from the raw glass reflectance. This has been done to exclude the contribution of the light that is re-transmitted from the transmission sphere. When light is incident in the reflection sphere, an amount of light will be transmitted through the glass and into the transmission sphere. An amount of this light will be re-transmitted through the glass and into the reflection sphere and so forth. If the contribution of the light re-transmitted from the transmission sphere is not excluded (i.e. the reflectance spectrum of the light source is not subtracted), the reflectance factor of glass is highly overestimated (approximately 20 % across all visible wavelengths). However, the

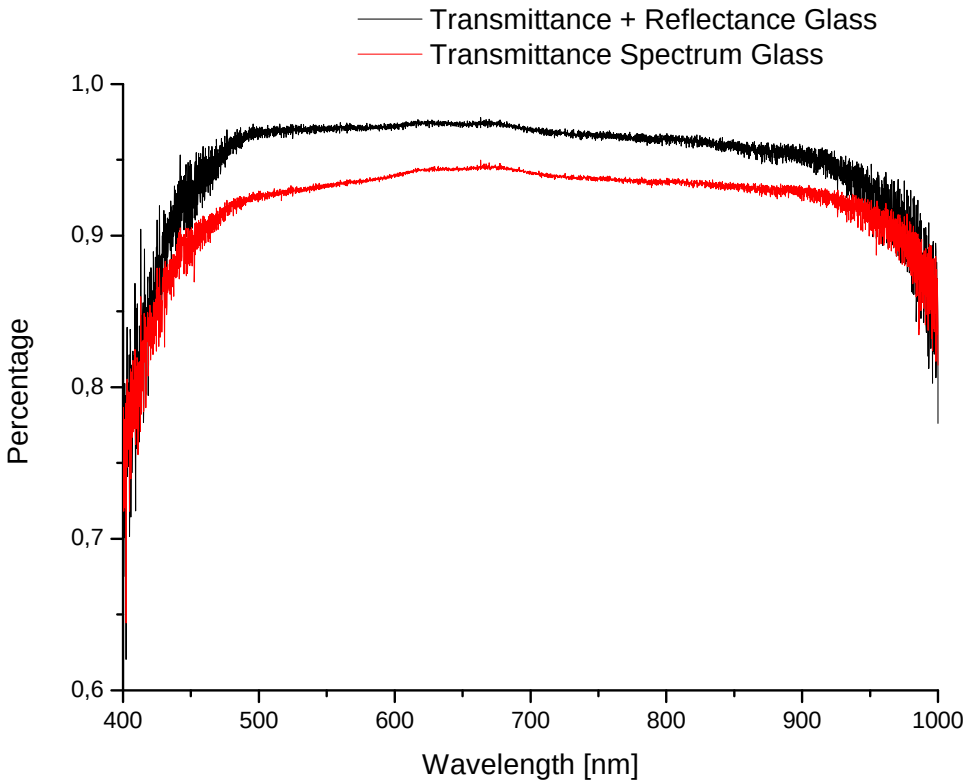

Figure A.2: Transmittance Spectrum of the glass substrate as well as the sum of the reflectance and the transmittance of the glass. The tails of the spectra are attributed to the limited performance of the ligth source.

reflectance of the light source is likely to be greater than the amount of light re-transmitted into the reflection sphere. Put in other words, an amount of the transmitted light will be reflected in the transmission sphere and not (re-)re-transmitted into the reflection sphere when the glass is at the sample port. This exchange of light between the spheres could in principle also be significant in the transmittance spectrum of sample, giving rise to an overestimate of the transmittance. The transmittance spectrum of glass in addition to the sum of the reflectance and transmittance is plotted in Fig A.2. As can be seen from the figure, the transmittance of glass iss 0.94 across the wavelength range, as it should be. It is important to note that the exhange of light between the sphere is not included in the post measurement processing of transmission data.

Bibliography

[1] T.F Stocker , Q. Dahe and G.K Plattner et al. (editors). Climate change 2013: The physical science basis. *Working Group I Contribution to the Fifth Assessment Report of the Intergovernmental Panel on Climate Change. Summary for Policymakers*.

[2] C. Braird and M. Cann. *Environmental chemistry, 5th edition*. W.H Freeman and Company, 2008.

[3] World energy outlook 2011. `http://www.iea.org/publications/freepublications/publication/WEO2001_WEB.pdf`. [Online; Accessed 05.04.2014].

[4] V. Fthenakis. Sustainability of photovoltaics: The case for thin-film solar cells. *Renewable and Sustainable Energy Reviews*, 13(9):2746–2750, 2009.

[5] A.E Becquerel. Memoire sur les effets electriques produits sous linfluence des rayons solaires. *Comptes Rendus*, 9:561 – 567, 1838.

[6] M.A Green. Photovoltaic principles. *Physica E: Low-dimensional Systems and Nanostructures*, 14(1):11–17, 2002.

[7] C. Kittell. *Introduction to solid state physics, Seventh edition*. Wiley New York, 1996.

[8] T.M Razykov, C.S Ferekides, D. Morel, E. Stefanakos, H.S Ullal and H.M Upadhyaya. Solar photovoltaic electricity: current status and future prospects. *Solar Energy*, 85(8): 1580–1608, 2011.

[9] T.O Håvardstun. Optical properties of metal nanoparticle arrays created using electron beam lithography. Master's thesis, Universiity of Bergen, 2013.

[10] D.A Kleinman. Considerations on the solar cell. *Bell System Technical Journal*, 40(1): 85–115, 1961.

[11] T. Dzhafarov. Silicon solar cells with nanoporous silicon layer. *Solar Cells-Research and Application Perspectives, edited by Professor A. Morales-Acevedo*, page 42, 2013.

[12] A. Goetzberger and C. Hebling. Photovoltaic materials, past, present, future. *Solar energy materials and solar cells*, 62(1):1–19, 2000.

[13] W. Shockley and H.J Queisser. Detailed balance limit of efficiency of p-n junction solar cells. *Journal of applied physics*, 32(3):510–519, 2004.

[14] M. A Green. Third generation photovoltaics: solar cells for 2020 and beyond. *Physica E: Low-dimensional Systems and Nanostructures*, 14(1):65–70, 2002.

[15] G.L Pearson , D.M Chapin and C.S Fuller. A new silicon p-n junction photocell for converting solar radiation into electrical power. *Journal of Applied Physics*, 25(5):676–677, 1954.

[16] A. Goetzberger , J. Luther , Joachim and G. Willeke. Solar cells: past, present, future. *Solar Energy Materials and Solar Cells*, 74(1):1–11, 2002.

[17] A. Morales-Acevedo and G. Casados-Cruz. Forecasting the development of different solar cell technologies. *International Journal of Photoenergy*, 2013:1–5, 2013.

[18] R.W Miles, H.M Hynes and I Forbes. Photovoltaic solar cells: An overview of state-of-the-art cell development and environmental issues. *Progress in Crystal Growth and Characterization of Materials*, 51(1):1–42, 2005.

[19] H.A Atwater and A. Polman. Plasmonics for improved photovoltaic devices. *Nature materials*, 9(3):205–213, 2010.

[20] P. Denby. Wipo patent application wo/2010/117280, 2010.

[21] M. M. Greve. *Nanostructures for the manipulation of electromagnetic waves*. PhD thesis, University of Bergen, 2013.

[22] A.W Murray and W.L Barnes. Plasmonic materials. *Advanced Materials*, 19(22):3771–3782, 2007.

[23] E. Hutter and J.H Fendler. Exploitation of localized surface plasmon resonance. *Advanced Materials*, 16(19):1685–1706, 2004.

[24] M.W Knight, H. Sobhani, P. Nordlander and N.J Halas. Photodetection with active optical antennas. *Science*, 332(6030):702–704, 2011.

[25] W. Rechberger, A. Hohenau, A. Leitner, J.R Krenn, B. Lamprecht and F.R Aussenegg. Optical properties of two interacting gold nanoparticles. *Optics Communications*, 220 (1):137–141, 2003.

[26] P.G Kik and Mark M.L Brongersma. *Surface plasmon nanophotonics*. Springer, 2007.

[27] A. Moores and F. Goettmann. The plasmon band in noble metal nanoparticles: an introduction to theory and applications. *New Journal of Chemistry*, 30(8):1121–1132, 2006.

[28] S.A Maier. *Plasmonics: fundamentals and applications*. Springer, 2007.

[29] D.K Gramotnev and S.I Bozhevolnyi. Plasmonics beyond the diffraction limit. *Nature Photonics*, 4(2):83–91, 2010.

[30] M.C. Garnett. Colors in metal glasses and in metallic films. *Philosophical Transactions of the Royal Society of London*, 203:385–420, 1904.

[31] G. Mie. Optics of turbid media. *Annalen der Physik*, 25:377–445, 1908.

[32] D. Pines. Collective energy losses in solids. *Reviews of modern physics*, 28(3):184–198, 1956.

[33] R.H Ritchie. Plasma losses by fast electrons in thin films. *Physical Reviews*, 106(5): 874–881, 1957.

[34] U. Kreibig and P. Zacharias. Surface plasma resonances in small spherical silver and gold particles. *Zeitschrift für Physik*, 231(2):128–143, 1970.

[35] D.J Griffiths. *Introduction to Electrodynamics 3. edition*. Prentice Hall Upper Saddle River, New Jercey, 1999.

[36] M. Pelton and B.W Garnett. *Introduction to Metal-Nanoparticle Plasmonics*. John Wiley & Sons, 2013.

[37] P. Hofmann. *Solid state physics: An introduction*. John Wiley & Sons, 2011.

[38] C.F Bohren and D.R Huffman. *Absorption and scattering of light by small particles*. Wiley-VCH, 1998.

[39] L. Novotny and B. Hecht. *Principles of Nano-optics*. 2012.

[40] P. Stoller, V. Jacobsen and V. Sandoghdar. Measurement of the complex dielectric constant of a single gold nanoparticle. *Optics letters*, 31(16):2474–2476, 2006.

[41] L.K Kelly, E. Coronado, L.L Zhao and G.C Schatz. The optical properties of metal nanoparticles: the influence of size, shape, and dielectric environment. *The Journal of Physical Chemistry B*, 107(3):668–677, 2003.

[42] P. Mulvaney, L.M Liz-Marzán V. Myroshnychenko, J. Rodríguez-Fernández, I. Pastoriza-Santos, A.M Funston, C. Novo and F.J.G de Abajo. Modelling the optical response of gold nanoparticles. *Chemical Society Reviews*, 37(9):1792–1805, 2008.

[43] R. Lazzari, I. Simonsen, D. Bedeaux and J. Jupille. Polarizability of truncated spheroidal particles supported by a substrate: model and applications. *The European Physical Journal B - Condensed Matter and Complex Systems*, 24(2):267–284, 2001.

[44] C.R. Kumar, editor. *Uv-vis and photoluminescence spectroscopy for nanomaterials characterization*. Springer, 2013.

[45] V. Amendola, O.M Bakr and F. Stellacci. A study of the surface plasmon resonance of silver nanoparticles by the discrete dipole approximation method: effect of shape, size, structure, and assembly. *Plasmonics*, 5(1):85–97, 2010.

[46] R. Lazzari and I. Simonsen. Granfilm: a software for calculating thin-layer dielectric properties and fresnel coefficients. *Thin Solid Films*, 419(1):124–136, 2002.

[47] D. Bedeaux and J. Vlieger. *Optical properties of surfaces*. Imperial College Press, 2004.

[48] C. Langhammer, M. Schwind, B. Kasemo and I. Zoric. Localized surface plasmon resonances in aluminum nanodisks. *Nano letters*, 8(5):1461–1471, 2008.

[49] V. Juve, M.F. Cardinal, A. Lombardi, A. Crut, P. Maioli, J. Perez-Juste, L.M Liz-Marzan and N. Del Fatti. Size-dependent surface plasmon resonance broadening in nonspherical nanoparticles: single gold nanorods. *Nano letters*, 13(5):2234–2240, 2013.

[50] C. Noguez. Surface plasmons on metal nanoparticles: the influence of shape and physical environment. *The Journal of Physical Chemistry C*, 111(10):3806–3819, 2007.

[51] T.L Temple and D.M Bagnall. Optical properties of gold and aluminium nanoparticles for silicon solar cell applications. *Journal of Applied Physics*, 109(8):084343–084343, 2011.

[52] C. Langhammer, B. Kasemo and I. Zorić. Absorption and scattering of light by pt, pd, ag, and au nanodisks: absolute cross sections and branching ratios. *The Journal of chemical physics*, 126(19):194702–194702, 2007.

[53] Lab Sphere. Reflectance and transmittance measurement integrating spheres. `http://woodall.ece.ucdavis.edu/pdf/labsphere_reflectance_manual.pdf/`. [Online; Accessed 05.05.2014].

[54] I. Simonsen , R. Lazzari, J. Jupille and S. Roux. Numerical modeling of the optical response of supported metallic particles. *Physical Review B*, 61(11):7722–7733, 2000.

[55] S.V Stavseng. Numerical modelling of the optical properties of truncated and coated prolate spheroidal nanoparticles. Master's thesis, Norwegian University of Science and Technology (NTNU), 2013.

[56] E. Aursand. Optical properties of truncated and coated spheroidal nanoparticles on a substrate. Master's thesis, Norwegian Univeristy of Science and Technology (NTNU), 2012.

[57] K. Rottmann. *Matematisk Formelsamling*. Spektrum Forlag, 2003.

[58] Ø. Storesund Hetland. Granfilmgui - a graphical user interface for simplified use of the simulation software granfilm. Master's thesis, Norwegian Univeristy of Science and Technology (NTNU), 2011.

[59] J. Jupille I. Simonsen, R.Lazzari and S. Roux. Numerical modeling of the optical response of supported metallic particles. *Physical Review B*, 61(11):7722–7732, 2000.

[60] I. Simonsen. `http://web.phys.ntnu.no/~ingves/Software/GranFilm/Current/`. [Online; Accessed 12.12.2013].

[61] Sopra Database. Sopra n.k database. `http://www.ioffe.ru/SVA/NSM/nk/`. [Online; Accessed 05.05.2014].

[62] International Organization for Standardization. 14644-1: Cleanrooms and associated controlled environments–part 1: Classification of air cleanliness. 1999.

[63] M.G Stepanova and S. Dew. *Nanofabrication*. Springer, 2012.

[64] A.A Tseng, K. Chen, C.D Chen and K.J Ma. Electron beam lithography in nanoscale fabrication: recent development. *IEEE Transactions on Electronics Packaging Manufacturing*, 26(2):141–149, 2003.

[65] M.M Greve and B. Holst. Optimization of electron beam lithography intsrument for fast, large area writing at 10 kv acceleration voltage. *Journal of Vacuum Science and Technology B*, 26(2):141–149, 2013.

[66] C-.H Seo and K-.Y. Suh. Reduction of proximity effect in electron beam lithography by deposition of a thin film of silicon dioxide. *Korean Journal of Chemical Engineering*, 25 (2):373–376, 2008.

[67] M.A McCord and M.J Rook. *Handbook of microlithography, micromachining, and microfabrication: microlithography*. Bellingham WA: SPIE Optical Engineering, 1997.

[68] A. Misaka, K. Harafuji and N. Nomura. Determination of proximity effect parameters in electron-beam lithography. *Journal of applied physics*, 68(12):6472–6479, 1990.

[69] MicroChem NANOTM PMMA. Pmma/copolymer datasheet.

[70] R. Abargues, U. Nickel and P.J Rodríguez-Cantó. Charge dissipation in e-beam lithography with novolak-based conducting polymer films. *Nanotechnology*, 19(12):125302 (6pp), 2008.

[71] J.W Pickering, C.J.M Moes, H.J.C.M Sterenborg, S.A Prahl and M.J.C Van Gemert. Two integrating spheres with an intervening scattering sample. *Optical Society of American Journal A*, 9(4):621–631, 1992.

[72] K.F Carr. A guide to integrating sphere radiometry. *Labsphere Technical Guide, Labsphere Inc*, 1997.

[73] M.M Greve, T. Håvardstun and B. Holst. Measuring the localized surface plasmon resonance effect on large arrays (5 mm$\times$ 5 mm) of gold and aluminum nanoparticles on borosilicate glass substrates, fabricated by electron beam lithography. *Journal of Vacuum Science & Technology B*, 31(6):06F410, 2013.

[74] X. Wang, P. Gogol, E. Cambril and B. Palpant. Near-and far-field effects on the plasmon coupling in gold nanoparticle arrays. *The Journal of Physical Chemistry C*, 116(46): 24741–24747, 2012.

[75] G. Owen and P. Rissman. Proximity effect correction for electron beam lithography by equalization of background dose. *Journal of Applied Physics*, 54(6):3573–3581, 1983.

[76] Thermo Scientific. Thermo scientific microscope coverslip product information. `http://www.labochema.ee/documents/tarvikud/menzel/Menzel_CoverSlips_UK.pdf/`, 2008. [Online; Accessed 07.05.2014].

[77] U. Guler and R. Turan. Effect of particle properties and light polarization on the plasmonic resonances in metallic nanoparticles. *Optics express*, 18(16):17322–17338, 2010.

[78] T.R Jensen, M.D Malinsky, C.L Haynes and R.P Van Duyne. Nanosphere lithography: tunable localized surface plasmon resonance spectra of silver nanoparticles. *The Journal of Physical Chemistry B*, 104(45):10549–10556, 2000.

[79] K.E Herold and A. Rasooly. *Biosensors and Molecular Technologies for Cancer Diagnostics*. CRC Press, 2012.

[80] T. Klar, M. Perner, S. Grosse, G. Von Plessen, W. Spirkl and J. Feldmann. Surface-plasmon resonances in single metallic nanoparticles. *Physical Review Letters*, 80(19): 4249–4252, 1998.

[81] S.H Ghosh, and P. Tarasankar. Interparticle coupling effect on the plasmon resonance of gold nanoparticles: from theory to applications. *Chemical Reviews*, 107(11):4797–4862, 2007.

[82] A. Pinchuk, G. von Plessen and U. Kreibig. Influence of interband electronic transitions on the optical absorption in metallic nanoparticles. *Journal of Physics D: Applied Physics*, 37(22):3133, 2004.

[83] P. Albella, Z. Pirzadeh, P. Alonso-Gonzalez, F. Huth, S. Bonetti, V. Bonanni, J. Åkerman et al. J. Chen. Plasmonic nickel nanoantennas. *Small: nano micro*, 7(16):2341–2347, 2011.

[84] Z. Pirzadeh, T. Pakizeh, V. Miljkovic, C. Langhammer, Christoph and A. Dmitriev. Plasmon–interband coupling in nickel nanoantennas. *ACS Photonics*, 1(3):158–162, 2014.

[85] G.A and H.G Craighead. Optical response and fabrication of regular arrays of ultrasmall gold particles. *Thin Solid Films*, 125(1):165–170, 1985.